High Throughput 3-D Tissue Cytometry

by

Hyuk Sang Kwon

Submitted to the Department of Mechanical Engineering

in partial fulfillment of the requirements for the degree of Doctor of Philosophy in Mechanical Engineering

at the

MASSACHUSETTS INSTITUTE OF TECHNOLOGY

June 2007

Author .....
Hyuk-Sang Kwon
Department of Mechanical Engineering

Certified by .....
Bevin P. Engelward
Professor of Biological Engineering

Certified by .....
Matthew J. Lang
Professor of Mechanical Engineering

Certified by .....
Dr. Richard Gilbert
Mechanical Engineering

Certified by .....
Peter T. C. So
Professor of Mechanical Engineering and Biological Engineering
Thesis Committee Chairman, Thesis Supervisor

Accepted by .....
Lallit Anand
Chairman, Department Committee on Graduate Student

High Throughput 3-D Tissue Cytometry

by

Hyuk Sang Kwon

Submitted to the Department of Mechanical Engineering

on May 15, 2007 in partial fulfillment of the requirements for the degree of

Doctor of Philosophy in Mechanical Engineering

Abstract

This thesis presents the ongoing technological development of high throughput 3-D tissue cytometry.and its applications in biomedicine. 3-D tissue cytometry has been developed in our laboratory based on two-photon microscopy (TPM) that is capable of *in situ* 3-D imaging of tissue up to a volume of several mm^3 with subcellular resolution. This high throughput tissue cytometry achieves an imaging rate of 2 mm^3/hour. I optimize the performance of this instrument by developing two new techniques. First, the image signal-to-noise-ratio and the microscope penetration depth can be improved by reducing tissue scattering. Optical clearing agents can significantly lower tissue scattering by index matching of different tissue constituents. While the application of tissue clearing agent has been extensively studied in fresh tissues, its application has not been extensively studied in paraffin fixed and frozen tissues. Frozen tissues are particularly important as tissue sections can be retained for biochemical and genetic analysis after fluorescence imaging. We investigate the effects of optical clearing agents in sub-zero temperature in terms of TPM image contrast and penetration depth. Second, tissue cytometry are often used in the detection of rare cells. In this case, if the region containing these rare cells can be identified by low magnification imaging first, there is no need to image the whole tissue specimen. I modified the two-photon tissue cytometer to incorporate a low magnification, wide field, one-photon imaging subsystem. Wide field surface imaging allows us to locate regions of interest and to perform high resolution 3-D imaging only at these locations using a micron precision x-y specimen positioner. 3-D tissue cytometry is applied in two biomedical applications. In the first project, in collaboration with Prof. Bevin Engelward, we study the frequency, the distribution and the clonal expansion rate of cells that undergo recombination during cell division using genetically engineered mice. The Fluorescent Yellow Direct Repeat (FYDR) mice developed by the Engelward group have cells that express yellow

fluorescent proteins if recombination occurs during cell division. In the second project, in collaboration with Dr. Richard Gilbert, we investigate the muscle architecture of whole mouse tongues. Dr. Gilbert's group has shown that force generation and deformation of the tongue can be characterized by "fiber tracks" observed in tongues using high field MRI. However, the morphological origin of these tracks has not been fully qualified on the cellular level and we seek to correlate these tracks with structures observed using 3-D tissue cytometry.

Thesis Supervisor: Peter T.C. So
Title: Professor of Mechanical Engineering and Biological Engineering

Acknowledgements

I thought that I would write many pages of acknowledgement. The truth is that I cannot even start writing because I cannot finish. There are too many people that I thank for.

I thank God, Hye-Sue Chong, Peter, Bevin, Matt, and Richard for their help for finishing my Ph. D. work at MIT. Hye-Sue always asked me to do the things that I am happy about. She wanted me to be a happy person. Peter has many skills that I would like to have, especially his approach of solving problems. He knows many things, but more over he never quits. He knows how to get things done and he does it. He put lots of efforts and helped, guided, and took care of me when I was having trouble solving problems. I thank him for his helps and considerations in both academic and private life of mine. Thank you, Peter! I hope some day I can help him in some way if he needs me. My school days were very lengthy one. There are many things that I should have, could have, or would have done differently. However, I have met many friends and I am very happy for that. I learned many lessons from friends, teachers and people in MIT. I appreciate that. I am sure that I will remember these lessons. Thank you for your sometimes cheerful, sometimes hard-to swallow, but always truthful remarks!

I would like to thank people in So lab (current and past members), KGSA members, collaborators, 500 technology square family, Leslie Ragan, Olga Parkin, and Tom Quinn. I would like to thank Hayden Huang, Yoonsung Nam, Terry Gaige, and Wei Chung for mouse tissue specimen preparation. I would like to pray for the many mice that were sacrificed for my work. I wish that you would find eternal peace in heaven.

I thank my parents, brother, Mihwa Lee, and relatives. They were always willing to help me in every possible way. Perhaps, I took it for granted. Now I realize that. Thank you!

There are many people that I do not mention here specifically, but I do remember in my daily life. I thank you guys! I received so many things from you, but I did not give you guys much. I would like to give you something nice in return.
I hope that I would make a person who can do something for the people in need. Hopefully, in the near future.....

Table of Contents

List of figures

List of Table

List of abbreviation

TPM	Two-photon excitation microscopy
FYDR	Fluorescent yellow direct repeat
CFM	Confocal fluorescence microscopy
SNR	Signal to noise ratio
FC	Flow cytometry
ECM	Extracellular matrix
PMT	Photomultiplier tube
MMM	Multifocal multiphoton microscopy
CCD	Charge-coupled device
CT	Computed tomography
PET	Positron emission tomography
MRI	Magnetic resonance imaging
OCT	Optical coherence tomography
OPT	Optical projection tomography
SIM	Surface imaging microscopy
SEM	Scanning electron microscopy
NA	Numerical aperture
FOV	Field of view
RPM	Revolution per minute
FFT	Fast fourier transform
FWHM	Full-width-at-half-maximum
FITC	Fluorescein isothiocyanate
RMS	Root mean square
WFM	Wide-field fluorescence microscopy
NIR	Near infrared
DMSO	Dimethyl sulfoxide
PBS	Phosphate buffer solution
DNA	Deoxyribonucleic acid
DSBs	Double strand breaks
HR	Homologous recombination
EYFP	Enhanced yellow fluorescent protein
WD	Working distance
NMR	Nuclear magnetic resonance

DTI	Diffusion tensor imaging
DSI	Diffusion spectrum imaging
PDF	Probability distribution function
ODF	Orientational distribution function
DW-MRI	Diffusion weighted magnetic resonance imaging

Chapter 1

Introduction

1.1. Major advantages of TPM for biomedical imaging

Goeppert-Mayer theoretically predicted two-photon excitation process in 1930s and Denk, Webb and co-workers introduced two-photon excitation microscopy (TPM) for biomedical imaging in 1990s [A1, A2]. TPM is a three dimensional incoherent imaging technique based on the nonlinear excitation of fluorophores. Two-photon excitation occurs only at focal point by the simultaneous absorption of two photons each having half of the energy needed for the excitation transition in typical fluorescence microscopy. The two-photon excitation probability is significantly less than the case of one-photon excitation. It only occurs at the regions of both high temporal and spatial photon concentration. First, the high temporal concentration of photons is realized by the use of high-peak power pulsed mode-locked femto-second laser. Second, the high spatial concentration of photons is realized by focusing the laser beam with a high numerical aperture objective to a diffraction-limited spot.

TPM is a high resolution fluorescence microscopy technique that provides 3-D images of cells and tissues. TPM allows 3-D biological specimen to be imaged with resolution comparable to that of confocal fluorescence microscopy (CFM) that has found many biological applications [A3-A7]. For some applications, TPM is rapidly gaining acceptance [A8, A9]. TPM has three distinctive advantages over other imaging modalities [A10, A11]. First, TPM achieves 3-D images with micron resolution to a depth of a few hundred microns for some of the biological specimens. Depth discrimination is the most important feature of TPM. This depth discrimination effect of the two-photon excitation arises from the quadratic dependence of two-photon fluorescence intensity upon the excitation photon flux, which decreases rapidly away from the focal plane. In TPM, over 80% of the total fluorescence intensity comes from a 1 μm thick region around the focal volume for objectives with numerical aperture of 1.25. Conventional CFM obtains 3-D resolution by using a detection pinhole to block out-of-focal plane fluorescence. For this reason, CFM loses a significant fraction of the emission light and it is not an efficient imaging tool especially in cases of highly scattering specimens. For imaging in highly scattering biological specimen such as turbid tissue, this capability of limiting the region of excitation instead of the region of detection is critical. Second, the longer wavelengths employed in TPM have significantly lower scattering and absorption in the specimen which helps ensure deeper tissue penetration. Third, TPM uses mostly near infrared light for excitation which is well spectrally separated from visible fluorescence emission. It allows for high-sensitivity imaging by eliminating the contamination of the fluorescence signal by the

excitation light. The separation between the excitation and emission spectra ensures that the excitation light and the scattering induced effect such as Raman Scattering can be rejected easily without filtering out any of the fluorescence photons resulting in a higher signal-to-noise-ratio (SNR). Fourth, TPM causes minimal photo-damage to biological specimens; thus it is compatible with *in vivo* imaging. TPM can initiate photochemical reaction inside cells and tissues causing potential photo-damage. However, since out-of-plane chromophores are not excited in TPM, photobleaching and photo-damage of biological specimens is restricted to the sub-femtoliter focal volume.

1.2 Two types of cytometry

Cytometry is defined as the quantification of the physical and biochemical features of cells. The characteristics of cells that are most commonly measured are optical characteristics such as fluorescent and scattering properties that can be related to the morphological, biochemical and gene expression states of the cells using appropriate fluorescent probes. There are cytometry techniques which are capable of examining large populations of cells in order to generate quantitative statistics of the population.

1.2.1. Flow Cytometry

One of the earliest cytometry techniques that enabled researchers to quantitatively and statistically assay large populations of cells was flow cytometry (FC) [A12-16]. As a quantitative analysis method applicable to individual cells or cell organelles, FC has become a very popular tool in biological and clinical study. FC provides high throughput cellular measurement where cells are carried along by a fluid stream one by one across a sensing point. At the sensing point, the biological states of these cells are assayed by optical spectroscopy. FC has found applications in a broad range of biomedical and biotechnological applications when populational analysis of cellular state is required or when rare cells must be detected from a large background population. The high throughput, specificity, and cell sorting capabilities have made FC a valuable cytometry technique in both the clinical and research settings.

In FC, cells are prepared in a suspension and this suspension is flowed through the sensing region where individual cells sequentially pass through in a fine stream. Scattering, absorption or fluorescence signals are collected from the interaction of the cell with the excitation light in the sensing region [A17]. FC is particularly important when population analysis of cellular state is required or when rare cells must be detected

from a large background population [A18]. However, there are two disadvantages in using FC. FC has limitations including a lack of spatial resolution and requires artifact-prone and laborious specimen preparation procedures. There are, in general, cell-cell, cell-tissue, and cell to extracellular matrix (ECM) interactions in tissues. In the absence of cell-tissue interactions, potential changes in cellular physiological states may occur. It is well known that the biochemical, mechanical, and intracellular inputs present in a tissue can all dramatically affect the behavior of a cell. Once the cell is removed from this tissue environment, these inputs are lost along with much of the native cell morphology and any meta-information about its place in the 3-D architecture of the tissue. The differences in the cellular behavior in their native tissue setting and in artificial environment are relevant in the interpretation of clinical and basic research results. In pharmaceutical development, these differences are also partially responsible for the high failure rate of drug candidates in tests at the tissue level inside actual organisms. Further, FC can only provide spectroscopic signature while morphological and structural information of cells cannot be studied due to instrument limitations. Finally, cells can only be studied by FC at a specific time point, temporal evolution of cellular states cannot be studied. For these reasons, there is a need for the development of cytometric tools that can effectively characterize cells in their native tissue state, can characterize both their structural and biochemical states, and can have ability of studying their evolution in time.

1.2.2. Image cytometry

Motivated by some of the limitations inherent in FC, image cytometry was developed [A18-A21] It shares some important characteristics with FC, like the ability to investigate large cell populations as well as acquire multi-parameter data on individual cells such as (1) cell morphology, (2) spatial localizations and orientation, (3) distribution of chromophores within cell, and (4) temporal evolution. In image cytometry, a population of cells is imaged on a microscope coverslip or other types of solid support rather than analyzed in suspension [A22]. Image cytometry offers several advantages over FC. First, since it is an imaging technique, it acquires morphological information of the cells in the population. This provides valuable information about the biological state of the cell, and it also provides spatial information of cellular compartments such as the nucleus or the cytoplasm. It is also possible to relocate cells of interest to study their temporal evolution. An additional advantage of image cytometry is the capability to study cells in intact tissues [A23,A24]. Image

cytometry can be used in research or some clinical setting as an important quantitative aid to standard histopathology [A25,A26]. A disadvantage of image cytometry is that it is generally slower than FC. For example, typical imaging speed for TPM is about a frame per second. However, the performance of imaging cytometry is increasing and the gap in processing speed between image cytometry and FC is decreasing.

1.3 Importance of *in situ* tissue imaging

The differences in the cellular behavior in their native tissue setting and in artificial environment are relevant in the interpretation of clinical and basic research results. There is a pressing need for the development of new cytometric tools that can effectively characterize cells in their native tissue state. Investigating the behavior of cells in intact tissues offers several advantages. First, since it isn't necessary to extract the cells from the tissue by mechanical or enzymatic means, there is much less opportunity to introduce artifacts into the analysis. Second, cellular morphology is drastically different between cells inside native tissues and the same cells grown on 2-D tissue culture. Third, the removal of cells from a tissue also necessarily eliminating many of the mechanical and biochemical signal inputs that are known to dramatically affect cell behavior and gene expression profile. Fourth, cell-cell interactions inside of an intact tissue can also be an important factor in cell function that is impossible to study once the cells have been removed from the tissue. Finally, imaging intact tissues preserves the 3-D architecture of the tissue specimen and provides a great deal of spatial and contextual information that is otherwise lost. All of these factors will affect the behavior and state of the cell and, depending on the question being asked, could easily have important biological or clinical ramifications. In many cases, the gene expression profile of the cell will change from its native state in the tissue. Many cell-based studies may thus be potentially predicated on a fundamentally faulty data set. As an example of the importance of studying intact tissues, is in the field of liver research where researchers have been unable to construct a liver model based on hepatocytes grown in 2-D culture. In order to approximate the expected behavior of hepatocytes researchers have had to engineer 3-D liver cell constructs [A27]. Another important area where the *in situ* tissue properties of cells are of critical importance is in the field of cancer research. Cancer is a disease which has a very strong spatial component to its etiology [A28]. Cancer cells can invade the stroma of the surrounding tissue and recruit non-malignant cells to differentiate and support the growing tumor. The arrangement of normal tissue boundaries becomes pathogenic as the expression profiles

of the surrounding cells are altered by cell signaling from the malignant cells [A29, A30]. The realization of the importance of the *in situ* properties of cancer, both in terms of the expression profiles of the individual cells and their spatial arrangement with respect to one another has led to the development of techniques such as laser capture microdissection [A31,A32].

1.4. Image cytometry based on TPM

Despite the obvious advantages of studying the native states of cells within the 3-D environment of their host tissue, standard preparation for both flow and image cytometry studies have been limited to cells in suspension or in 2-D culture. This is mainly due to technical limitations in the traditional instrumentation that cannot easily characterize large populations of cells within the 3-D environment of macroscopic thick tissues.

Most high-resolution imaging techniques are not well suited for deep tissue imaging due to absorption and scattering from interaction between tissue constituents and excitation light. Standard wide field microscopy suffers from very poor resolution and contrast when attempting to image more than several microns from the surface of the tissue. Confocal scanning microscopy is a technique that has shown some success in imaging intact tissue. However in practice, the axial imaging depth is less than 40 microns for many tissue types. Moreover, it has high phototoxicity and photobleaching in of-out-of-focus planes which further limits its usefulness. A more recent imaging technique that has proven far more suitable for studying tissues is TPM.

There are inherent advantages of two-photon microscopy that lends itself to be used in developing 3-D image cytometry. TPM has strengths such as its inherent 3-D sectioning, low background, high penetration depth, and low phototoxicity. For these reasons, it is particularly well suited for imaging biological specimen such tissues [B1-B20]. TPM can study tissue structures with subcellular resolution, and reduction of specimen photo-bleaching and photo-damage. Depending on the biological specimen, it can image into thick tissue specimens up to a few hundred microns. 3-D image cytometry using TPM has the ability to characterize multiple cell layers in specimens; in contrast, 2-D image cytometry can monitor only a single cell layer. However, 3-D image cytometry requires high speed two-photon imaging. With the high throughput rate and the deep tissue imaging capability, 3-D image cytometry based on TPM has the potential for the detection of rare cellular events in intact tissues. Conventional TPM systems have image acquisition rates on the order of a few seconds which is far too

slow for imaging macroscopic specimens. The incorporation of high speed imaging capacity is critical for imaging large areas in a reasonable amount of time. The basic challenge in the engineering of these type of systems is to achieve high speed imaging (around 10-30 Hz frame rate) while maintaining sufficient detection sensitivity to visualize weakly autofluorescent tissue structures. A number of approaches have been adopted to achieve video rate scanning. [H21 – H24]. I will describe the two common approaches: single point scanning with a polygonal scanner and multi-foci scanning.

1.4.1. TPM and high speed imaging

The typical frame rate of TPM is in the order of seconds. This frame rate increases especially in low light situations, such as in deep tissue imaging. There are two way to improve TPM imaging speed for high throughput cytometry applications [A34-37]. One way to achieve high speed two-photon imaging is the use high speed scanners. Our lab designed and implemented a video rate two-photon system based on the raster scanning of a single diffraction limited focal spot using a high-speed polygonal mirror (figure1.1) [A35]. In this system, the laser beam is rapidly raster scanned across a specimen plane by means of two different scanners: a fast rotating polygonal mirror provides high speed line scanning along one direction (x-axis), with about 3 kHz line rate. A slower galvanometer-driven scanner with a 500 Hz bandwidth moves the line along the orthogonal direction (y-axis) to cover the image plane. An eyepiece lens and tube lens expands the excitation light to fill the back aperture of the objective providing diffraction limited imaging. The emission light from the imaging volume is collected by the same objective and is detected by a photomultiplier tube (PMT) detector. More in depth discussion of this technology is presented in Chapter 2.

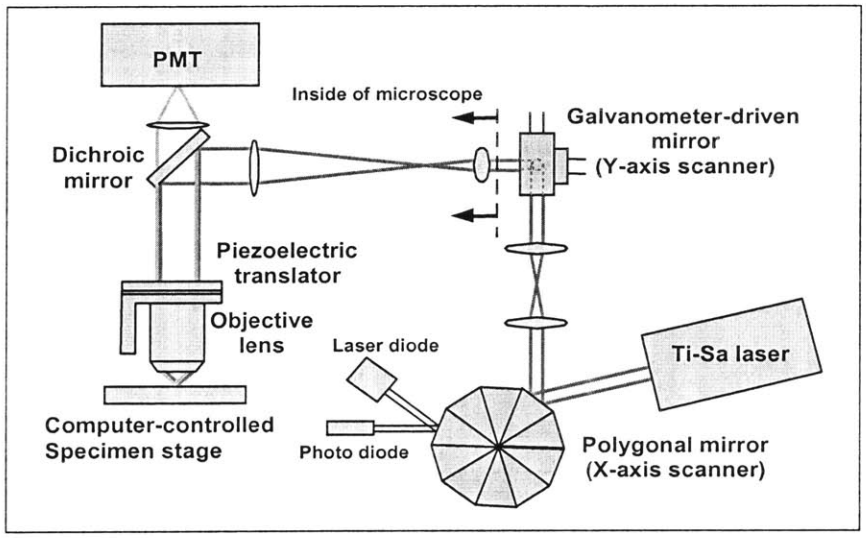

Figure 1.1: Fast Scan microscopy developed by Kihean Kim [A35]

Another promising way to increase the speed of TPM is to scan multiple foci across the specimen although we did not use this approach the current thesis research [A36,A37]. In this multifocal multiphoton microscopy (MMM) configuration, an array of foci is generated at the field aperture plane. The emission from each focal point is again collimated by the excitation tube lens and is directed to the objective through a dichroic mirror. The collimated rays are designed to overlap at the back aperture of the objective and to overfill it. The objective projects the individual focal points into the specimen. The scanning of the foci can be achieved by either rotating or translating a lenslet array, or by using galvanometric scanners in the light path. The emission light is collected by the objective in epi-illumination mode, deflected by the dichroic mirror, and focused by the emission tube lens. A charge-coupled device (CCD) camera or PMT array can be placed at the image plane to record the image.

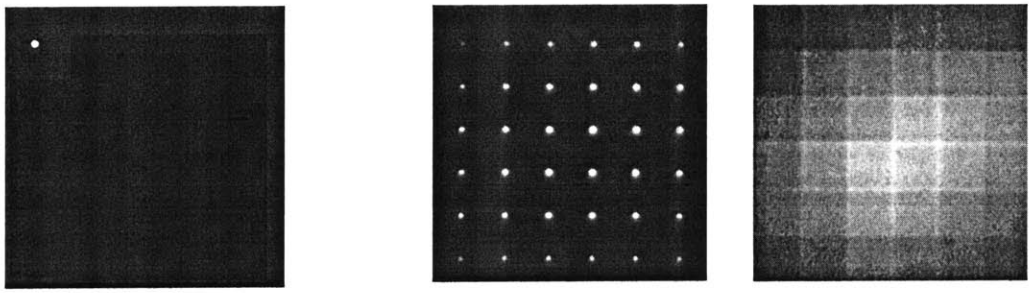

Figure 1.2. Two high speed scanning methods: Fast Scan (A) has a one focus scan fast utilizing polygonal mirror and MMM (B) has multiple foci scan corresponding smaller area. (C) MMM image of fluorescein solution.

1.4.2 3-D tissue cytometry

The construction a novel high-speed 3-D tissue cytometry based on TPM was accomplished in our lab. By incorporating high speed image capabilities with automated cutting mechanism, it becomes possible to image large populations of cells within their native tissue environment using TPM and extend standard 2-D image cytometry into 3-D image cytometry. We have termed this technique two-photon 3-D tissue cytometry.

1.5. Statement of work

Although imaging of large tissue of small animal organ using 3-D cytometry has been successfully demonstrated by our group, significant engineering challenges remain. The goal of this thesis is to continue the development of existing high speed two-photon based 3-D tissue cytometry, and further optimize the system for increase acquisition speed and image quality. Two approaches will be taken: (1) Combine low magnification wide field imaging and automated specimen positioning for rare cell detection in the two-photon tissue cytometry. Many cytometry applications require the detailed study of rare cells or cell clusters. In this case, there is little need of imaging the whole tissue specimen if the locations of these cells or cell clusters can be identified by low magnification, wide field imaging and if automated specimen positioning has sufficient accuracy to relocate these regions of interest during high magnification imaging. (2) The penetration depth of TPM on turbid tissue is limited. This poor penetration depth can be improved by optical treatment of specimen, which decreases the data acquisition time. We propose to develop a technique for optical clearing of fresh, fixed, and frozen tissue specimen. We further apply this 3-D tissue cytometry in two studies. The first study aims to quantify recombination events in tissues with implications in carcinogenesis. The second study seeks to correlate lingual structures observed using magnetic resonance imaging with cellular level structures observed using high resolution optical microscopy. Understanding tissue structures over multiple length scales allows tissue mechanics to be understood on the basis of cellular morphology and biochemistry.

Chapter 2

Instrumentation and methodology development

2.1 Three dimensional tissue cytometry based on fast scan microscopy

2.1.1. Introduction: deep tissue imaging techniques

There are many 3-D biomedical imaging modalities on the organ level, such as computed tomography (CT), positron emission tomography (PET), and magnetic resonance imaging (MRI). While these techniques all have unique strengths, it is common among them that they do not have resolution for subcellular structures. For example, while high resolution MRI is capable of imaging whole animals, its resolution is limited to about hundreds of microns [B1]. There are a number of high resolution optical imaging methods such as optical coherence tomography (OCT) [B2], optical projection tomography (OPT) [B3], CFM, and TPM. OCT can achieve a few mm in imaging depth and depends on temporal coherence for axial resolution. Typical resolution of OCT in the radial direction is on the order of micron, and axial direction is on the orders of tens of micron but micron level resolution has been achieved in rare cases. OPT is a new technique and has been successful for imaging millimeters thick translucent specimen, such as embryos. However its performance in highly turbid specimen has not been well demonstrated. CFM and TPM are 3-D imaging techniques that have subcellular resolution. CFM is the most established method for 3-D biomedical imaging but its imaging depth is often limited to within about 50 micron into a tissue sample. Moreover, due to its excitation wavelength is in the UV and blue spectral ranges, significant photodamage and photobleaching can occur on the focal plane as well as out-of-focus regions. TPM is a particularly promising tool among 3-D tissue optical imaging techniques, mainly because of its high resolution, and reduced photodamage as described in the Introduction section. For even higher resolution imaging, there is surface imaging microscopy (SIM) [B4]. SIM is a block face technique. In one implementation, this method incorporates scanning electron microscopy (SEM) imaging and microtome sectioning to construct 3-D images with voxel sizes on the order of 10 by 10 by 50 nm. However, this system is not a practical tool for imaging a large volume mainly because its voxel resident time is on the order of tens of microseconds ensuring lengthy data acquisition for larger specimens.

While TPM has a penetration depth of several hundred microns, superior to other high-resolution optical microscopy techniques, it is still insufficient to image the full thickness of whole organs of small animals. For example, tumor metastasis has

been studied in animal models and been shown to occur over great distances [B5]. There is a growing interest in understanding how the information contained in the genome is deployed throughout the three dimensional environment of an actual organism [B6]. To effectively understand how the gene expression affects tissue physiology and pathology, an imaging technique is required to map the entire organ and relate the morphological information to the underlying expression profile. We partly overcame this limitation of TPM by incorporating an automated microtome into a high throughput multiphoton microscope. By imaging serial sections tens to hundreds of microns into a fixed tissue block, and then sectioning off the top layer and imaging the newly exposed section, it is possible to image through an entire ex vivo specimen, and obtain 3-D images of macroscopic volume with microscopic resolution. The primary objective of my thesis work is to develop and optimize 3-D tissue cytometry which is based on two-photon excitation technology and can image whole small animal organs such liver, heart and tongue ex vivo.

2.1.2 Constructing a 3-D tissue cytometer based on a fast scan microscope.

The 3-D image cytometer is design to image tissues with volumes on the order of cubic millimeters to cubic centimeters. In the Applications section, the capability of this instrument is demonstrated in the imaging of a 3 mm × 3 mm × 3 mm mouse tongue based on autofluorescent and second harmonic generation from the specimen.

The construction of a novel high-speed 3-D tissue cytometry is based on TPM with improving data acquisition speed, and the adaptation of automated tissue sectioning mechanism [B7]. The proposed system is composed of three key elements: a high speed TPM using a polygonal scanning mirror achieving a speed approximately 40 times faster than convention TPM, an automated x-y specimen stage, and an automated tissue sectioning mechanism.

The instrument is built with a Zeiss microscope (Axioscope, Zeiss Thornwood, NY). A femtosecond Ti:Sapphire laser, powered by a continuous wave Nd:YLF diode pump laser, (Mira 900, Coherent, Palo Alto, CA) is used to induce two-photon fluorescence providing high power mode-locked pulses for non-linear two photon excitation. The microscope system is optimized for the excitation wavelength in the range between 700 and 900 nm. Both the polarization and the power of excitation light at the specimen are controlled by a half wave plate (CVI Laser Inc., Putnam,

Connecticut) and a Glan-Thomson polarizer. Typically, to avoid excitation saturation of chromophores, the average laser power incident upon the specimen must be less than about 25 mW. The laser beam is rapidly raster scanned across a sample plane by means of two different scanners. A fast rotating polygonal mirror (Lincoln Laser, Phoenix, AZ) accomplishes high-speed line scanning along x-axis and a slower galvanometer-driven scanner with 500 Hz bandwidth (Cambridge Technology, Cambridge, MA) correspondingly deflects the line-scanning beam along the sample's y-axis. The spinning disc of the polygonal mirror is composed of 50 aluminum-coated facets arranged contiguously around the perimeter of the disc. The facets repetitively deflect the laser beam over a specific angular range and correspondingly scan a line 50 times per revolution. To acquire imaging speed of 10 frames per second, rotation speed of 3750 rpm was selected and this corresponds to the line scan speed of 320μs/line. The pixel residence time was approximately 0.7 μs. An independent laser diode (1mW at 632 nm, Thorlabs, Newton, NJ) along with a photodiode detector (Thorlabs) is used to encode the polygonal mirror position and to generate a reference signal. This signal is used by a high-speed data acquisition circuit (see the data acquisition part below) to synchronize the x-y scanners, the objective translator, and PMT detection circuitry. The laser beam is coupled into an upright microscope (Axioscope, Zeiss, Thornwood, NY) by means of a modified epiluminescence light path. The beam is reflected by the dichroic mirror toward the objective and is focused on the specimen. We often use a Zeiss 40× Fluar 1.3 numerical aperture (NA) objective to focus the laser light onto the sample and directed the fluorescent signal to the emission path of the microscope. The specimen is raster scanned with a single excitation focus and photons are collected using non-spatially resolved detectors, such as a PMT running in the analog mode (R3896, Hamamatsu, Bridgewater, NJ). To perform 3-D volume scans, the objective is mounted on a computer-controlled piezoelectric objective translator (P-722.00, Physik Instrumente, Waldbronn, Germany). The maximum z-axis travel range is 100μm. Axial translation of the objective yields a z-stack of image planes. The induced fluorescence signal is collected by the same objective and passes through the dichroic mirror. Residual scattered light is removed by an additional barrier filter (SP700, Chroma Technology, Brattleboro, VT). The fluorescence is recorded by a high-sensitivity PMT (R3896, Hamamatsu, Bridgewater, NJ). Currently, a two-color detection scheme is available by separating the two color signals via a dichroic mirror. The two color channels have matching band-pass filters and the signals are detected by two PMTs. The current signals from the PMTs are converted to a voltage signal using a transimpedience circuitry and a 16-bit A/D converter (NI 6251,

National Instruments Corp., Austin, TX) which can operate up to 1.25 million samples per second. The signal is transferred to the computer memory through the PCI bus. Images are generated by integrating signal synchronized with the raster-scanning pattern of the scanners. The imaging speed is 10 frames per second for 300 by 400 pixels using one color channel. With the Zeiss 40X Fluar 1.3NA objective, the field of view (FOV) is approximately 200 μm by 150 μm.

To image areas larger than the field of view of the objective, a robotic stage (H101, Prior Scientific, Rockland MA) was used. Overlaps between the images stacks at adjacent stage locations were maintained to facilitate montaging of these image stacks. The amount of overlap in 2-D was set to about 30%, but it may be decreased with advances in registration technique (under development). This robotic stage also translates the sample for mechanical sectioning. Since the maximum imaging depth of TPM is a few hundred microns for acceptable SNR in most tissues, we image the whole animal organ by removing and discarding the tissue layer that has been imaged. The robotic stage was used to translate the sample from the objective to a home-built milling machine that had been integrated into the microscope system. The milling machine consisted of a 1" milling bit driven by a DC motor rotating at 300 revolutions per minute (RPM). In addition to the milling stage, we further incorporated a pressurized air blower to remove chips generated from the milling process and a syringe dispenser to replace the immersion oil on the sample after cutting. The milling machine, the air blower, and the syringe oil dispenser are all automated and are coordinated by the data acquisition software written in LabView (National Instruments Corporation, Austin).

It is important that the throughput of this 3-D cytometry is high so that large tissue volume and a large cell population can be imaged within a reasonable time period. The throughput rate is determined by the size of the field of view in the microscope system and the imaging speed. Larger tissue area can be sampled with a bigger FOV without slower specimen translation. The objective of lower magnifications is preferred for this reason, but it is also critical to use the objective of a high NA to achieve micron scale resolution and to maximize the collection of emission signal.

2.1.3 Calibration procedures for the 3-D tissue cytometry

The resolution of the two-photon microscope is verified and calibrated by imaging specimens that consist of immobilized sub-diffraction limited fluorescent latex spheres. Under the current system design with a 40X Zeiss Fluar, 1.3 NA, objective, the z-resolution of the current system is about 2 microns and the lateral resolution is on

the order of 0.7 micron. Therefore, TPM image was sampled at 2.0 μm in the axial direction.

In addition to verify the optical resolution of the system, it is also important to calibrate the various mechanical translators used in the 3-D tissue cytometer. We measured the image pixel size, the step size of the pizeo-objective translator, and the x, y, z step sizes of the robotic specimen stage. To determine the pixel size of a 2-D image, it is necessary to measure the size of its FOV. The FOV was determined by imaging a ronchi ruling (a grating with 5000 lines per inch). There are two ways to determine the pixel size from a ronchi ruling image. The first method is simply counting the number of grating period in the ronchi ruling. The second way is to find spatial frequency of ronchi ruling using fast Fourier transform (FFT). Results from both methods agree that the FOV was approximately 200 micron by 150 micron in x and y directions, respectively, for the 40X objective. Since our images are 400 by 300 pixels in the x and y directions, the pixel sizes are 0.5 micron.

The step size of the piezo-objective translator was calibrated by imaging large fluorescent beads along the axial direction (e.g. invitrogen F8844). The cross-sections of the bead were imaged at successive depths. The size of the bead was estimated by summing of the photon counts from central pixels of the bead around its centroid. When the laser focuses above and below the bead, the intensity is close to zero. On the other hand, when the laser focuses inside the bead, the intensity is high. By measuring the distance between the rising edge and falling edge of the intensity profile of the bead along the axial direction, a full-width-at-half-maximum (FWHM) of the bead can be determined in terms of piezo-positioner step size. Since the diameter of the bead is known a priori, one can calibrate the size of the piezo-positioner step. A convolution step has been taken to correct for the finite axial PSF of the system. We measured that 8 volt input to piezo-positioner along z direction is sufficient to cover the entire 15.5 μm diameter fluorescent bead (F8844). Therefore, each z-step input (in volt) to piezo-positioner corresponds to about 2 μm movement in z axis.

The lateral motion of the robotic specimen stage is calibrated using a similar procedure. A field of 10 micron beads was imaged by laser scanning. Afterwards, the specimen stage is translated by a known number of steps and a second image was taken. By cross-correlating the two images before and after the step, the size of the step can be determined using the known bead size as a reference. The axial motion of the robotic specimen stage is calibrated using the fine focus drive of the Zeiss microscope which has a scale of 2 micron per step. Fluorescent beads are imaged at one plane where they are in focus and then imaged at a different plane after translating

the objective using the fine focus drive. The needed axial displacement for the robotic stage to put the specimen back in focus allows us to calibrate the axial step size of the robotic stage which is measured to be about 0.3 micron per one axial step; 200 axial steps corresponds to 60 micron movement in z axis.

2.1.4. Imaging procedure using the 3-D tissue cytometer

The protocol for the use of the 3-D cytometer is detailed as follows. The first task is laser alignment and the alignment of optics in the excitation path. We further ensure that the specimen stage and detectors were well covered to block out all the stray light from the room. After the alignment process, the flatness of the FOV was accessed by imaging a fluorescein isothiocyanate (FITC) solution. Intensity non-uniformity is mostly due to a slight distance misalignments of the polygonal scanner and the galvanometric scanning mirror from the conjugated common eye-point. Slight non-uniformity in the field is unimportant and can be corrected by normalizing subsequent images using a correction file generated from an uniform fluorescein solution image. After alignment, the proper functioning of tissue sectioning components (the mill, the oil dispenser, and the air pump) were checked and confirmed.

The specimen was typically embedded in paraffin. The specimen was next placed on the stage and properly oriented. The specimen was mounted on a specimen holder with the use of double sided tape and epoxy glue. The specimen holder was then bolted to the robotic x-y stage. Initial cutting of the sample removes a thin 30 micron layer from the top surface of the specimen to ensure flatness of the surface. Flatness of the sample is critical to minimize artifacts during imaging. Flatness of the sample surface ensures subsequent cuts are smoother and exert less force on the specimen and the stage. Minimizing force results in reducing positioning error of the specimen before and after the cutting. Visual and tactile inspection was sufficient to ensure sufficient flatness. If there were any excessive variations in surface height of the specimen, additional cuts will be taken until flatness is achieved. A critical parameter of the milling system is the rotational speed that should be adjusted to optimizing the cutting of paraffin or other embedding medium. The initial cutting step is also very important to check the alignment of cutting mechanism to ensure that the cut surface of the specimen surface is parallel and coincident with the imaging plane of the objective. Since objective was fixed to microscope body and could not be adjusted, the position of milling bit height was adjusted via a micrometer driven stage translator with 1 micron resolution. Additional positioning control allows the orientation of the

cutting mechanisms to be adjusted until parallelism is achieved. After initial cutting of the specimen, the size of the sample for imaging was approximated. The imaging region was set by the smallest but sufficient rectangle to cover the whole paraffin block. The four x-y coordinates of the imaging region were determined and used to program the robotic stage. After these parameters are optimized, this design gives a cutting reproducibility of a less than a micron in height and works well for the 3-D tissue cytometry.

The imaging conditions should be optimized for different specimen. The goal was to find the combinations of imaging parameters that resulted in greatest imaging depth with acceptable SNR. Depending on the specimen, various combinations of objective lens type, excitation wavelength, and excitation power were tried and evaluated in terms of those two goals specified. Since in TPM all power improvements result in quadratic signal enhancement, even small improvements in excitation throughput can lead to appreciable signal enhancements of the overall system. In general, choosing the appropriate power level for two-photon imaging is constrained by two basic boundary conditions: The minimum accepted SNR determines the minimum power that can be used whereas the damage threshold of the specimen determines the maximum power. Further, the use of power significantly higher than the fluorophore excitation saturation threshold will cause resolution degradation. It is also important to minimize possible artifacts such as specimen thermal damage under excess power.

The acquisition of image data is divided in three basic steps which are explained in figure 2.1. The first step was imaging. For opaque specimens such as mouse tongue tissue, a 120 by 120 by 80 micron volume can be raster scanned by the galvanometric scanners laterally and by the piezoelectric objective positioner axially. The typical axial imaging depth ranged from tens to hundreds of microns, depending on the tissue opacity and objective working distance of the objective. For the imaging of a larger lateral area, the next step was to raster scan the specimen with respect to the objective using the robotic x-y stage. A macroscopic volumetric image can be montaged from a series of smaller image stacks as discussed earlier. Once this process was completed, the third step was to remove the tissue layers that have already been image. This was accomplished by translating the entire specimen axially a predetermined distance and then moving the specimen toward the milling machine where the uppermost portion is mechanically sectioned. The translation speed was approximately a millimeter per second for paraffin samples that was empirically determined at to produce smooth (< 5 μm in root mean square (RMS)) cuts at the

surface of the sample for TPM imaging. For an imaging depth of 80 μm, the sectioning depth was 60 μm allowing a 20 μm axial registration overlap. For more transparent specimens, greater imaging depth can be achieved while keeping the same 20 μm overlap for registration. Clearly, more efficient imaging can be done in more transparent specimens. After cutting, the chips and debris were removed with the air blower and fresh immersion oil was dispensed. The same three steps were repeated until the entire specimen was imaged. We note that this entire process is automated and requires no interaction from the user other than mounting the specimen and inputting the imaging and sectioning parameters.

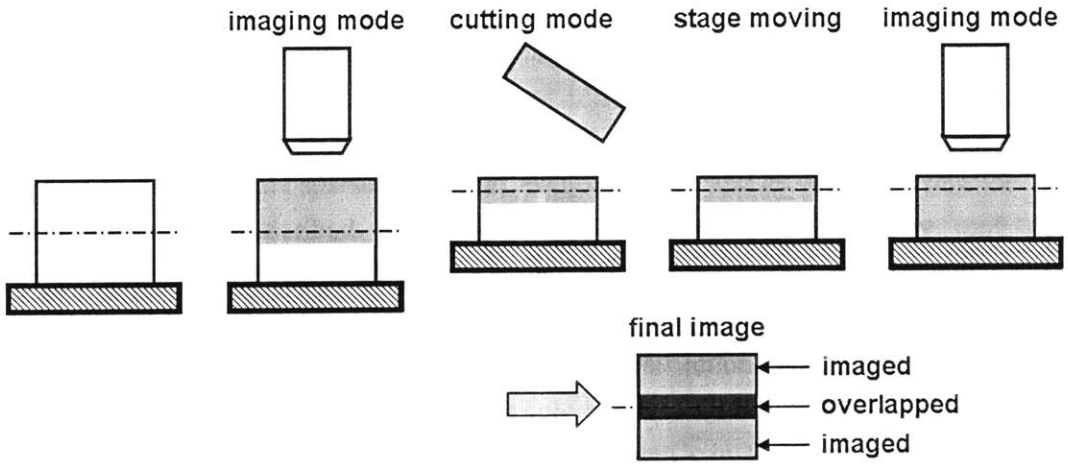

Figure 2.1: 3-D tissue cytometry imaging procedure. Imaging mode is composed of successive small volume imaging of sample for entire surface with objective and piezo. It would take about 4 seconds to image small volume of about 200 by 150 by 80 micron in size with 2 micron incremental step in z. It would take a second to position the sample to image adjacent small volume. Cutting mode is composed of translating the sample to the cutter and removing the debris, supplying immersion oil. It takes about 80 seconds for cutting process.

2.1.5. Conclusion

We have developed a fast, automated 3-D image cytometer with subcellular resolution that is capable of imaging ex vivo tissue specimen up to a cubic centimeter in size. It can be used for imaging macroscopic tissue volumes or whole small animal organs. It can identify unique rare cells in larger populations as well as can reveal information about the biochemical state of the organ. There is a wide range of biomedical studies that are feasible using this 3-D tissue cytometery in fields such as neurobiology, cardiology, cancer biology and muscular disorder.

2.2. Development of high throughput site-selective 3-D tissue cytometer

Many cytometry applications require the detailed study of spatially sparse biological event by detecting rare cells or cell clusters. In this case, there is little need of imaging the whole tissue specimen if the locations of these cells or cell clusters can be identified by low magnification, wide field imaging and if automated specimen positioning has sufficient accuracy to relocate these regions of interest during high magnification imaging.

2.2.1. Introduction

In the study of sparse biological events in large tissue volume, using the 3-D tissue cytometry described in Section 2.1 would require unnecessary long data acquisition time and would produce unnecessarily large dataset. Furthermore, wide-field, low magnification imaging also provides a useful record of the global tissue histological state as a background for the high resolution two-photon 3-D images. This site selective system is realized with conventional TPM with the addition of wide-field fluorescence microscopy (WFM). A specimen can be readily imaged at high resolution using two-photon fluorescence microscopy and at low resolution using wide-field fluorescence imaging. Regions of interests can be identified by wide field image and they can be subsequently interrogated at high resolution using 3-D resolved two-photon imaging.

A. Problems associated with 3-D tissue cytometry data acquisition time

One application of the site selective 3-D image cytometer is in the study of carcinogenesis due to mutation events. FYDR mouse developed in the Engelward laboratory is a genetically engineered mouse where cells express yellow fluorescent protein after undergoing homologous recombination at an integrated transgene. This allows the identification of genetically different but phenotypically normal cells. In collaboration with Engelward laboratory, this site-selective high throughput 3-D Image cytometry was used to study spatially sparse biology events, where we studied the frequency, the distribution and the clonal expansion rate of pancreatic cells that undergo recombination during cell division using genetically engineered mice. It was done by

carefully imaging foci in 3-D so that we can learn how many cells are in each focus and potentially the types of cells in the focus. Since homologous recombination at specific locus is a rare event, the frequency of recombinant cells in the pancreas is ~5 per million. The pancreas of mouse contains approximately 10^7 cells and has a size of approximately 1.5 cm by 1 cm by 0.05 cm when it was placed on the slide glass. There are about 50 recombinant foci in the adult mouse pancreas. It would take about 50 hours for 3-D tissue cytometry to image an entire pancreas tissue organ and detect these foci containing recombinant cells with use of 20X objective with 50 micron imaging with 20 micron overlap. However, using 3-D site-selective tissue cytometry, the location of these cell clusters can be first recorded with WFM and then 3-D high resolution imaging of the cluster can be done with TPM. It takes 10 seconds to image a surface of 5 mm by 4 mm in WFM. This imaging platform can rapidly identify very rare fluorescent cell clusters within an entire mouse tissue (at the cm scale) and subsequently provides 3-D imaging of individual fluorescent cells in each cluster (at the micron scale). The estimated time for imaging all the foci is about 6 hours, almost an order of magnitude reduction in data acquisition time.

2.2.2 Development of site-selective 3-D tissue cytometry

This new development complements the existing 3-D tissue cytometry allowing high throughput analysis of tissue specimens with sparse regions of interest. We developed and implemented a technique that incorporates low magnification wide field imaging with TPM. The system is realized with conventional TPM with the addition of wide field fluorescence microscopy and an automated specimen positioning. For wide field imaging, we typically use low magnification, low numerical aperture objective with lower resolution but larger FOV such as 1.25X NA. For two-photon imaging, we typically use high numerical aperture oil-immersion objective with higher resolution, but smaller FOV such as 20X.

From the low magnification wide field image, the whole surface of the tissue specimen can be imaged and regions of interest can be recorded, identified and positioned reliably for further high resolution two-photon imaging using an automated x-y stage positioner.

A. Imaging methods

Both of the two-photon microscopy and wide field fluorescence microscopy are common techniques and both can be readily implemented. The optical schematic

describing both systems is shown in figure 2.2.

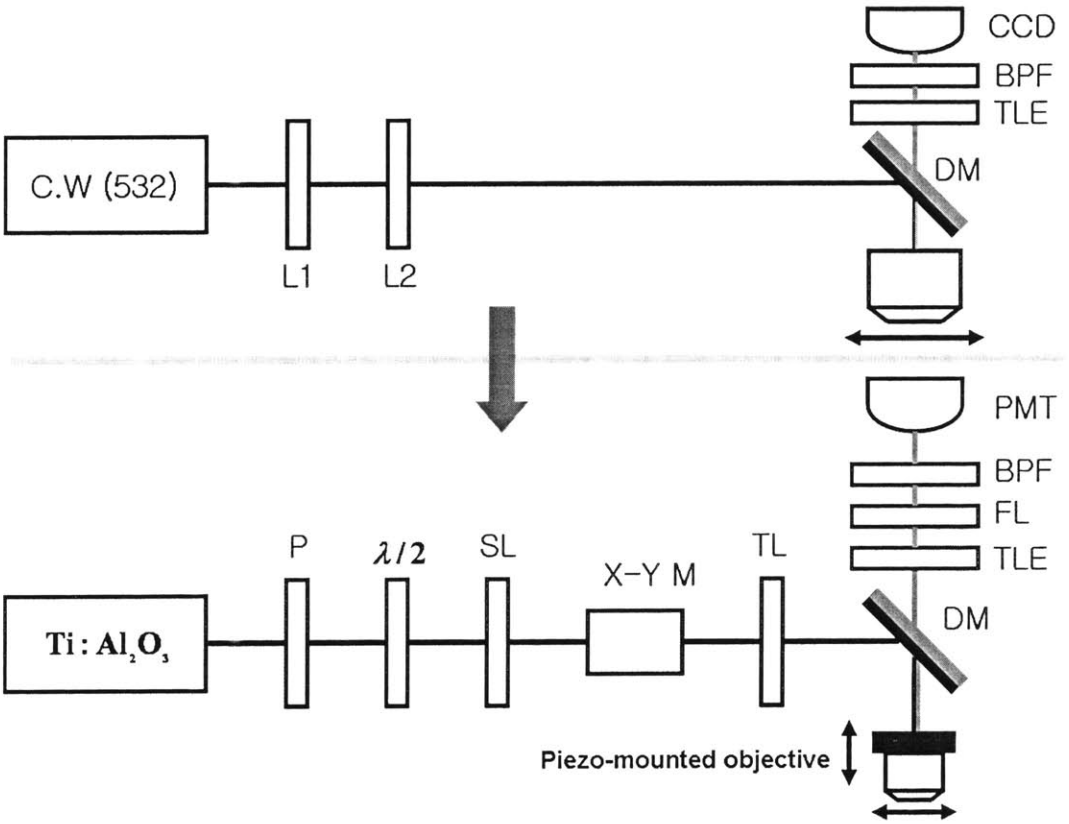

Figure 2.2: Optical layout for 3-D site-selective tissue cytometry. Black line connecting optical component indicates the excitation beam and Gray light indicates the emission beam. CW (532) denotes the excitation source for WFM; continuous wave diode laser with 532 nm wavelength. L1 and L2 are combination of lenses for magnifying and collimating excitation laser beam. DM denotes dichroic mirror. TLE denotes emission tube lens inside microscope body. BPF denotes band pass filter in emission path. CCD denotes for the charge-coupled device. It provides spatial information as well as the intensity information. Ti:Al_2O_3 denotes the excitation source for TPM; Ti-saph laser with tuning capability. P denotes the polarizer. λ/2 denotes half wave plate. With these polarization and power level can be adjusted. SL denotes scan lens. X-Y M denotes x-y mirror scanner. TL denotes tube lens for excitation path. FL denotes de-scanning lens. Horizontal arrow indicates the motion of the x-y specimen stage.

A1. Two-photon microscopy

The design of the two photon microscopy is described in the INTRODUCTION

A2. Widefield fluorescence microscopy

In a conventional WFM, the entire FOV of the specimen is illuminated with light from an excitation source, and the image can be viewed directly by eye or projected onto an image capture device. Typical wide field image is a mixture of a sharp, focused image of the emitted light from in-focus plane and a blurred image of the emitted light from out-of-focus planes. It is for this reason that the primary application of a WFM is in the imaging of thin specimens up to several microns. For thicker specimen, fluorescence signal may still be detected but the fluorescent object can no longer be sharply imaged. The source of excitation light can be a mercury lamp, or a laser in the typical one-photon exctiation wavelength range. In general, it is possible to use multiple excitation sources to selectively excite a number of fluorophores in the specimen. Wide field imaging is an inherently high throughput method since both the illumination and detection of light throughout the FOV are achieved almost simultaneously.

B. Common equipments for both imaging modalities

There are many common elements for both imaging modalities. Both imaging modalities share a Zeiss Axiovert 110 microscope (Zeiss Inc., Thornwood, NY). An automated x-y stage was used to translate the specimen under the objective. A computer with home-built data acquisition card and home-built data acquisition software was used for TPM as well as running Viewfinder software (Pixera Corporation, San Jose, CA) for WFM.

C. Excitation source

For WFM, the light source unit is composed of a green diode laser (BTG - 2S, Beam of Light Technologies, Clackamas, Oregon) and a beam expander. Excitation beam is magnified by the beam expander and is focused at the back focal plane of the low magnification, low NA, objective resulting in a collimated beam on the specimen. The beam expansion unit controls the size of FOV. In the case that the specimen contains fluorophores with different excitation spectra, multiple excitation sources can be implemented to meet this need. For TPM, a 75MHz, 100GHz pulsed mode-lock Ti-Sapphire laser (Tsunami, Spectra Physics, Palo Alto, CA) was used as described previously. A lens pair consists of an eyepiece lens and a tube lens expands the excitation light to fill the back aperture of an objective lens providing diffraction limited imaging. In this system, the laser beam is raster scanned across a 2-D specimen filed of view by means of x-y scanner. 3-D structure of the specimen is generated by

stacking 2-D images spaced by accurate incremental movement of the piezo actuator attached to the objective. The selection between WFM and TPM modes requires an exchange objectives as well as manually direct excitation light through different optical paths via several switchable mirrors.

D. Detection

For wide field imaging, the Pixera Pro150ESM systems features a monochrome CCD sensor with 1.5M pixels, 62-dB signal-to-noise ratio, low dark noise and detection sensitivity of 0.01 lux. For two-photon imaging, the fluorescence detected at each point is measured by a high sensitivity photomultiplier tube (R7400P, Hamamatsu Corporation, Bridgewater, NJ). The excitation spot is raster scanned across the specimen allowing an image to build up mapping the distribution of the fluorophores. The emission light from the imaging volume is collected by the same objective and is detected by a CCD for WFM or a set of PMT detectors for TPM. Data acquisition time depends on the specimen size as well as the occurrence frequency of the spatially sparse rare events in the biological specimen.

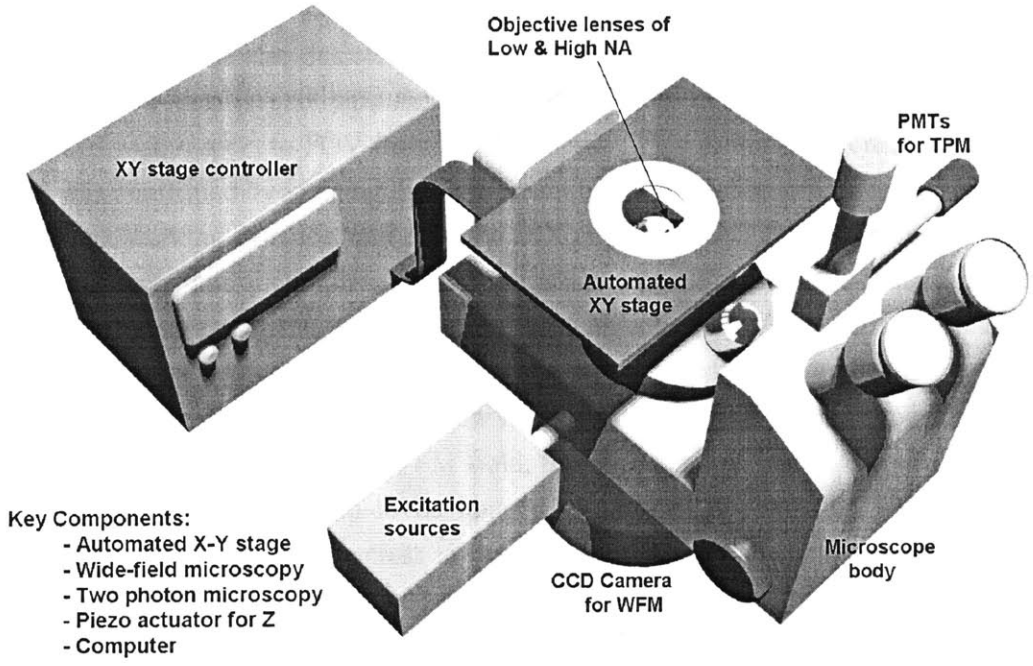

Figure 2.3: 3-D site-selective tissue cytometry equipment. For wide-field microscopy, continuous laser excitation, low NA objective, and CCD camera are used. For two-photon microscopy, high power pulsed mode-lock laser, high NA objective with piezo actuator, and high sensitive PMTs are used. Computer controlled x-y stage is used for both imaging modalities.

E. Imaging procedures

First, the imaging procedure starts with aligning the FOV for both imaging modalities (figure 2.4). Each objective has different FOV size and working distance. For each microscopy, the FOV is set by the combination of the objective and the detector. For WFM, the combination of the 1.25X, low NA objective and Pander CCD camera has a FOV of approximately 5 mm by 6 mm. The resolution for WFM is 8 μ m (corresponding to 0.61λ/NA) with 532 nm excitation wavelength, and 0.04 NA objective. For TPM, the use of 20X 0.7 NA objective gives a FOV of approximately 240 um by 240 um. The resolution for TPM is less than 1 μm. The resolution of the WFM is smaller than the FOV of TPM. The centers in the FOVs for both imaging modalities were identified by using a centering-aid glass slide. The centering-aid slide contains a 200 micron size spot marked by both fluorescent beads and a slightly fluorescent ball-pointed pen mark. It was placed on specimen holder which was mounted on the computer controlled x-y stage. The small ball-pointed pen mark on the centering-aid slide was first focused by visual inspection through the eyepieces of the microscope using the high NA objective illuminated by wide field fluorescence illumination. The approximate distribution of the fluorescent beads on this ball pointed pen mark is also detected. Then, a lower NA objective was used and focused on same fine details and thus the center coordinates of the high NA objective is identified with respect to FOV from CCD camera. This center position of FOV in the TPM was confirmed by imaging the fluorescent beads. Each microscope objective has a different working distance, and only the 20X objective for TPM was mounted on the piezo actuator, thus focus plane in the specimen was different. We restore parfocal condition by adjusting the height of the 1.25X objective by placing a shim below it. For imaging, the biological specimen was placed on a slide glass and a robotic stage. The specimen is focused first by the low magnification objective. For specimens that are bigger than the FOV of the WFM field, the robotic stage raster scan the specimen allowing the whole specimen to be imaged prior to high resolution imaging. The locations of the regions of interest in the specimen are recorded. Each image is then opened, stitched together, examined and used for locating these biologically rare event sites. All the possible candidate sites are identified and verified by human eye and recorded. Sites likely to contain regions of interest are then ready for two photon imaging.

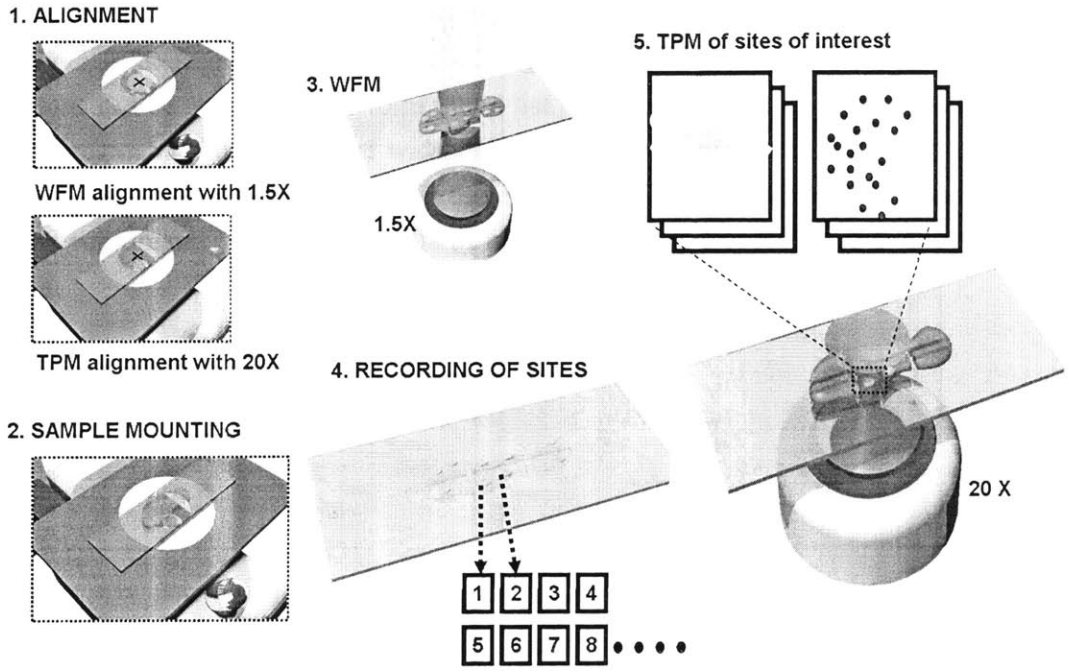

Figure 2.4: Image procedure for 3-D site selective tissue cytometry. The same point is identified and its position is recorded in both FOVs in alignment mode (1). Biological sample was mounted in slide glass (2). Series of WFM are done in order to identify rare events (3). Positions of the rare events sites are recorded (4). Series of TPMs are done on the rare sites one by one using automated x-y stage.

2.2.3 Discussions and Conclusions:

A. Advantages and disadvantages

In 3-D site selective tissue cytomtery, a large area is imaged rapidly with WFM, and specific regions of interest are imaged at high resolution with TPM. The current implementation of this site-selective tissue cytometry uses a slow speed TPM. While it is sufficient for many site selective studies, it is not suitable for whole organ imaging where higher raw speed is needed. Of course, similar site selective scheme can be implemented with the high speed 3-D tissue cytometer described in Section 2.1 providing even greater experimental flexibility. The maximum imaging depth is set by the minimum working distance of the objective used and the turbidity of the specimen.

B. Future plan: automation

It is possible to make the imaging process even more automated with a few simple changes. The results from WFM imaging can be more objectively and rapidly

interpreted in automated imaging processing. First, all the regions of interest in WFM image can be segmented and identified automatically. Second, the centroids of these regions can be computed and form into a list. Third, given this list of the positions of these regions of interest in the wide field image, the appropriate robotic x-y specimen stage coordinates corresponding to these positions can be calculated. Fourth, using these coordinates, high resolution TPM imaging can then be performed at these selected sites.

2.3 The effects of optical clearing in frozen tissue specimens

2.3.1 Introduction:

A. Light interaction with tissue

When light enters a tissue and interacts with its constituents, either absorption or scattering may occur. In the case of absorption, energy is either dissipated as heat or re-emitted as light in the case of fluorescence. A photon can be scattered by tissue constituents and changes its direction of travel with or without changing its energy. Photon scattering with tissue constituents occurs via both elastic Rayleigh and Mie scattering. The scattering of light occurs due to heterogeneity in optical refractive index. Rayleigh scattering describes the scattering process when the sizes of the scatterers are much smaller than the wavelength; Mie scattering describes processes where the scatterers are comparable in size to the excitation wavelength. The penetration depth of excitation light in the turbid biological specimen such as muscle tissues is limited by both the absorption and the scattering of light in general. Another complication arises in tissues or whole organs that have significant auto-fluorescence background resulting in poor SNR from regions of interest. Further SNR reduction may also occur due to optical aberration as light transverses through inhomogeneous tissues. It is known that absorption of light by tissue constituents is minimized in the near infrared (NIR) range of 700 ~ 1400 nm. For both Rayleigh and Mie scattering processes, the scattering effect has inverse power law dependence on wavelength. Therefore, scattering processes is minimized with increasing wavelength. Since the excitation light of TPM is in near-infrared wavelength, it provides better penetration into tissue specimen than other imaging modalities such as CFM that uses UV or blue/green excitation. CFM has a penetration depth less than 50 μm in typical tissue. Nonetheless, TPM imaging depth remains limited to less than one millimeter in typical tissue. A number of approaches have been proposed to circumvent this including using fluorescence lifetime imaging [C31] to better discriminate between target specimen fluorescence signal from autofluorescence background, using longer excitation wavelength in the 1.2-1.3 μm range to further minimize the effect of scattering and absorption [C32], and using adaptive optics to reduce optical aberration in the specimen [C33-C35]. A well demonstrated way to increasing the penetration depth of excitation light in the turbid biological specimen is to minimize the differences

in refractive index with use of optical clearing agent. The reflection of light at interface can be described by Fresnel equation, which basically describes the behavior of light when moving between media of differing refractive indices. In optics and fiber optics, index-matching materials are substances, usually a liquid, adhesive or gel, which have indexes of refraction that closely approximate that of optical elements or fibers. Index-matching materials are used to reduce Fresnel reflection at the surface of an optical element where typical transmission loss is about 5% per interface. With index matching, this loss can be made almost negligible.

B. The optical clearing effect

Optical clearing agents reduces scattering by matching refractive indexes of the constituents of a tissue specimen and have been shown to be effective in improving imaging depth in turbid biological tissues [C41]. Different types of optical clearing agents have different efficiencies in increasing the transparency of tissues [C42]. It has been found that the transparency of tissue is further related to the specific tissue type and the length of time that the tissue is treated with optical clearing agents [C41,C42]. There are researches into improving excitation light transport into deeply targeted areas of tissues to aid in diagnostic and therapeutic applications. Optical clearing agents, such as glycerol, dimethyl sulfoxide (DMSO), have been shown to reduce scattering in blood and tissue [C41]. From previous studies, two main theories have been suggested to explain the effects of hyperosmotic optical clearing agents. First, the index of refraction of the tissue constituents (such as collagen and cells) could be more closely matched by the agent than the interstitial or intercellular fluids. Second, dehydration of the cells due to the hyperosmotic optical clearing agent causes the tissue to become more densely packed. An increase in light penetration depth allows photons to reach deep lying target chromophores more effectively.

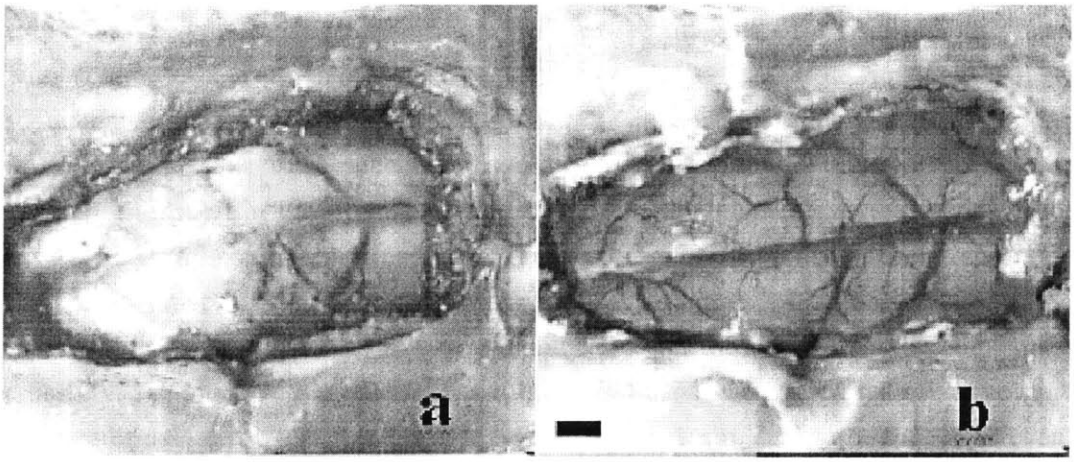

Figure 2.5: visual changes of image contrast of blood vessels for *in vivo* dura mater, *Tuchin, J.Phys. D: Appl. Phys. 38 (2005)*

C. Aims of this study

We investigated the effects of glycerol, an optical clearing agent, in enhancing the image contrast and penetration depth in TPM. There were four tissue specimens used in this study. The first and second biological specimens chosen for this study were ex vivo mouse heart, and liver for their opacity. The third one was mouse brain and it was chosen for its minimal opacity. The fourth one was mouse pancreas for determining the volume change before and after optical clearing application. Three states of the specimen were studied with or without application of optical clearing agent: fresh, fixed, and frozen. Fresh tissue specimens are excised and are imaged with minimal perturbation except refrigeration. Fixed tissue specimens are excised and subsequently fixed using standard paraformaldehyde procedure. Previously, some optical clearing experiments with fresh and fixed specimens at room temperature have been performed by other groups. Optical clearing study using TPM has been done to enhance the penetration depth utilizing optical clearing agent. However, optical clearing effect on frozen biological specimens with TPM imaging has not been explored. In this study, we aim to investigate the optical clearing effect on tissue specimen at temperature below freezing as well as at room temperature. There are a number of situations where biomedical imaging is performed at low temperature such as in laser treatment of port wine stains and some photodynamic therapy procedures. However, our primary interest is to identify an alternative sample preparation procedure for the tissue in whole organ imaging without fixation followed by paraffin embedding in 3-D tissue cytometry.

Tissue preservation is an important factor for 3-D tissue cytometry. For

example, the typical image acquisition time for the imaging of a whole mouse heart with volume of 1 cubic centimeter is several days [B7]. Therefore, imaging of fresh specimen is not feasible without fixation due to the specimen degradation with long imaging time. In usual specimen preparation for 3-D tissue cytometry involves fixation and paraffin embedding of the tissue in order to preserve the structure for several days of continuous imaging. There are many methods of tissue specimen fixation in order to keep accurate preservation of structure. It is desirable to use a crosslinking reagent that is of low cytotoxicity and can form stable and biocompatible crosslinked products. For example, the tissue first has to be treated with fixative such as paraformaldehyde or formalin, to cross link protein structure and to prevent decomposition. The specimen is subsequently embedded in paraffin to provide sufficient mechanical rigidity to allow accurate tissue sectioning needed for imaging beyond a few hundred microns by the 3-D tissue cytometry. While a chemically fixed organ has been successfully imaged (see Chapter 3), the fixation process will alter the biochemical environment in tissues hindering a number of genetic and protein assays. For example, results from a controlled study showed that there was a high frequency of non-reproducible sequence alterations detected with the use of formalin-fixed tissues [C36]. Further, in the case of paraffin embedding of the fixed tissue, there is often undesired increase in autofluorescence from paraffin interfering with signals during data acquisition. In contrast, frozen specimens have two main advantages for 3-D tissue cytometry. First, frozen specimen preparation is particularly important as it is an accepted tissue preservation approach where genetic and biochemical information are best preserved and can be assayed later. Second, we could avoid highly autofluorescent paraffin embedding that currently is needed to provide the necessary sample rigidity for mechanical sectioning. We are, therefore, interested in both fixed and frozen tissue specimens and whether they can be effectively optically cleared for 3-D cytometry study.

We will investigate the effect of optical clearing on fluorescence signal degradation in a fluorescence microscope as a function of depth. Further, while the effect of optical clearing on changing the tissue structure has been postulated, it has not been substantiated or quantified. We therefore seek to measure these structural changes experimentally so that microscopic images of optically cleared tissues can be better interpreted.

D. Lessons from cryoperservation

While optical clearing in a frozen specimen has not been previously studied, the experimental treatment of the tissue is quite similar to that used in cryoperservation, a very well studied field [C43]. Low temperature has significant effects on living tissues. Tissue is subject to degradation if there is no blood circulation unless the temperature is very low. Freezing-damage to cells is due to the formation of ice-crystals from water at low temperature. Moreover, organs can be damaged by small amounts of ice formation due to the critical cell-to-cell relationships which must be maintained for proper function. Although most living organisms are composed of large amounts of water, it is possible to avoid ice formation in many organisms from freezing. A cryoprotectant can make water harden into an amorphous glassy state with free of crystal formation, called the vitrification process [C44]. The addition of glycerol or other cryoprotectant not only lowers the freezing point, but it also changes the character of the ice, crystals will be much smaller and less damaging. Introduction of glycerol as a cryoprotectant was to protect bull sperm against freezing injury [C45]. Since then, glycerol as a cryoprotectant has long been used in vitrifying human blood & sperm, and for many years was used to reduce freezing in human cryonics patients. There are many types of cryoprotectants besides glycerol. For example, human embryos have been cryopreserved with not only glycerol, but with DMSO and propylene glycol these days. Cryoprotectants have been used to preserve bone marrow, fetal hearts, intestines, parathyroid glands, skin, spleens, thymus glands, etc. However, all cryoprotectant agents are toxic, some more than others. Cryoprotectant toxicity can potentially affect any organelle or macromolecule with proteins being the most vulnerable. The major cryoprotectants can be listed with respect to toxicity for most mammalian tissues. In the order of decreasing vitrifying strength and toxicity, major cryoprotectants were listed: Propylene glycol > DMSO > Ethylene glycol > glycerol. Vitrification can always be done with use of the most toxic and penetrating cryoprotectants in high concentration if cryoprotectant toxicity was not a concern. However, the optimal cyroperservation protocol should be chosen based on minimizing toxicity and achieving greater viability of living specimen such as cells and tissues. Cryopreservation of tissues and organs is much more difficult than cryopreservation of small collections of cells. More time is required for cryoprotectant to permeate an organ. Another factor to consider is that the effect of cryoprotectant on an organ is complicated by the presence of many substances such as salts, proteins, fats, etc besides water. Therefore, the choice of cryoprotectant agent is based on empirical study with combination of type, concentration and cooling rate.

E. Choice optical clearing agent and cooling rate

The 50% V/V (volume/volume) glycerol/ phosphate buffer solution (PBS) was chosen as optical clearing agent for various frozen mouse tissues study. The melting/freezing point of pure glycerol is about 17.8°C. The freezing point of 67% glycerol/water mixture results in the coldest temperature at -46.5°C. However, concentrations of glycerol greater than 55% V/V are too viscous and toxic for cryonics use [C50]. The 50% V/V Glycerol/PBS solution has -23°C freezing point [The Merck Index]. The refractive index of muscle at 632 nm has been found as 1.38 and it is comparable to 50% glycerol 50% PBS solution [C42].

Crystallization from water cooling can be avoided by using cryoprotectant. A 68% V/V glycerol/water solution will not crystallize at any subzero temperature; will vitrify completely [C56]. It is noticeable that complete vitrification is not necessary in order to avoid freezing damage. It is found that organ has some tolerance for ice crystallization. For example, it is known that some species of frogs can spend days with as much as 65% of their total body water as ice due to protection from glycerol manufactured by their livers. Audrey Smith demonstrated that hamsters would be slowly cooled to -1°C, and 60% of brain water is turned to ice crystal with no gross loss of normal behavior upon thawing [C55]. Using the finding that at least 60% of the brain can be frozen without neurological damage, gives: minimum glycerol volume requirement $V_m = 68 - 0.68(60) = 27.2$. Therefore, 27.2% V/V glycerol should be sufficient to prevent ice-crystal damage to brains cooled to any subzero temperature. Another example is a series of experiments where cat brains was cooled to -20°C in 15% V/V glycerol (resulting in 62% brain water as ice) for years, and cat brains showed regular EEG patterns upon thawing [C52, C53].

Cell membranes are commonly believed to be the part of cells most vulnerable to freezing damage. According to tissue freezing theory, intracellular freezing is fatal for the cells, whereas extracellular freezing is not necessarily fatal to some extent [C54]. Very important prediction from the freezing theory is that the rate of cooling varies affect outcomes of freezing effect. In theory, vitrification can be achieved by using a small amount of cryoprotectant and by cooling at fast rate to avoid nucleation. However, rapid cooling creates stress when the warmer core needs to contract more than the cooler surface because cooling occurs from outside to inside. This may be the reason why slow cooling reduces tissue damage. Extracellular vitrification prevents cell membranes from coming in contact and fusing. Less cryoprotectant is needed inside cells than in the extracellular space because of dehydration which drives water

from cells into the extracellular space and because cells naturally contain proteins that enhance vitrification. For these reasons, use of non-penetrating cryoprotectants can assist vitrification because most nucleators are extracellular and because dehydration allows for intracellular vitrification by bound water. This loss of intracellular fluid has two effects. First, the increased solute concentrations make cells more resistant to freezing. Second, if a cell does freeze, the resulting ice crystals are much smaller, and they do less physical damage to intracellular organelles. Among different rates of cooling available, 1 °C/min cooling rate will be used in optical clearing effect study at subzero temperature as recommended by the "Nalge Nunc International Inc." as an optimal cooling rate. The 50% glycerol 50% PBS solution will be used for its less toxicity, and its cryoprotectant nature to maximize viability of tissue in freezing. Procedures and results of the frozen optical clearing study, its advantages, limitations and future will be discussed.

2.3.2 Experimental Methods

A. Two-photon imaging system

The experiments were performed using a typical TPM comparing the effects of optical clearing agents on fresh, fixed, and frozen tissues. The excitation light source used is a mode-locked Ti-Sapphire (Ti-Sa) pulsed laser with about 100 femtosecond pulse width (Tsunami, Spectra-Physics, Mountain View, CA) pumped by a continuous wave, diode-pumped, frequency-doubled Nd:YVO4 laser (Millenia, Spectra-Physics, Mountain View, CA). The excitation wavelength is tunable from 700 nm to 1000 nm. Mostly, 780 nm and 890 nm excitation wavelength were used. Both of the polarization and the power of excitation light at the specimen are controlled by a half wave plate (CVI Laser Inc., Putnam, Connecticut) and a Glan-Thomson polarizer. Typically, tissue imaging is conducted with an average laser power of about 3 to 30 mW at the sample plane. A computer-controlled galvanometric x-y scanner (6350, Cambridge Technology, Watertown, MA) deflects (raster-scans) the laser beam across the specimen. The excitation beam is coupled into an inverted microscope (Axiovert 100TV, Zeiss Inc., Thornwood, NY) via a modified excitation light path. The scan lens is positioned such that the x-y scanner is at its eye-point while the field aperture plane is at its focal point. The excitation light is reflected by the dichroic mirror to the objective. Since the objectives are infinity-corrected, a tube lens is positioned to re-collimate the excitation light. A 1:10 beam expander consisting of the scan lens and the tube lens ensures that the beam overfills the objective's back aperture and the full

numerical aperture of the objective is used, thus achieving diffraction limited focusing. The scanning mirror is in the telecentric plane of the back aperture of an objective lens so that the excitation beam is stationary on its back aperture independent of the motion of the scanner mirror. The high numerical aperture is essential for the formation of a diffraction limited spot on the order of 0.1 femtoliter. The objectives used in this system were a 40X oil immersion lens with 1.3 NA, and a 25X glycerol immersion lens with NA (Zeiss). The objective lens generates the excitation light in the sample plane in the specimen. The specimen was scanned with a single focus of excitation light and the emission photons were collected with a PMT. The scanner mirror moves the excitation beam in the sample plane in a raster pattern to cover the whole 2-D sample plane. The size of 2-D image was approximately 120 μm by 120 μm containing 256 by 256 pixels. The input power was 200 mW after polarizer. The frame rate is approximately 0.38 frames/s corresponding to a pixel dwell time of 40 μs.

B. Equipment and initial frozen optical clearing study

In order to keep the tissue specimen under 0°C while imaging, a device prototype was designed and implemented for imaging frozen specimens. This device was machined from acrylic. The main function of this device was first to hold and place the specimen, and second, to keep the temperature of the specimen below 0°C while we are performing two-photon imaging, mainly working as a cold temperature reservoir. As a preliminary experiment on frozen specimens, a quick study on the mouse heart tissue was done (figure 2.6). Fresh mouse heart tissue was cleared with 50% glycerol, 50% PBS for 4 hours as previously described. The specimen was placed in -20°C freezer. During imaging, we have observed thin crystal structure formed at the interface of objective and immersion oil. The resultant image quality was so poor that no structural information was obtained. We have switched to 25X multi-immersion objective, and used 50% glycerol as an immersion medium. There was no interface problem as with use of 40X objective. With rapid freezing in a -20°C freezer, optical clearing effect was not apparent.

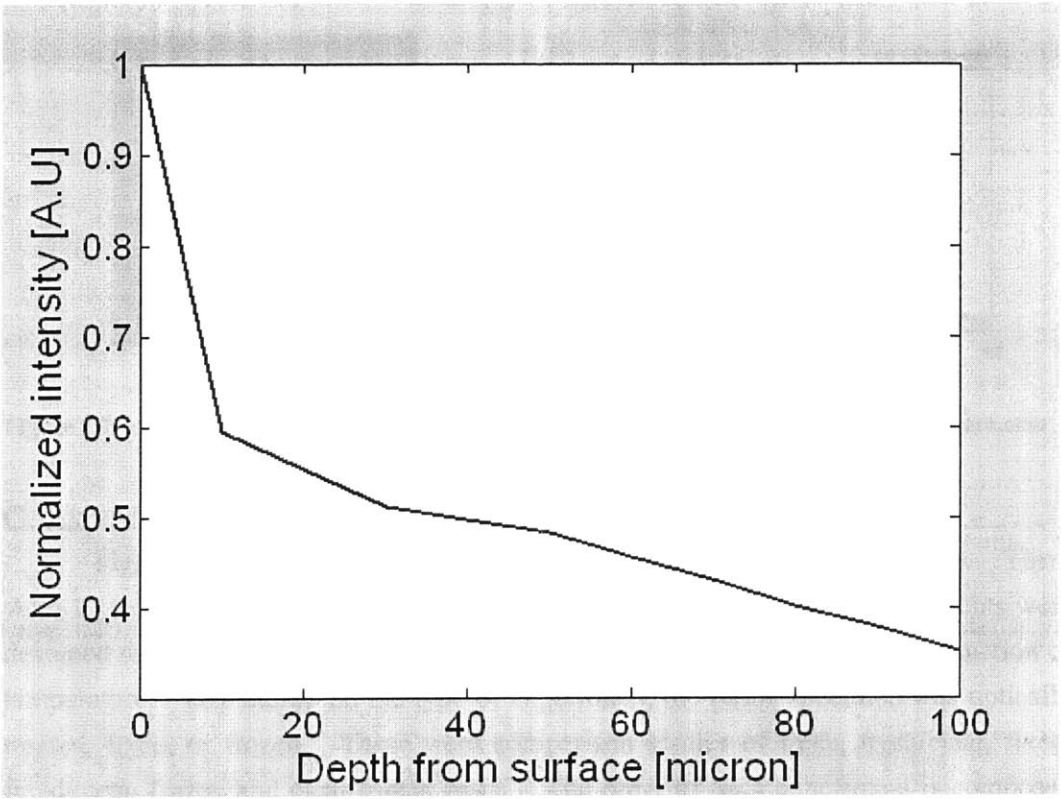

Figure 2.6. Initial study on optical clearing effect of a frozen mouse heart tissue sample using a -20°C freezer. Mouse heart tissue was treated with 50% glycerol solution for 4 hours and kept 4 hours in -20°C freezer. Excitation wavelength is at 780 nm. Intensity sum of all the pixels was computed along depth. This intensity sum was normalized with respect to the intensity sum at the surface.

This result indicated the possibility that finding an optimal cooling rate is important. We have found the commercially available cryogenic devices, Mr. Fosty (figure 2.7), for achieving optimal cooling rate of 1°C per min, according to Cryo-preservation manual by Frank. P Simione, M.S. of ATCC in cooperation of Nalge Nune International corp. 1998.

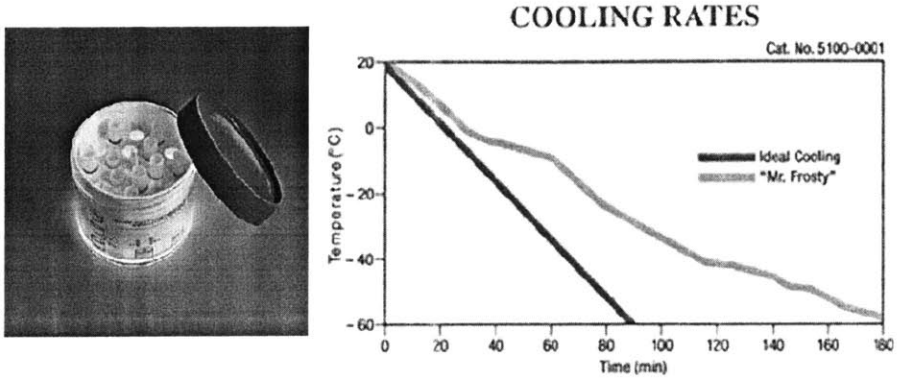

Figure 2.7. Mr Frosty and cooling rate used with -80°C freezer. http://www.nalgenelabware.com

C. Experimental procedure of optical clearing study

Figure 2.8 shows the experimental procedure of optical clearing study. There were 12 sets of experiments done using 4 types of different tissues. Experiments were designed to compare various combination of optical clearing efficiency as a function of temperature. Depending on the type of experiment, the tissue specimen was optically treated, fixed, or frozen. These were comparison studies of fresh, fresh/clear, fixed, fixed/clear, frozen and clear/frozen cases. The order of each experiment is composed of sample preparation, mounting and imaging. Tissue specimen was obtained from various mouse organs such as liver, heart, brain and pancreas. In sample preparation, the tissue specimen was cut in different size of 100, 200, 500 micron. The tissue sample was kept in PBS solution briefly and washed with PBS for several times in order to remove the blood. Fresh specimen was prepared by adding solution of 100% in PBS at pH 7. Fresh/clear specimen was prepared by adding solution of 50% in PBS and 50% in glycerol and kept it at 4°C for 4 hours. Fixed specimen was prepared by adding a solution in 4% paraformaldehyde overnight to crosslink the intracellular proteins followed by 70% ethanol solution overnight, and then prepared in 100% PBS solution. Fixed/clear specimen was prepared by fixation first with the same manner as described followed by adding a solution of 50% in PBS and 50% in glycerol and kept it at 4 °C for 4 hours. Clear/frozen specimen was prepared by adding solution of 50% in PBS and 50% in glycerol and kept it at 4 °C for 4 hours, followed by placement in Mr. Frosty which allows cooling at the optimal rate inside a -80°C freezer and for 4 hours. After specimen was prepared, specimen was mounted for imaging. The mounting devices at room temperature study and at subzero temperature study are different. For the studies at room temperature, specimen was placed between a coverslip and a glass slide with rubber isolator in order to maintain tissue shape. For the studies at subzero

temperature, the specimen is placed on a low temperature reservoir to keep the temperature of the specimen below 0°C while we are performing two-photon imaging. The current simple device is able to keep the specimen below 0°C for about 6 minutes which is sufficient for our investigation. 3-D imaging was performed at 10 micron axial. Imaging times are about 70 seconds or 95 seconds when 15 planes or 20 planes were imaged, respectively. Image analysis was followed to compare TPM intensity at different specimen depths. For mouse heart and liver study, all the intensity in FOV were simply summed to a value at each depth and compared. For mouse brain and pancreas, the pixels comprising the structures of interest were selected and summed to a value at each depth and compared.

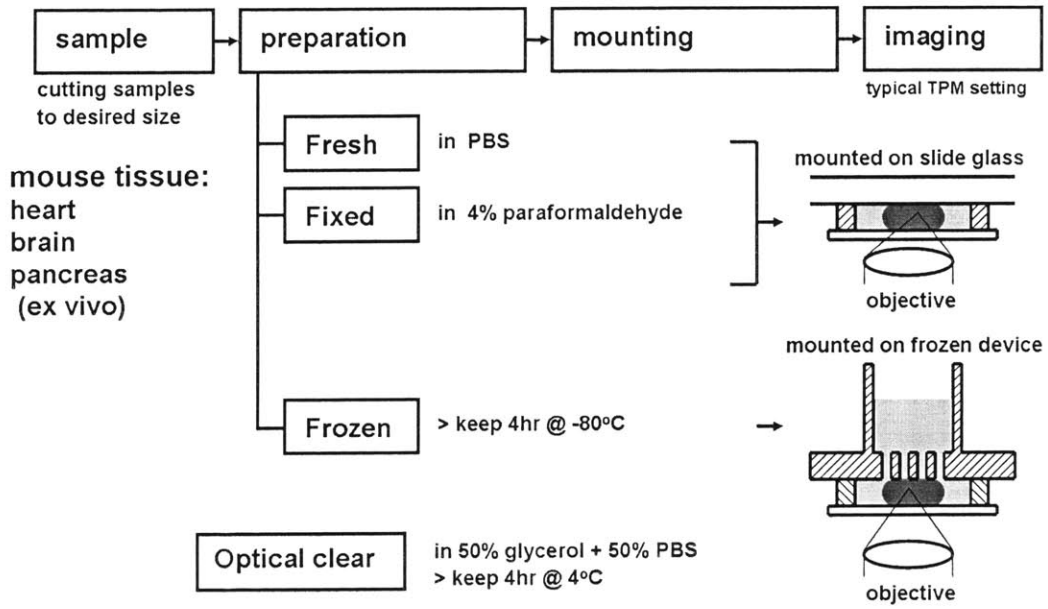

Figure 2.8. Experimental procedure of optical clearing study. Three mouse tissues were used for the experiments. Experiments were designed to compare various combination of optical clearing efficiency as a function of temperature. Depending on the type of experiment, tissue specimen was optically treated, fixed, or frozen. Fresh tissue specimens are excised and are imaged with minimal perturbation except refrigeration. Fixed tissue specimens are excised and subsequently fixed using standard paraformaldehyde procedure. Frozen tissue specimens are excised and subsequently frozen using cryoware, Mr Frosty with -80°C freezer for 4 hours. Typical TPM imaging was don. In order to keep the tissue specimen under 0°C while imaging, a device was designed and implemented for imaging frozen specimens. The main function of this device was first to hold and place the specimen, and second, to keep the temperature of the specimen below 0° C while we are performing two-photon imaging, mainly working as a cold temperature reservoir.

2.3.3 Results of TPM optical clearing studies

In order to understand the mechanism for optical clearing, specimens treated with optical clearing agent for different lengths of time can be compared. Fresh specimens were optically cleared by immersing the specimens in a 50% glycerol and 50% PBS solution for various periods of time. The time of optical clearing does not seem to affect the outcome. To study the effects of fixation, optical clearing has applied prior and after fixation. The specimens were fixed with 4% formaldehyde overnight to crosslink the intracellular proteins followed by 70% ethanol overnight. The fixed specimens were optically cleared also with a 50% Glycerol and 50% PBS solution. We have observed the optical clearing effect only for the optically cleared fresh muscle tissues which is consistent with studies by Campagnola *et al* [5] while fixed specimens show no clearing effects. Figure 2.9, 2.10, and 2.11 show the effect of optical clearing application time, and fixation on mouse heart tissue.

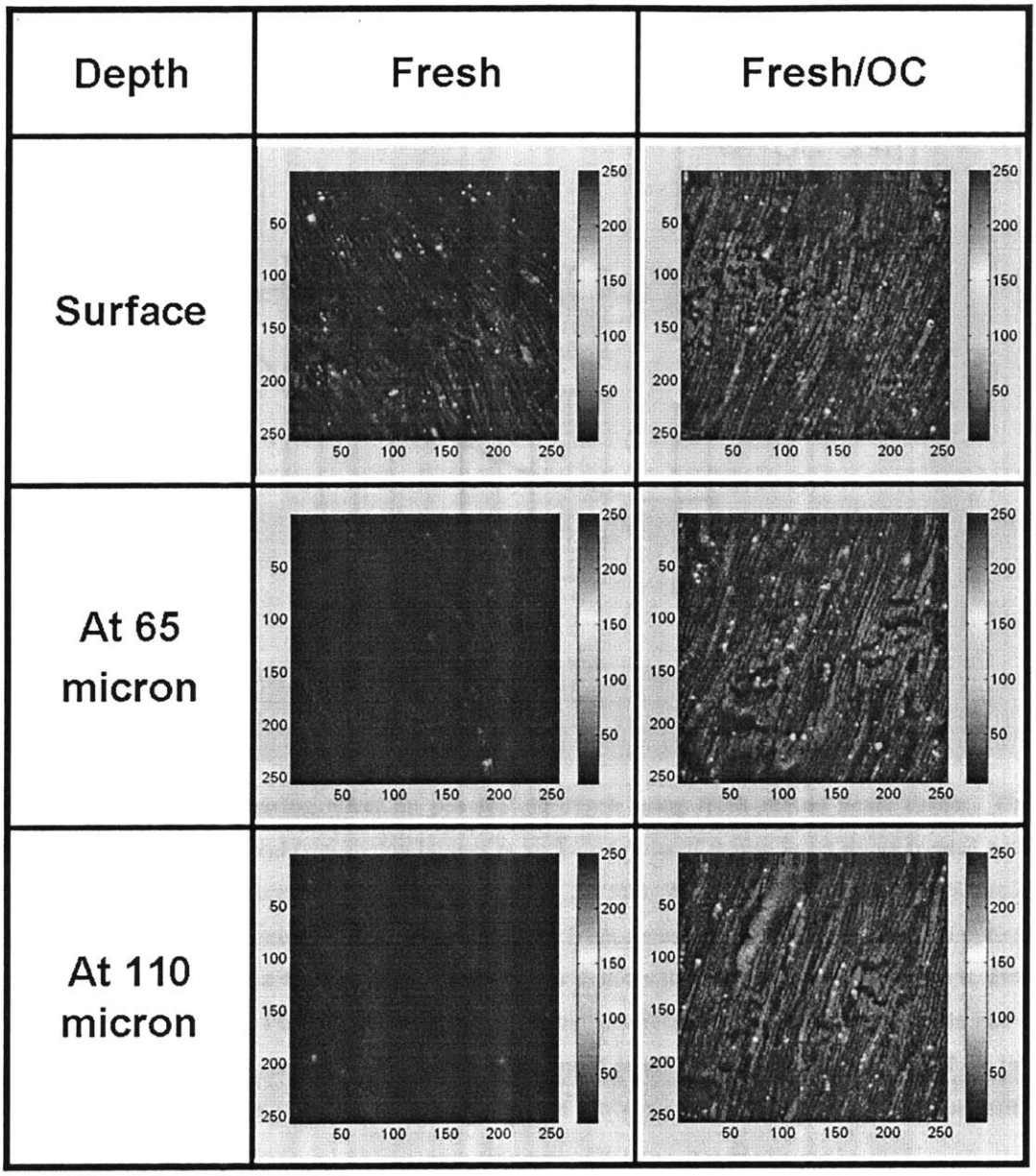

Figure 2.9. Raw image of TPM on mouse heart tissue. Raw image of two-photon microscopy at different depths were taken without optical clearing treatment (Fresh), and with optical clearing in 50% glycerol-treated (O.C. treated) mouse heart tissue for 4 h. Excitation wavelength is at 780 nm. Auto-fluorescence from muscle fiber is detected. The image quality is very poor with fresh tissue at 65 micron deep from the surface. On the contrary, the image quality with fresh tissue treated with optical clearing agent at 110 micron from the surface is as good as the one at the surface.

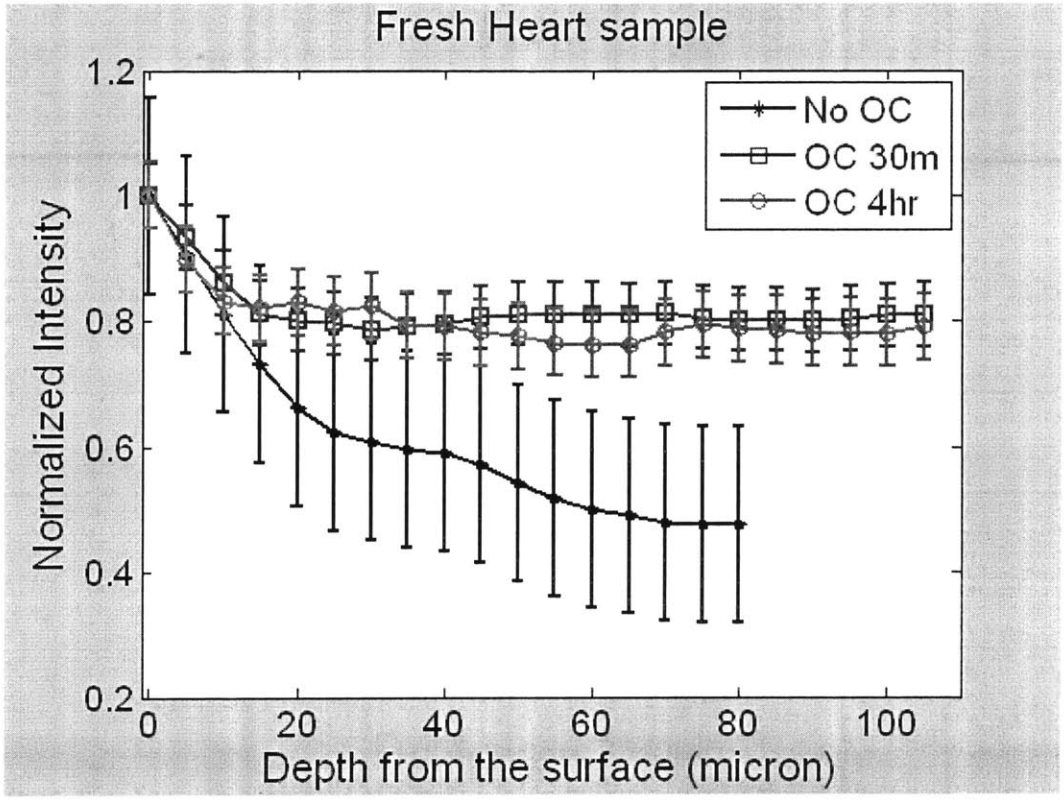

Figure 2.10. Optical clearing effect on penetration depth using fresh mouse heart tissue. The average intensity of several two-photon images at various depths of mouse heart tissue treated with 50% glycerol with different application time of 0, 30 min, 4 h. No OC denotes heart tissue specimens excised from mouse. O.C. 30min denotes fresh mouse heart tissue treated with optical clearing for 30 minutes in 4°C refrigerator. O.C. 4hr denotes the fresh mouse heart tissue treated with optical clearing for 4 hrs in 4°C refrigerator. Similar effect is observed for both 30 min and 4 h application of optical clearing. Excitation wavelength is at 780 nm. Intensity sum of all the pixels was computed along depth. This intensity sum was normalized with respect to the intensity sum at the surface.

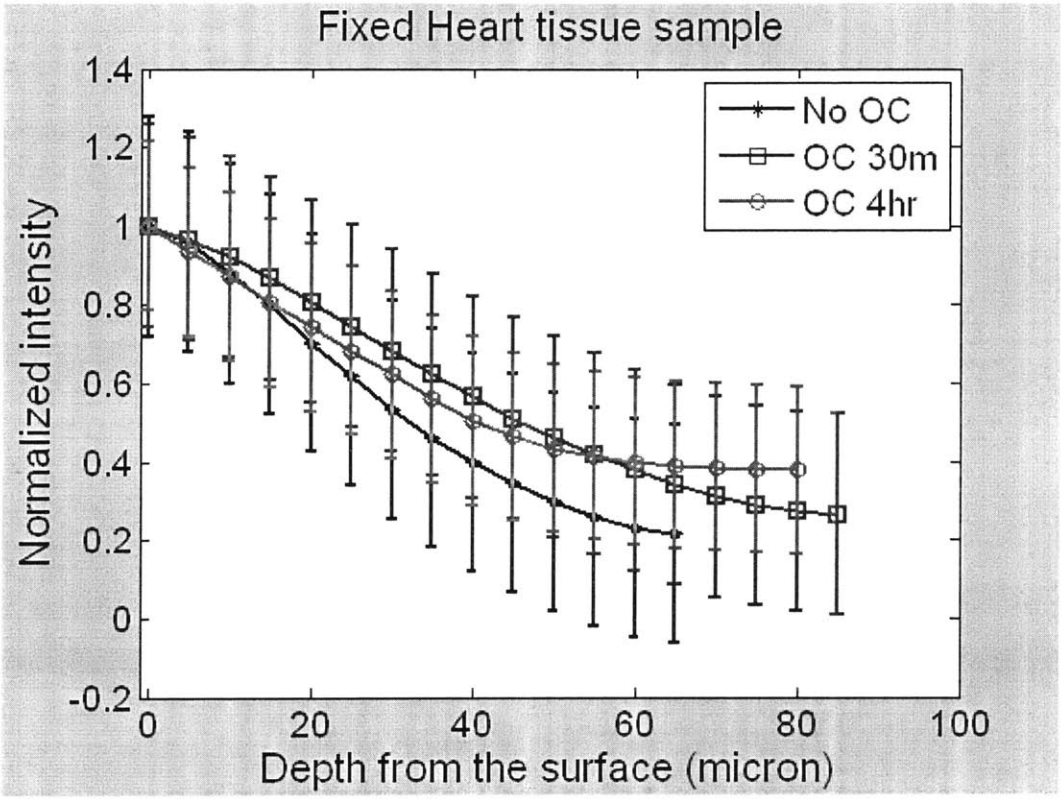

Figure 2.11. Optical clearing effect on penetration depth using fixed mouse heart tissue. The normalized average intensity of several two-photon images at various depths of mouse heart tissue treated with 4% paraformaldehyde fixation followed by applying 50% glycerol with 0, 30 min, 4 h. Fixed tissue specimens are excised and subsequently fixed using standard paraformaldehyde procedure. No OC denotes heart tissue specimens excised from mouse, followed by fixation. O.C. 30min denotes fixed mouse heart tissue treated with optical clearing for 30 minutes in 4°C refrigerator. O.C. 4hr denotes the fixed mouse heart tissue treated with optical clearing for 4 hrs in 4°C refrigerator. Each case, little clearing effect is observed. Excitation wavelength is at 780 nm. Intensity sum of all the pixels was computed at each depth. This intensity sum was normalized with respect to the intensity sum at the surface.

In order to study the effect of optical clearing on frozen specimen, three specimens were used. First mouse heart in three states were compared: fresh (fresh), optically cleared fresh specimen (OC 4hrs), and optically cleared frozen specimen (OC frozen). Figure 2.12 shows that optical clearing effect occurs on both OC and OC frozen case. There is more than factor of 2 increases in penetration depth.

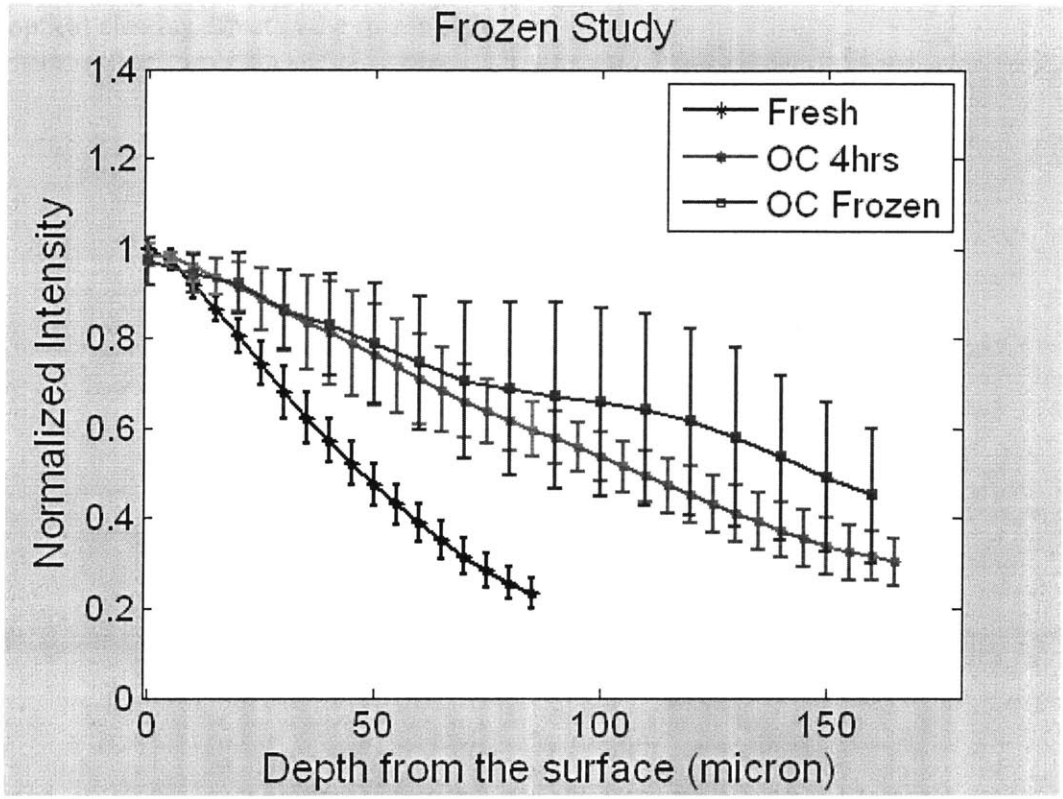

Figure 2.12. Optical clearing effect on penetration depth using mouse heart tissue at subzero temperature. The normalized average intensity of several two-photon images at various depths of mouse heart tissue treated with 50% glycerol with 4h at (A) room temperature and (B) sub-zero temperature compared with fresh case. Fresh denotes pancreas tissue specimens excised from mouse. Fresh/O.C. denotes fresh pancreas tissue treated with optical clearing for 4 hrs in 4°C refrigerator. O.C./Frozen denotes the pancreas fresh tissue treated with optical clearing for 4 hrs in 4°C refrigerator, followed by 4 hrs in -80°C freezer. Each case, optical clearing effect is observed. Excitation wavelength is at 780 nm. Intensity sum of all the pixels was computed along depth. This intensity sum was normalized with respect to the intensity sum at the surface.

Second, mouse brain was used to compare the effect on as it is (fresh), optically cleared, (OC 4hrs), and (OC frozen). Mouse brain was imaged from the surface where there are abundant dendrites and little cell body. The intensity level of dendrites and cell body are very different. For this reason, obtained raw image was processed to select only the dendrite structures, and if there were any cell body, it was intentionally avoided for image analysis (figure 2.13). Figure 2.14 shows that optical clearing effect occurs for both OC and OC frozen case. For both type of tissues, optical clearing efficiency is similar for both fresh and frozen specimen. Further, both mouse heart, more optically dense, and mouse brain, less optically dense, tissues show significant

optical clearing effect in the frozen state.

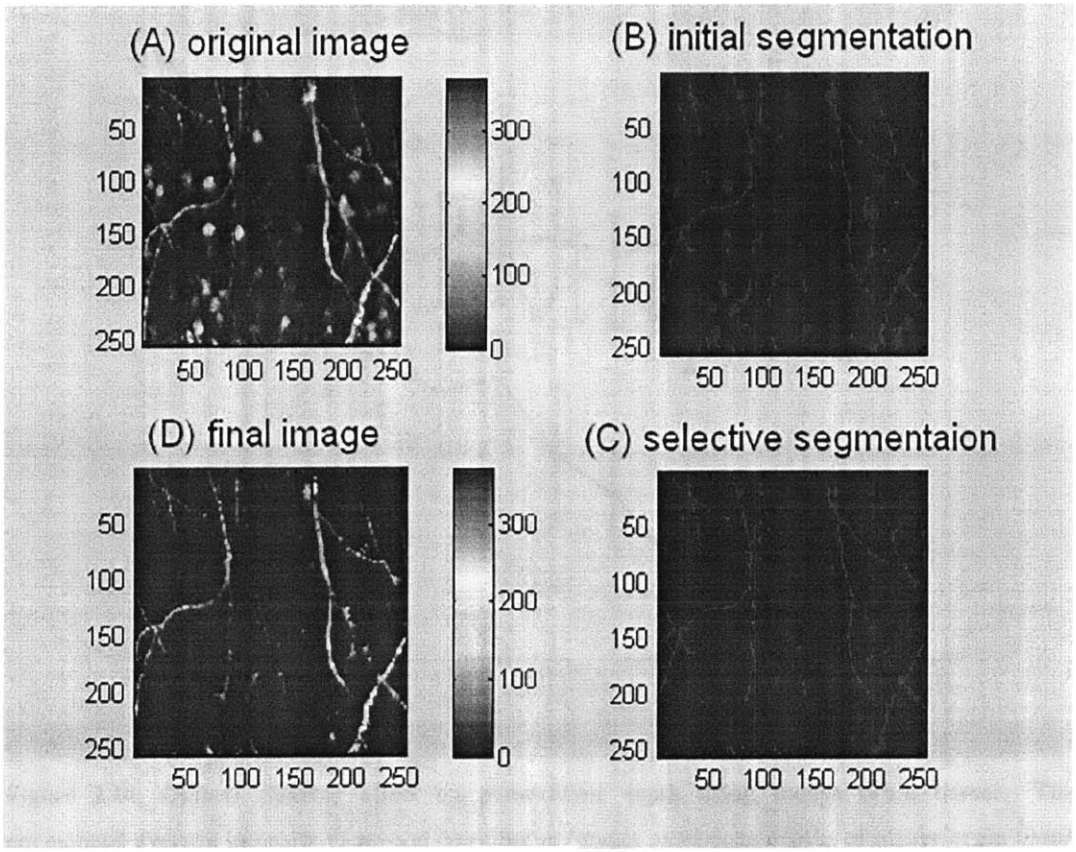

Figure 2.13. . Illustration of the image processing algorithm for discriminating and selecting mouse brain dendrites. (A) Raw image showing cell body and dendrites. GFP transgenic mouse was used for the experiment. Mouse brain was imaged from the surface where there are abundant dendrites and little cell body. The intensity level of dendrites and cell body are very different. For this reason, obtained raw image was processed to select only the dendrite structures, and if there were any cell body, it was intentionally avoided for image analysis (B) Binary image with threshold, erosion and dilation on raw image. Canny Edge algorithm was used for segmentation. (C) Selecting and deleting of cell body from segmented image. (D) Final image with only dendrites shown. This final image with only dendrites was used for calculation.

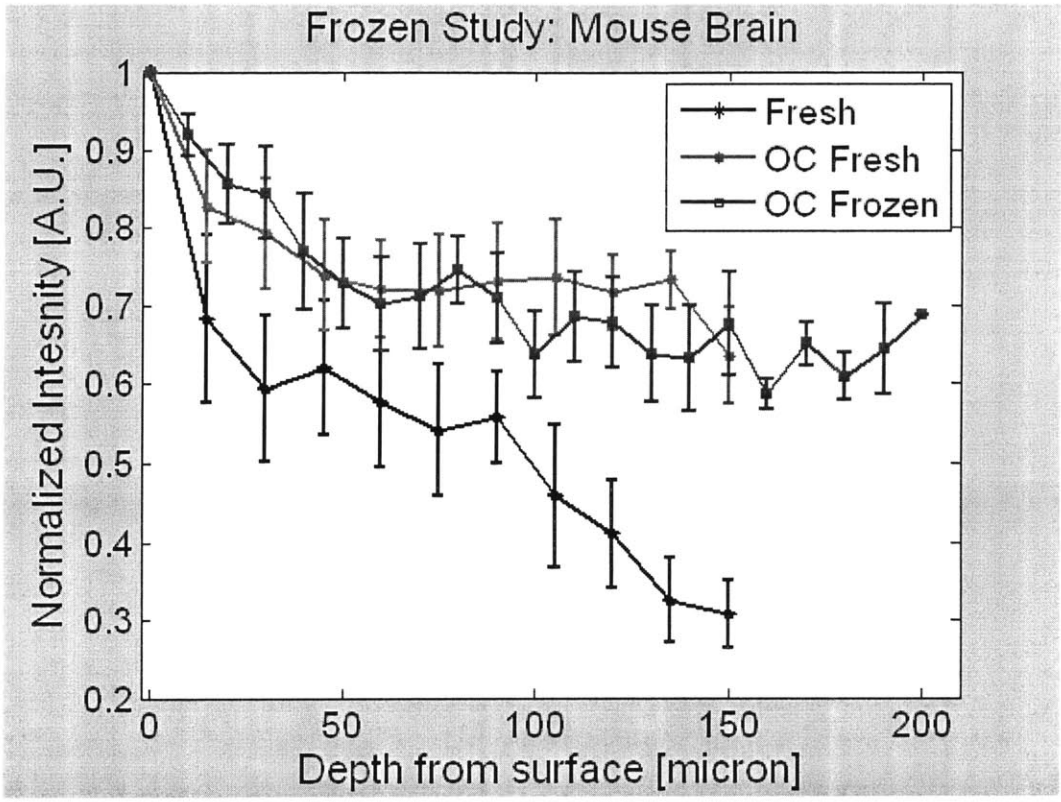

Figure 2.14. Optical clearing effect on penetration depth using mouse brain tissue. The normalized average intensity of several two-photon images at various depths of mouse brain tissue treated with 50% glycerol with 4h at room temperature and sub-zero temperature compared with fresh case. Fresh denotes brain tissue specimens excised from mouse. Fresh/O.C. denotes fresh brain tissue treated with optical clearing for 4 hrs in 4°C refrigerator. O.C./Frozen denotes the fresh brain tissue treated with optical clearing for 4 hrs in 4°C refrigerator, followed by 4 hrs in the -80°C freezer. Each case, optical clearing effect is observed. Excitation wavelength is at 890 nm. Intensity sum of all the pixels was computed along depth. This intensity sum was normalized with respect to the intensity sum at the surface.

Finally, we seek to study the effect of optical clearing on tissue structure. The mouse pancreas was imaged at three different conditions (fresh, optically cleared fresh, and optically cleared frozen). The volume change from optical clearing was evaluated by studying mean separation of nuclei in the tissue. The nucleus were stained with Hoechst 33234 and it was segmented in 2-D and reconstructed as 3-D object (see detail on FYDR study). The number of nuclei within specified volume (220 by 220 by 60 micron) was compared for each case. The volume of pancreas shrinks by 20% with optical clearing agent applied (figure 2.15).

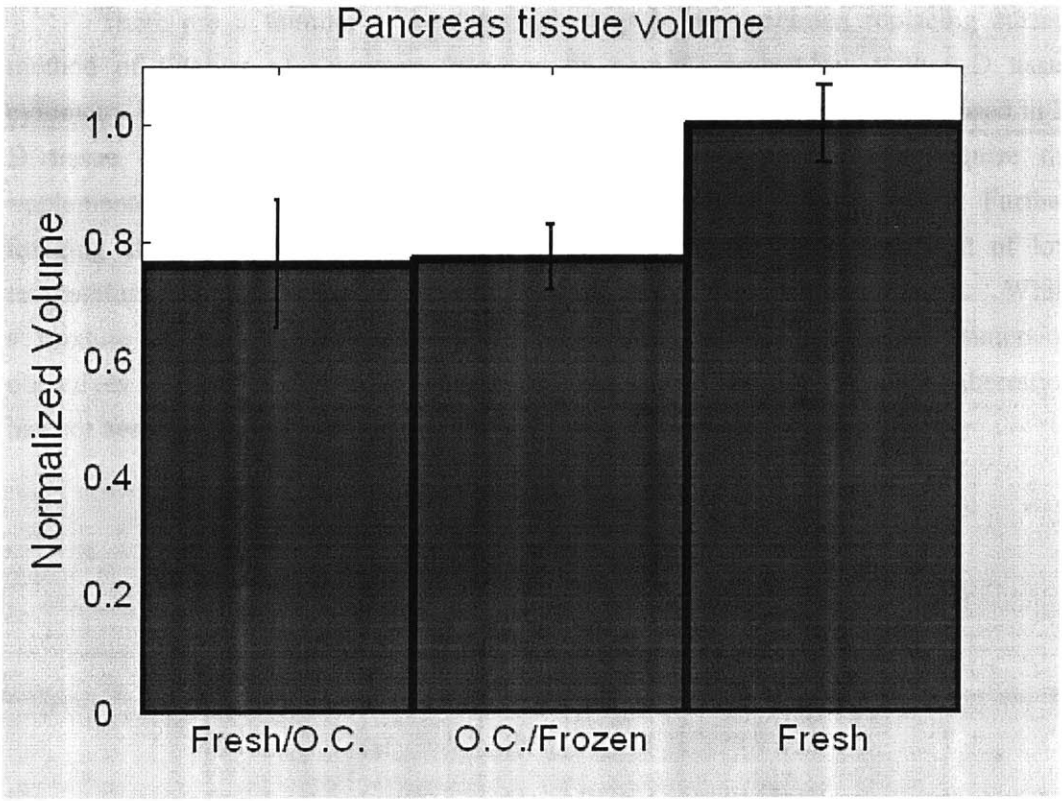

Figure 2.15. Study on volume change with optical clearing effect. Study on volume change with optical clearing effect was done by counting the number of nuclei in the same 3-D volume. Fresh denotes pancreas tissue specimens excised from mouse. Fresh/O.C. denotes fresh pancreas tissue treated with optical clearing for 4 hrs in 4°C refrigerator. O.C./Frozen denotes the pancreas fresh tissue treated with optical clearing for 4 hrs in 4°C refrigerator, followed by 4 hrs in -80°C freezer. The mouse pancreas was imaged at three different conditions (fresh, optically cleared fresh, and optically cleared frozen tissue). The volume change from optical clearing was evaluated by studying mean separation of nuclei in the tissue. The nucleus were stained with Hoechst 33234 and it was segmented in 2-D and reconstructed as 3-D object.

2.3.4 Conclusions

We have used 50% glycerol and 50% PBS solution as an optical clearing agent for heart muscle, brain and pancreas tissue, and found that there are more than 2 fold increase in achievable depth at room temperature. Comparing fresh and fixed specimens, we have observed the optical clearing effect only for the optically cleared fresh muscle tissues which is consistent with previous studies by other group using different imaging modalities. Effect of frozen tissue specimen was further investigated. We found that fresh and frozen specimens show similar degree of optical clearing.

There are a number of benefits of using frozen specimen replacing current method of fixation of specimen followed by paraffin embedding with 3-D tissue cytometry imaging. With frozen specimen, optical clearing approach can be used in 3-D tissue cytometry allowing deeper imaging. However, this will require the implementation of a cooling system with circulating optical clearing agent. Further, imaging at subzero temperature is also a challenge optically as the effect of low temperature on optical components such as an objective lens is not well known. While a mixture of 60% glycerol and 40% PBS solution allows the use of immersion objectives without ice crystal formation, the effect of this solution on optical aberration has not been quantified.

Chapter 3

Applications of 3-D tissue cytometry to biological studies

3.1. A study of mitotic homologous recombination with site-selective 3-D tissue cytometer

3.1.1 Introduction: biology of homologous recombination

Cancer is caused by multi-step processes through successive rounds of clonal expansion and selection of cells that have accumulated tumor gene mutations [D1-4]. Mutations that drive cancer development are often caused by DNA damage. Double strand breaks (DSBs) in deoxyribonucleic acid (DNA) are considered to be the most dangerous among DNA lesions, since genetic information loss [D5], or possible gross chromosomal rearrangements [D6] from imperfect repair, could cause mutation in the cell. Mitotic homologous recombination (HR) is a critical pathway for the accurate repair of potentially mutagenic DSBs [D7-12]. Mutations in inherited genes [D13-16] or exposure to chemical agent [D17] or radiation [D18] that modulate HR are associated with an increased risk of cancer [D19-20]. During DNA replication, homologous sequences are usually aligned perfectly. However, sequence misalignments and exchanges may occur and can lead to rearrangements that contribute to cancer. Clonal cell populations can appear to be phenotypically normal, even though they have acquired mutations. The ability to detect clonal expansion *in situ* within histologically normal tissue enables the identification of these clonal cell populations, and studying these cells may provide insight into the earliest stages of cellular transformation, prior to the clinical appearance of a tumor. Until recently, no methods had been developed to study clonal expansion within intact histologically normal tissue. The ability to study HR events *in vivo* was recently realized by using a tissue specimen from transgenic FYDR mice, where a HR event at an integrated transgene results in expression of a fluorescent protein [D21].

3.1.2 Previous studies

The pancreas is an organ that produces digestive enzymes or hormones such as insulin [D22]. Age is a key risk factor for pancreatic cancer [D23]. Previous work by Wiktor-Brown *et al* provided a rapid *in situ* imaging approach composed of wide-field imaging (epi-fluorescence microscopy) and using flow cytometer for identifying recombinant cells within intact pancreas tissue of FYDR mice in order to study the effect of aging on HR in the pancreas [D24]. She demonstrated that aging is the

factors that modulate homologous recombination and clonal expansion by showing an increase in the frequency of recombinant cells in the pancreas with age. FYDR pancreas tissue was imaged using epi-fluorescnce microscopy using filters specific for Hoechst-stained nuclei and enhanced yellow fluorescent protein (EYFP). Recombinant foci (a cluster of cells expressing EYFP in the tissue) can be directly detected within intact tissue by overlaying these images. Composite epifluorescence images show that recombinant cells accumulate in the pancreas of FYDR mice with age and that this accumulation results from both de novo recombination events as well as clonal expansion of previously existing recombinant cells. Wide-field imaging does not have any discrimination in depth. When a recombinant focus is present on the surface of the pancreas, the boundaries are distinct and it is possible to estimate the number of cells within the focus. However, for foci located below the surface, the scattering of emitted fluorescence prevents identification of specific cell boundaries. Also it is possible to recognize foci with bright intensity as bigger than its true size. Although clonal expansion was estimated using traditional epifluorescence microscopy, it was not possible to determine the number of recombinant cells per focus in 3-D using this approach. Thus, the extent of clonal expansion, an important precursor to tumor formation, could not be quantified. To overcome the depth resolution limitation of WFM, TPM microscopy was used. The use of two-photon tissue cytometry can overcome these limitations, thus providing high resolution images of fluorescent recombinant foci at a depth of up to 100 μm within pancreas tissue of FYDR mice.

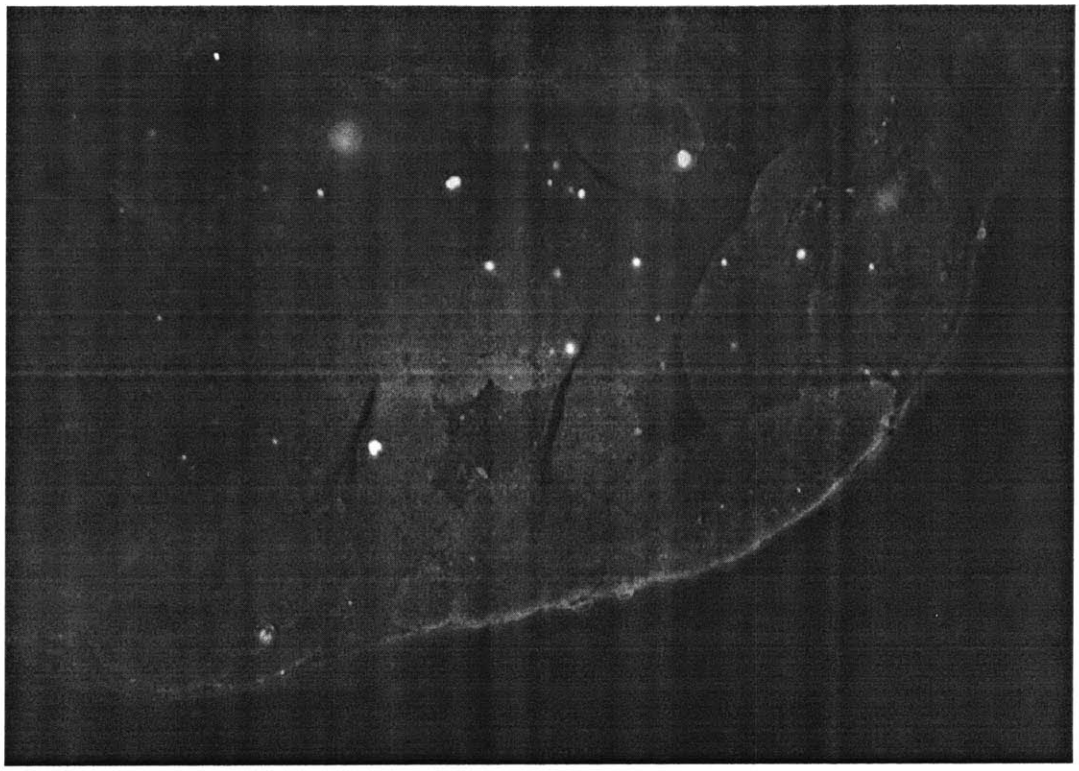

Figure 3.1. EYFP recombinant foci detection using WFM in pancreatic tissue. Image is from Wiktor-Brown DM *et al.* PNAS (2006) 103:11862.

3.1.3 3-D site-selective high-throughput tissue cytometry

There is a large amount of variation in cell behavior, even under the same experimental conditions. One challenge in bioimaging studies is to increase the rate of data acquisition such that a sufficient amount of data can be collected to overcome the inherent variances in data population. A new imaging technique, site-selective high throughput 3-D Image cytometry, has been developed and implemented to study a large tissue volume in the smallest possible time. The system is realized with a conventional TPM with the addition of fluorescence microscopy and the incorporation of automated specimen positioning x-y stage. Applying this technique to study the recombination foci in the pancreas of FYDR mice, we seek to quantify the distribution and the clonal expansion of cells that undergo recombination during cell division. In a given foci, morphological information of EYFP expressing cells such as, their brightness, and their size, can be quantified from the TPM images. Specifically, in order to study the effect of aging on recombinant cell frequency, we analyzed pancreas tissue from two age groups, 'juvenile' (4 weeks aged) and 'aged' (70+ weeks aged).

The design of the site selective, high throughput 3-D cytometer has been described in the Technology section, Chapter 2. The specific experimental parameters for this study are enumerated below. For TPM, we used a 20X 0.75 NA objective resulting in a FOV of 240 um by 240um. Around 50 layers were imaged in each section with a 1 μm depth increment. This depth range covered about 3 to 4 layers of cells spanning the full thickness of typical recombination focus. The acquisition speed was approximately 0.05 frames per second. In order to achieve reasonable statistical accuracy, we have studied at least 60 foci for both age groups. Two-photon microscopic analyses were carried out on female FYDR mice aged 4 weeks, and 67-74 weeks. All animals were housed in a virus-free facility and given food and water *ad libitum*. In order to visualize nuclei in isolated tissues, Hoechst staining dye was administered via retro-orbital injection with help from experienced veterinary technicians to minimize pain and distress for the animals. The mice were anesthetized using isoflurane as inhalational anesthetic in a precision vaporizer at a working concentration of 1 - 4%. Duration of anesthesia was 10 - 20 seconds only. Single retro-orbital injection of 0.04 mg Hoechst per gram of mouse body weight (volume not exceeding 0.2 ml) was performed using 26G syringe 20 minutes prior to sacrifice. Hoechst stock solution was prepared by dissolving Hoechst 33342 powder (Invitrogen) in sterile phosphate buffered saline (PBS, pH 7) at a concentration of 5 mg/ml. Mice were humanely sacrificed by CO_2 asphyxation. Whole pancreata were isolated, rinsed and soaked in PBS (pH 7.4) containing ice-cold 0.01% soybean trypsin inhibitor (Sigma). This pancreas is relatively soft and can be readily molded to fit the specimen holder. Pancreas tissue was uniformly compressed between two coverslips separated by 0.5 mm spacers. First, WFM was used to identify possible EYEP cluster locations. Biological specimen was placed on stage. The objective used was a low magnification of 1.25X Olympus Plan Apo with 0.04 NA (Olympus, Center Valley, PA). In combination with a Pander CCD camera for detection, the FOV of this system is 4.7 mm by 6 mm. The time required for imaging pancreas with adequate SNR using WFM is about 10 seconds per frame. Since the specimen is bigger than a single FOV of the WFM, a series of WFM imaging were taken using automated x-y stage traveling 5 mm and 4 mm along x and y direction, respectively. The communication with the robotic x-y stage was established via the serial port. Image stacks were taken with region of overlaps: about 1 mm in width (along x direction) and 0.67 mm in length (along y direction). These overlap regions allowed us accurately montage these imaging together via a stitching operation. After the composite image is formed, the locations for foci were identified and recorded so that the information is used for later

TPM imaging. A piezo actuator attached to objective lens was used to enable imaging at a maximum depth of about 200 microns. An automated x-y stage was used again in TPM to position the sample so the individual foci in the pancreas can be imaged one after another.

In TPM, both Hoechst stained nuclei and EYFP flurophores containing cytoplasm in FYDR mouse pancreas were simultaneously excited at 870 nm and their emissions were collected at the corresponding PMT channels. A 20X Zeiss Fluar, 0.75 NA working distance (WD) 0.6 mm objective was chosen in this application as a compromise between resolution and FOV. The sizes of most recombination foci in the pancreas were smaller than the FOV size of this 20X objective. Therefore there is no need to stitch images to locate the specific EYFP focus. On the other hand, it has a disadvantage of having less resolving power compared to that of higher even NA objective. Power of around 17 mW (measured after the objective with the use of a calibrated photodiode) was delivered to the pancreas tissue specimen with a pixel clock rate of 10 KHz. A power level of 200 mW and pixel clock rate of 10 KHz was utilized for TPM imaging of pancreas tissue specimen of both age groups. Pancreas tissue specimen degrades gradually and after 48 hours, it was not feasible for imaging with TPM. For the juvenile mouse, the number of foci is much less than that in aged mouse case. Therefore, it is a challenge to image enough foci from the younger mice. Intensity loss was found by imaging the same EYFP focus over time, and there were little change within 24 hours after harvest of the pancreas tissue specimen. Dehydration of the tissue was minimized by covering the specimen slide with careful wrapping with transparent tape. If the pixel clock rate were decreased, the SNR would increase assuming that all other factors remain the same. We chose a pixel clock of 10KHz pixel clock rate to maximize image SNR while minimizing data acquisition time. Considering the number of foci in the aged mouse found from WFM, we choose 10KHz to ensure that typically data acquisition time is within 12 hours. TPM data acquisition time for (256 x 256) pixels with these conditions was about 15 seconds per frame.

Two detector channels were implemented by using a dichroic mirror and two band-pass filters (Chroma Technologies, Brattleboro, VT). The nuclei which are visible from Hoechst 33232 staining allow counting the number of cells in the FOV. The emission filter set for detecting Hoechst stained nuclei in Blue channel is 470/40 where Hoechest absorption and emission spectra has maxima at 347 nm, and 483 nm respectively. The emission filter set for detecting EYFP in Green Channel is 530/40 since EYFP has absorption and emission spectral peaks at 513 nm and 527 nm respectively. Figure 3 shows the raw TPM images of FYDR rec mouse. The FYDR

rec mice are our positive controls. For the FYDR rec mice, all of the cells contain a copy of the recombined gene and are capable of expressing EYFP. However, it was found that there are many cells without EYFP expression and also the intensity of expressing EYFP varies from cell to cell. This was done by simple image analysis and results are shown in figure 3.2.

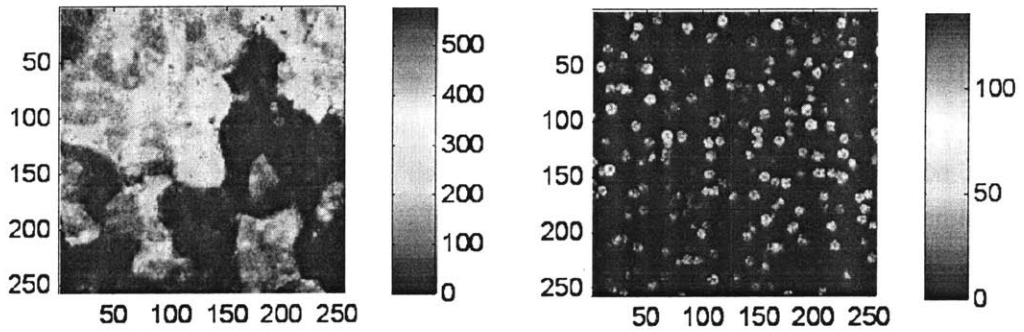

(a) Green Channel (b) Blue Channel

Figure 3.2. Image optimization study for pancreas tissue from FYDR rec mouse. These images were taken with 200 mW power and 10KHz pixel clock rate, where EYFP recombinant focus shows up in the green channel (A), and nuclei shows up in both green and blue channel (B). Green channel and blue channel have the signal of intensity collected the emission wavelength mostly from 510 nm to 550 nm, and from 450 to 490 nm, respectively. This nuclei intensity breakthrough from the blue to green channel was corrected in image processing. The color used in image is pseudo, and it is showing only the intensity level. FOV with 256 by 256 image is about 240 by 240 micron.

After establishing the optimal imaging conditions, imaging on FYDR mouse pancreas was done. In the FYDR mouse, EYFP is only expresses in a cell when there was a HR event occurring at the transgene. The frequency of these cells is very low and occurs at a rate of approximately $1:10^6$. For this reason, note that the location of the cell clusters is first recorded with WFM and then details of 3-D of the cluster is imaged with TPM at high resolution using high throughput site selective cytometer. 3-D site-selective tissue cytometry was used to identify recombinant cells *in situ* for the study the mechanisms of mitotic recombination during aging. In this experiment, tissue specimens were freshly excised from the pancreas of selected transgenic mice. There were 7 juvenile mice at 4 weeks age and two old mice with more than 70 weeks of age used for imaging.

3.1.4 Image analysis

Images by TPM microscopy were analyzed in order to identify and to measure the morphology of relevant tissue organelles in 3-D. The TPM image stacks of pancreas tissue are sequential 2-D images with 1 micron incremental steps along the axial direction. The image stacks further contain two color channels of information from the identical FOVs. The blue channel has cell nuclei images while both the EYFP expressing cells and the nuclei are visible in the green channel in 3-D. These images are composed of pixels with values corresponding to intensity levels. The 256 by 256 pixels image has a FOV of 240 by 240 microns. While image processing and measurement are performed on the pixel level, these dimensions can be readily converted to actual physical sizes. In this study, we concentrate on the segmentation of EYFP cell clusters and their related nuclei structures. Segmentation is the transformation of a raw image into a reduced representation where regions in the 3-D image stack corresponding to objects of interest, e.g. the nuclei, can be individually identified. All of image analysis algorithms are written in Matlab (MathWorks, Natick, MA) and the accompanying image processing toolbox.

Pre-processing of the images from both channels is required as the first step. Image defects such as hot spots, mottle, and uneven illumination become especially conspicuous when the image is enhanced. As with any real-world source of data, microscopy images are noisy, mostly from the noise introduced by the detector and its electronics, specimen autofluorescence, and room light. There was noticeable breakthrough from blue channel nuclei signal to green channel cell cluster image due to the underlying nature of the emission spectrum of the dye. Green channel purification was done by subtracting blue channel signal reduced by a known factor (corresponding to the known amount of spectral breakthrough) from green channel signal. Second, a background noise threshold was set and used to remove low intensity pixels from our analysis. Thresholding is very effective in removing background noise and to improve the image SNR. Thesholding allows us to retain the significant information from image while neglecting regions of the image that has too low SNR to be properly analyzed anyway. The threshold values are set in the beginning analysis. This was done by taking a background image in tissue with no noticeable YFP expression establishing the background noise being less than 6 photon counts. Threshold was set at 7 to remove all the noise associated with electronics, autofluorescence and room light. After noise reduction, segmentation was done on each channel. Segmentation is the transformation of a raw image into a reduced representation where 3-D regions of the

image are interpreted as types of objects of interest (such as the nuclei or the cell clusters). Errors may be introduced in the analysis stages; for example, image segmentation is usually imperfect. The exact representation depends on the details in the implementation of the segmentation process. Thus, each phase in the image analysis should be as robust as possible to errors introduced in the previous phase. To select segmentation algorithm parameters, all segmented images were graded manually to check its validity.

In this study, we need to segment two structures: the EYFP cell clusters and the nuclei (figure 3.3 and 3.4). The methods for segmentation for both cases are slightly different and these segmentation procedures are performed on each 2-D images of a 3-D stack. The EYFP cell cluster boundaries were determined in the green channel images by applying a simple global intensity threshold. The input to this segmentation process is the preprocessed image of EYFP cell clusters. The output is a threshold image where pixels above the intensity threshold are labeled as 1, and pixels below the intensity threshold are labeled as 0, creating a bitmap of binary values, called a binary image. From the binary threshold image, a segmented image was produced by associating pixels that correspond to the same clusters. The association of a pixel to a particular cell cluster is done by examining its connectivity. Each 8-way connected set of pixels is marked as a distinct region of its own. Each connected group of pixels, corresponding to a distinct cell cluster, is further assigned a unique integer value as a label.

The segmentation of nuclei was done by applying intensity-based threshold followed by a watershed algorithm on the blue channel images. While the foci are sparse, the nuclei can be very closely adjacent to one another. In this case, global thresholding is not very effective in distinguish the presence of multiple nuclei while the watershed method is known to be more effective. The procedure for intensity based thresholding is similar to the previous discussion and will not be repeated. After the thesholding step, watershed is applied to break apart regions that may contain closely adjacent nuclei. To ensure the robustness of the watershed step, it is necessary to smooth the region boundaries by removing high frequency nose in the image. A 2-D Gaussian filter was applied to the image prior to the application of the watershed algorithm. The watershed algorithm first finds the local maxima of intensities within a region. The maxima are used as seeds. Sub-regions are grown from these seeds via a dilation process. These sub-regions grow until they come into contact with each other. These sub-regions are not merged at contact; instead, a boundary is placed where these two sub-regions intersect. As both sub-regions continue to dilate and grow, they do

not grow past this boundary. This dilation and growth process stops when whole region initially delinearated by global thresholding is filled. After segmentation, individual regions corresponds to the nuclei are labeled as described before. The input to this segmentation process is the preprocessed image of nuclei with noise removed as described earlier. The output is a segmented image where the intensity value of a pixel is a label that designates it a specific nucleus identified.

All the previous processing steps are done on 2-D images of the 3-D stack. After successful segmenting both the nuclei and the foci in 2-D, the connectivities of these object in 3-D need to be established. Each nucleus was identified by connecting 2-D nucleus images. Individual nucleus was reconstructed in 3-D by connecting 2-D nucleus segmentation through a 3-D image stack. This procedure was done in two steps. First, pixel connections were checked. Connectivity was assumed if any part of a 2-D nucleus was overlapping in terms of lateral coordinate with another 2-D nucleus on adjacent planes. From this, the entire 2-D nucleus segments comprising of the same nucleus was identified. Second, the two adjacent 2-D nucleus segments in the different z plane are checked by the distance of their centroids. Typical size of the nucleus in this tissue is approximately 10-15 micron. We require that the centroids of adjacent planes to be within 5 microns to be truly connected and to be counted as a single nucleus. All the nuclei in 3-D were identified and labeled by this manner. For labeling, each centroid at each plane is checked first, and if it is associated with a centroid from a previous plane, it is identified as the same nucleus. If a centroid has no associations from the previous plane, it initiates a new numbering. The reconstruction of EYFP recombinant focus in 3-D was done by considering only connectivity found from overlap in space. As described earlier, each 8-way connected set of pixels is marked as a distinct region of its own. This is sufficient since the foci are sparse.

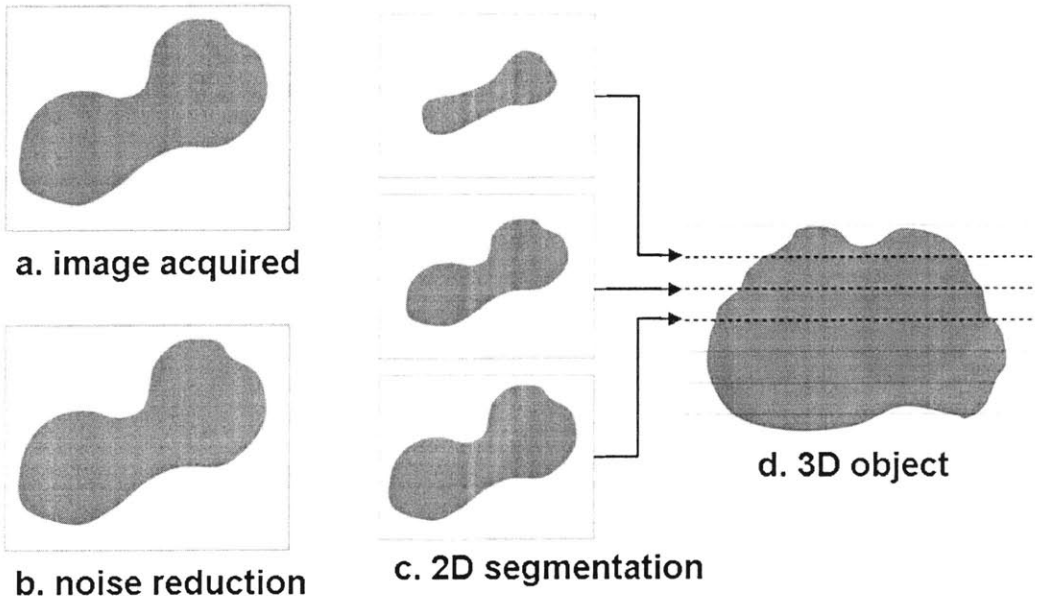

Figure 3.3: Imaging process procedure for obtaining 3-D EYFP cell clusters at one isolated focus site. Raw images (a) contain noise which was removed by filtering and setting the threshold. Using these noise free images (b) obtained at different depth, segmentation was done using 2-D segmentation algorithm. By carefully connecting by checking overlaps between adjacent 2-D EYFP segmented images, 3-D EYFP cell cluster is constructed.

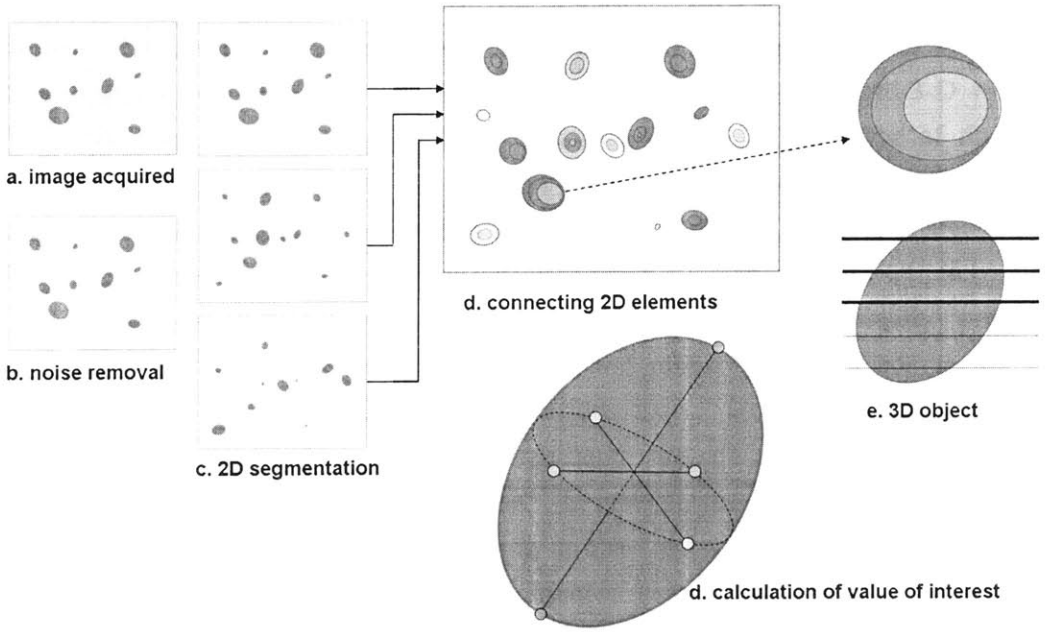

Figure 3.4: Imaging process procedure for obtaining 3-D nucleus. Image was obtained (a) and noise was removed (b) the same manner as described in EYFP cell cluster case. In 2-D segmentation, an additional operation such as applying watershed algorithm was applied in order to discriminate possibly clustered nuclei (c). Then the 2-D segmented images of a nucleus in adjacent planes were connected in terms of checking overlap and distances (between centroids), and realized as a 3-D nucleus. Various calculations can be done with this nucleus in 3-D using pixel and intensity information (e).

After successful segmentation and labeling of both nuclei and foci in 3-D space, the size and intensity values for all 3-D objects in each channel were established. The information was organized so that the information such as type of object (nuclei, foci) and object location in x y and z, etc were readily available. Since we are interested in studying HR event, nuclei outside of recombinant EYFP focus were not considered for analysis. Overlapped regions between EYFP recombinant focus and each nucleus are identified by observing the coordinates of their locations.

3.1.5 Algorithms development for morphological quantification

After segmentation and labeling, we are ready to quantify the morphology of these nuclei, foci, and their relative distribution. The statistics for standard deviation and mean values were determined for each morphological measurement. There are

quantitative results on the following parameters for each age group. First, total number of nuclei inside of each recombinant EYFP foci within specimen was found. Second, size of the each EYFP focus was measured in by its height and 3-D volume. Third, the intensity of the each EYFP focus was found. Fourth, size of the each nucleus was measured in by its 3-D volume. Fifth, the intensity of the each nucleus was found. Sixth, spatial distribution of the nuclei within a focus is characterized. Finally, the shape of entire nucleus was investigated by studying their ellipticity. The algorithm for each morphological measurement is validated visually prior to implementation. There were more advanced and robust validation approaches but current solutions seem adequate in this application.

Common to these morphological measurements are the need to compute an object's size, intensity, centroid, and shape. In general, the 3-D volume and intensity of an object were found by either summing up the comprising pixel elements or their intensities. Another useful value for an object is its centroid position in 3-D space. The centroid coordinates for each object (either nucleus or recombinant EYFP focus) in 2-D region were found from calculation of intensity weighted coordinate sum divided by the number of corresponding pixels. The centroid coordinates without consideration of intensity weighting were also computed. The values obtained with or without intensity weighted approaches were not that different and agreed within one micron. For each object, their size, intensity and centroid coordinates were recorded for further use. The number of nuclei in a recombinant EYFP focus was obtained by simply counting the number of nuclei that overlap recombinant EYFP focus in 3-D space. There are many shape descriptors useful in terms of characterizing the 3-D object. In our analysis, three principal axes, their lengths and orientations, were found for the entire nuclei. The principal axes are mostly aligned with the object's symmetry axes. Principal axes were found by computing tensor matrix, and eigenvectors associated by the tensor matrix. Since this tensor matrix was a symmetric, real matrix, it was possible to find a Cartesian coordinate system where it has only non zero diagonal elements; eigenvalues in three directions. Eigenvectors corresponding to these engenvalues were the unit vectors along the principal axes. Three lines starting from centroid of nucleus were drawn along positive and negative directions of the eigenvectors. Lengths of three major axes were found simply by finding distance between two points in the both ends of three lines. Two end points in each line were approximated by interpolating the adjacent pixel coordinates.

3.1.6 Results: quantification of recombination events

A. Visualization

Using WFM, a pancreas tissue was successively imaged at adjacent locations and stitched together afterwards. Figure 3.5 shows a typical image of WFM. Both sides of tissue specimen were imaged in order to obtain as much data as possible. WFM with 532nm continuous wave diode laser reveals only EFYP cell cluster sites, which were shown as circle white dots.

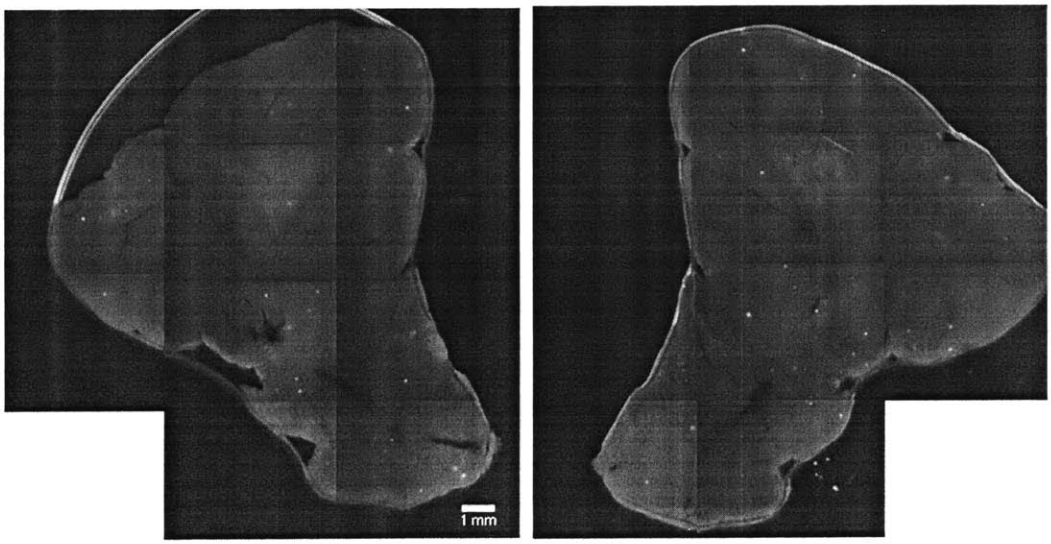

Figure 3.5. Typical WFM image of pancreas tissue of mouse pancreas tissue. Typical WFM by uniform illumination of continuous wave laser was done on mouse pancreas tissue. Fluorescence recombinant foci are identified and their x-y coordinates are mapped within the composite images. Smaller WFM images (5mm by 4 mm) were stitched to cover whole surface of the pancreas. WFM was done on one side (A) and on the other side (B). White scale bar indicates 1 mm.

From results of the WFM, the EYFP cell cluster sites were recorded and used for further imaging in TPM. To determine the extent to which one-photon microscopy distorts the true size of recombinant foci, a comparative analysis was performed for multiple foci collected by both epifluorescence and two-photon microscopy. Figure 3.6 shows both representative TPM and WFM imaging of pancreas tissue. Each square indicates the regions of TPM performed with 240 by 240 micron FOV. Comparing inset (A) and (C) shows that size of the EYFP cell cluster are very different, while they look similar with WFM image. Comparing inset (D) with inset (B) and (C) shows that the size of EYFP recombinant focus is the smallest of three, while it is the biggest with

WFM. Comparing brightness of EYFP cell cluster (inset (B) and (C)), EYFP cell clusters are much brighter in inset (C) on the contrary to the finding from WFM. These comparisons demonstrate the importance of true 3-D imaging in quantifying these recombination foci.

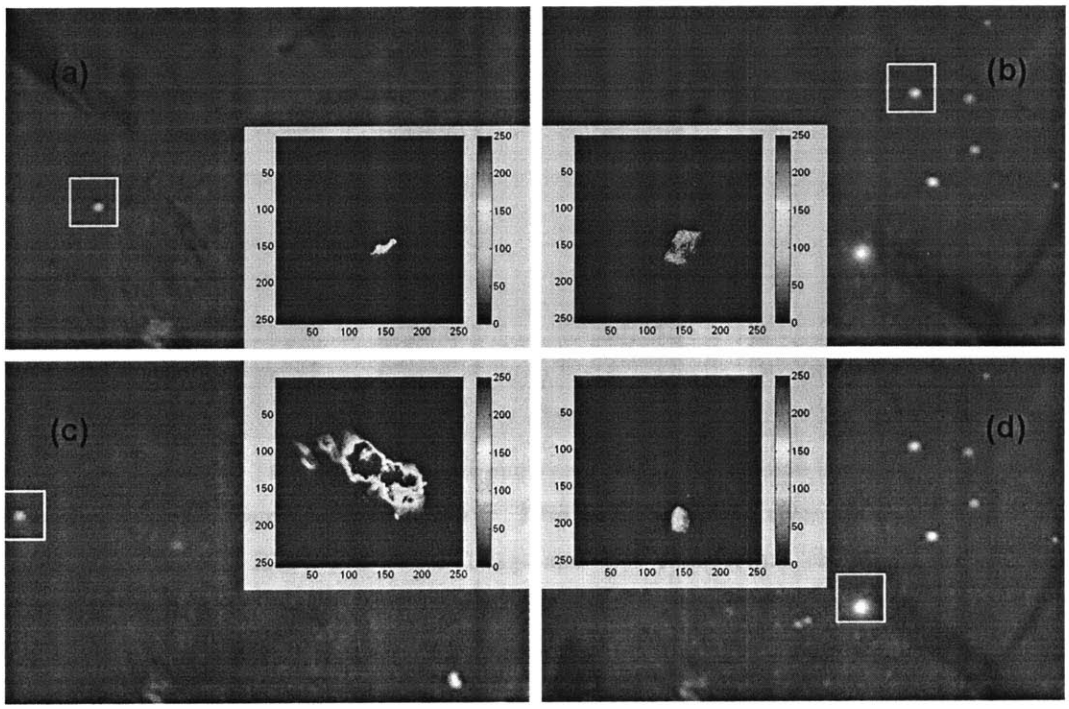

Figure 3.6: EYFP cell cluster size estimation using TPM and WFM. Foci showing similar size in WFM but having different sizes with different numbers of cells as revealed by TPM. Excitation wavelengths are 532nm, and 870 nm for WFM, and TPM, respectively. WFM identifies EYFP recombinant cell cluster and shows approximate size of each focus shown as a blurry white ellipse. These sites are imaged again with TPM. TPM image has two channel information of EYFP recombinant cell cluster (shown in the center) as well as the nuclei (not shown here). FOV is about 240μm by 240μm. Rectangles in white indicate the size and location of TPM imaging.

Each recombinant EYFP focus was imaged with TPM. Successive TPM images are taken at sites of interest along the depth. A 2-D TPM image has information on both EYFP cell cluster and nuclei in terms of their size and brightness. Figure 3.7 shows the typical 2-D TPM image.

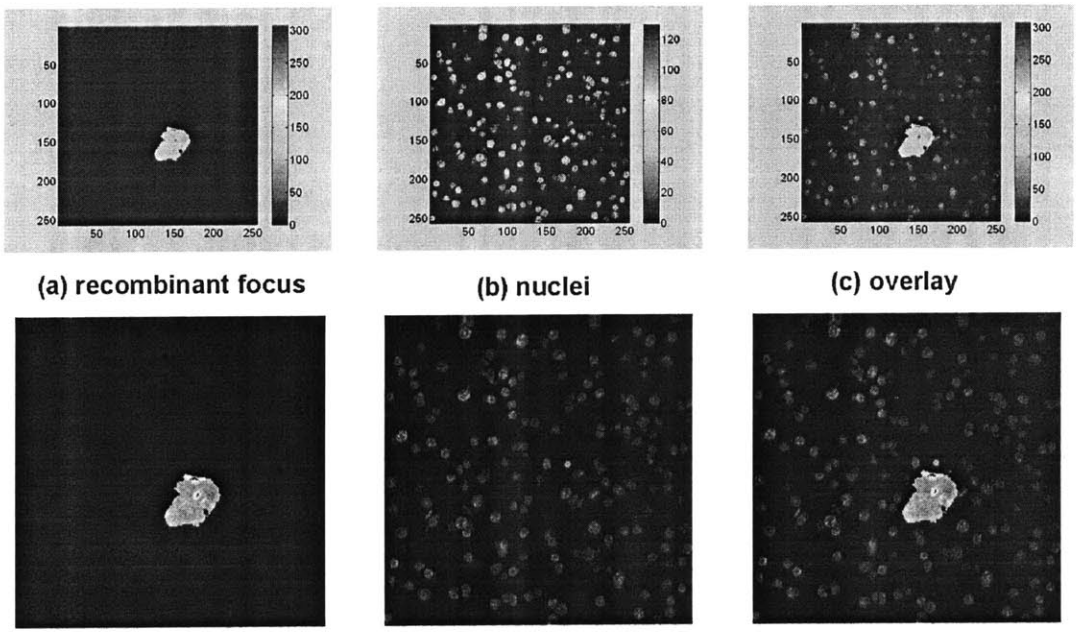

Figure 3.7. Typical 2-D TPM image of mouse pancreas tissue. Two-photon images are composed of two channel images from the identical FOV. TPM image is pseudo color images with intensity. Green channel has a EYFP cell cluster image and blue channel has cell nuclei images. By overlaying two features, we can identify the number of cells in the cell cluster.

Figure 3.8 shows the 2 channel images of both EYFP and nuclei at different depths. By combining these 2-D images at discrete planes with 1 micron incremental steps in z, 3-D reconstruction of the recombinant EYFP focus and nuclei was done using commercially available Imaris 5.0 software.

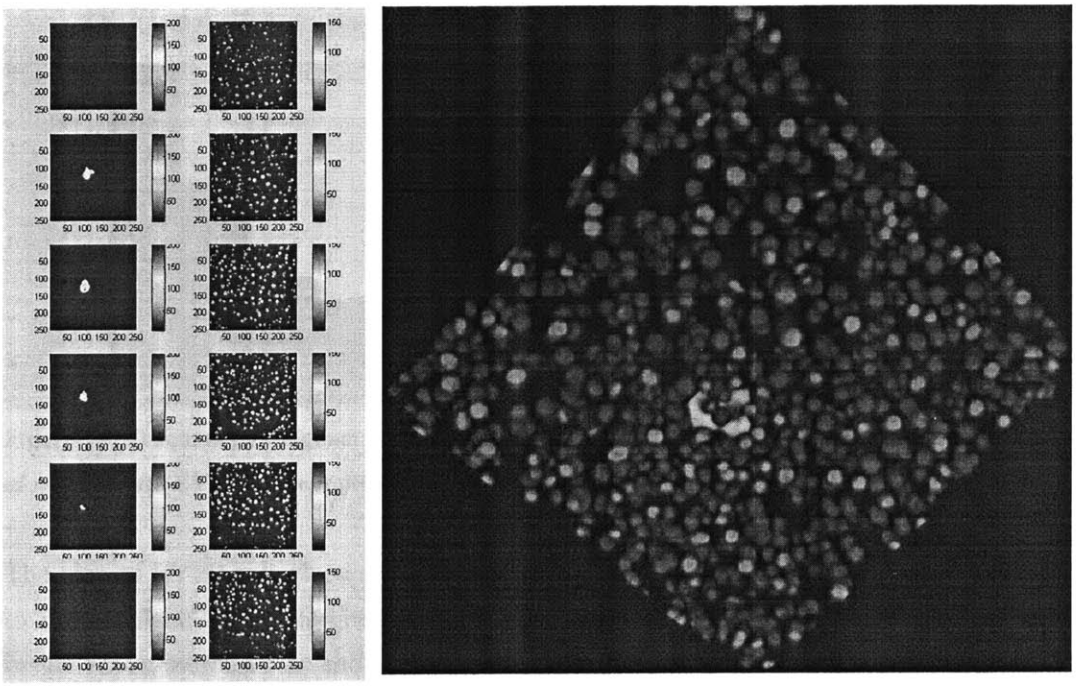

Figure 3.8. 3-D reconstruction of nuclei and EYFP cell cluster from TPM images of mouse pancreas tissue. TPM images (left) were taken at 870nm with 50 micron deep with 1 micron incremental step. FOV is 240 by 240 micron. By stacking 2-D images, 3-D volume image (right) was generated. There are 7 cells in the EYFP recombinant cell cluster.

B. Quantification of relative changes in two mouse age group

These statistics were acquired and analyzed for age effect on HR event in this study. The number of cells inside of EYFP cell cluster for juvenile mouse group varies from 1 to 5 from investigating 79 foci using 7 mice at 4 week old. The number of cells inside of EYFP cell cluster for juvenile mouse group varies from 1 to 53 from investigating 69 foci using 2 mice at more than 70 week old (figure 3.9). It was noted that there were 7 recently initiated HR events for the older mice. Of the foci analyzed in pancreas tissue of juvenile mice, the largest recombinant focus contained five cells. In contrast, about 40% of recombinant EYFP foci in aged mice contain more than five cells, with one focus containing 53 cells. Overall, from juvenile to aged mice, the median number of cells per focus increases from one to four cells.

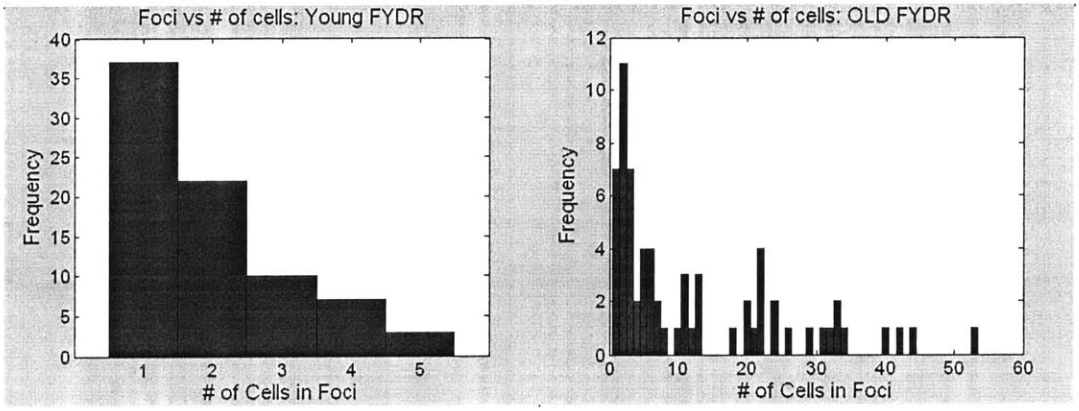

Figure 3.9. Frequency histogram for juvenile and aged mice. Frequency vs number of cells inside of recombinant EYFP foci was plotted for each case.

The size of EYFP cell cluster was measured in terms of its vertical height with respect to image plane. The height of EYFP cell clusters increases as the number of cells inside focus increases as shown in figure 3.10, and its linear fit curves at figure 3.11. Compared to the juvenile mouse, the clusters in aged mouse have a larger height. Average heights were found as 27 micron and 18 micron for aged and juvenile, respectively. The slopes of the fits measure the rate of cluster height increase to be 2.56 μm/cell to 0.6 μm/cell respectively. The size of EYFP cell cluster was also measured in terms of its volume. The volume of EYFP cell clusters increases as the number of cells inside focus increases as shown in figure 3.12. Average values are found to be 3791±3117 μm^3 and 3691±2973 μm^3 for aged and juvenile, respectively. Compared to the juvenile mouse, aged mouse has a similar cell size. Assuming spherical cells, their radii are about 10± 9 μm; and their volumes ares $4/3\pi r^3$. This radius is much larger than the rate of cluster height increase indicating that new clones are not expanding perpendicular to the tissue surface.

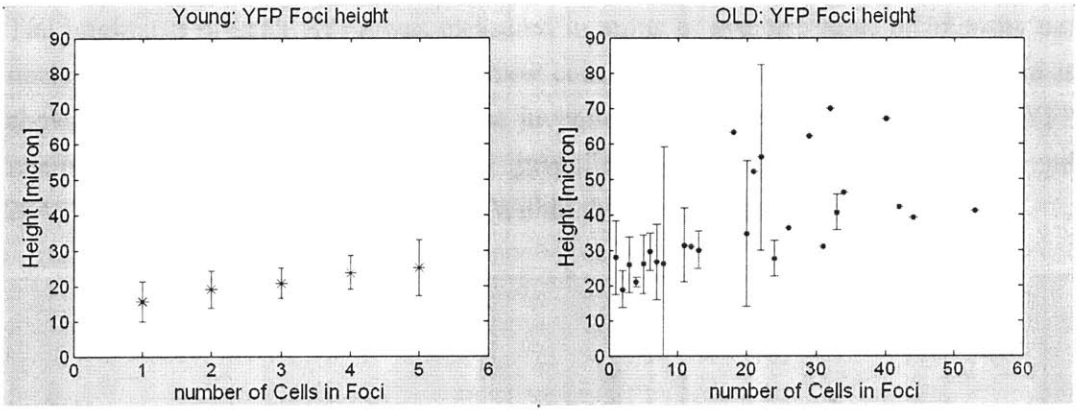

Figure 3.10. EYFP cell cluster height. EYFP cell cluster height vs number of cells inside of recombinant EYFP foci was plotted. The data point represents the average value with error bar if available.

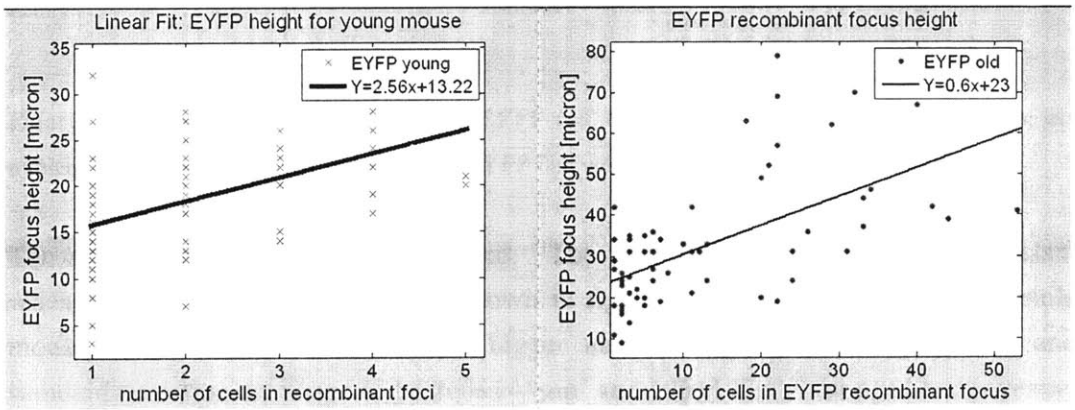

Figure 3.11. Linear fit on the YFP recombinant cell cluster focus. The R^2 values are 0.24 and 0.43 for juvenile and aged, respectively.

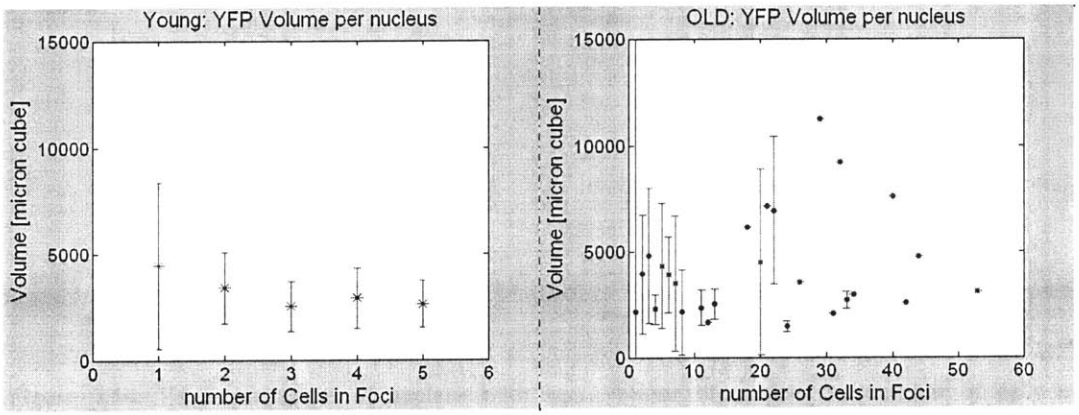

Figure 3.12. Volume changes of EYFP cell cluster with age. Volume of EYFP cell cluster per nucleus vs number of cells inside of recombinant EYFP foci was plotted.

The brightness of each EYFP was measured in terms of average value of intensity per nucleus. The brightness of EYFP is almost constant when it was plotted against foci as shown in figure 3.13. Compared to the juvenile mouse, aged mouse has twice EYFP intensity per nucleus for aged and juvenile are 618930±1100900 [A.U], and 284810±317069 [A.U.]) respectively. Within the error, they are similar.

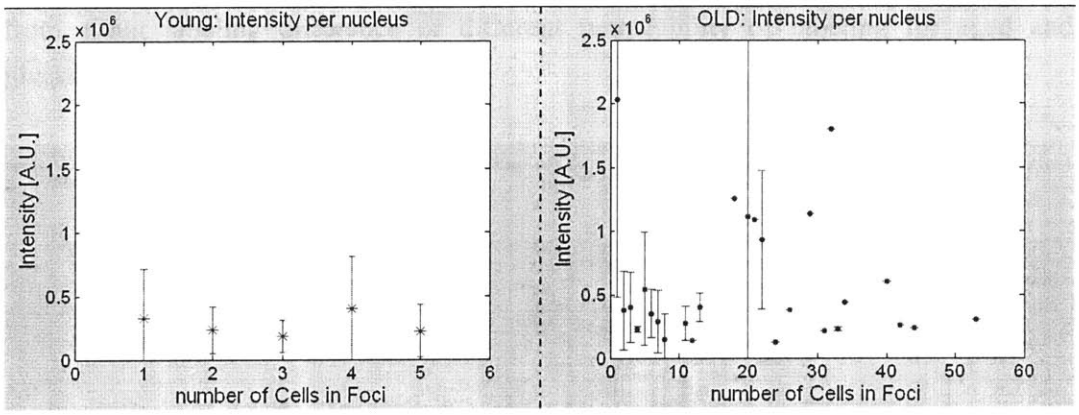

Figure 3.13. Age effect on brightness of EYFP cell cluster. EYFP cell cluster brightness per nucleus vs number of cells in recombinant EYFP foci was plotted.

The size of each nucleus was measured. The volume of nucleus is almost constant when it was plotted against foci as shown in figure 3.14. Compared to the juvenile mouse, aged mouse has a little bit bigger nucleus volume. Average values and standard deviation are found to be 260±141μm^3 and 196±177μm^3 for aged and juvenile, respectively They are very similar in size.

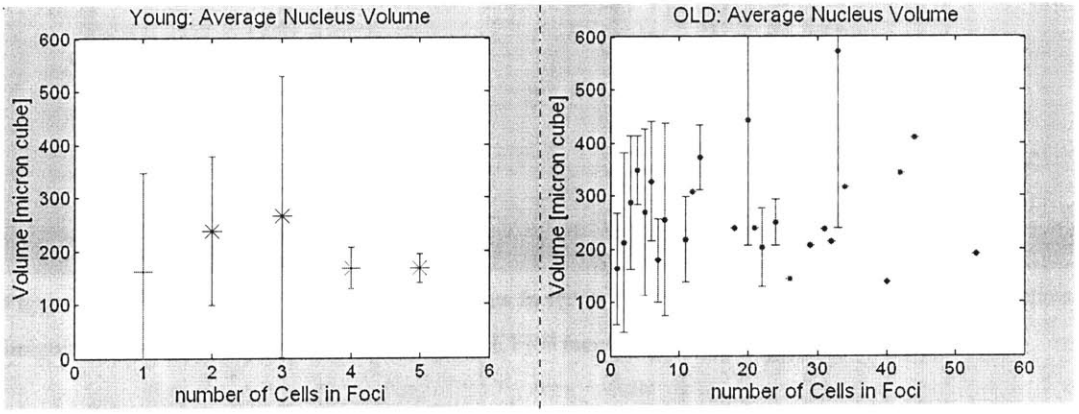

Figure 3.14. Volume changes of nucleus with age. Volume of nucleus vs number of cells in recombinant EYFP foci was plotted. Volume each nucleus at foci was averaged.

The brightness of each nucleus was measured in terms of average value of intensity per pixel and average value of intensity per nucleus. The brightness of nucleus is almost constant when it was plotted against foci as shown in figure 3.15 and 3.16. Compared to the juvenile mouse, aged mouse has twice (14±5 to 7±4 [A.U.]) and more than two times (4200 ±2872 to 1400±1433[A.U.]) brighter as shown in intensity per pixel and intensity per nucleus volume, respectively The intensity difference can be explained from either labeling difference or different permeability of labeling for aged and juvenile case.

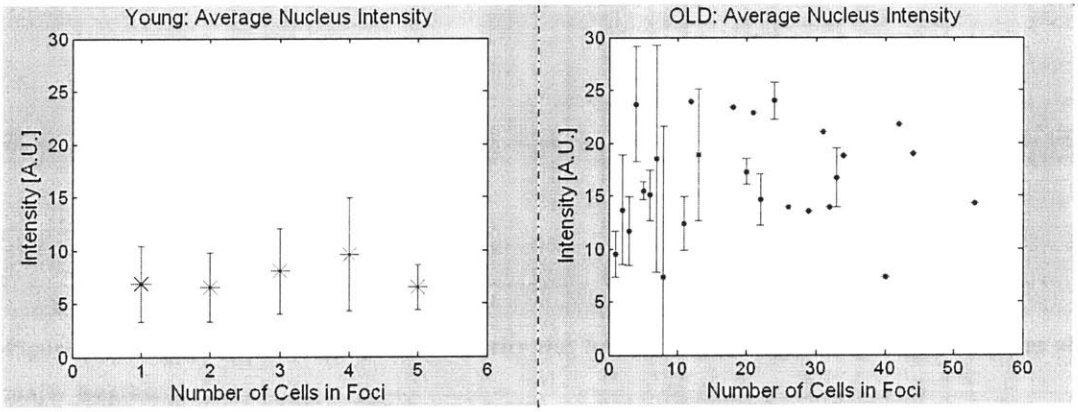

Figure 3.15. Age effect on brightness of nucleus in terms of average intensity per pixel. Nucleus brightness vs number of cells in recombinant EYFP foci was plotted.

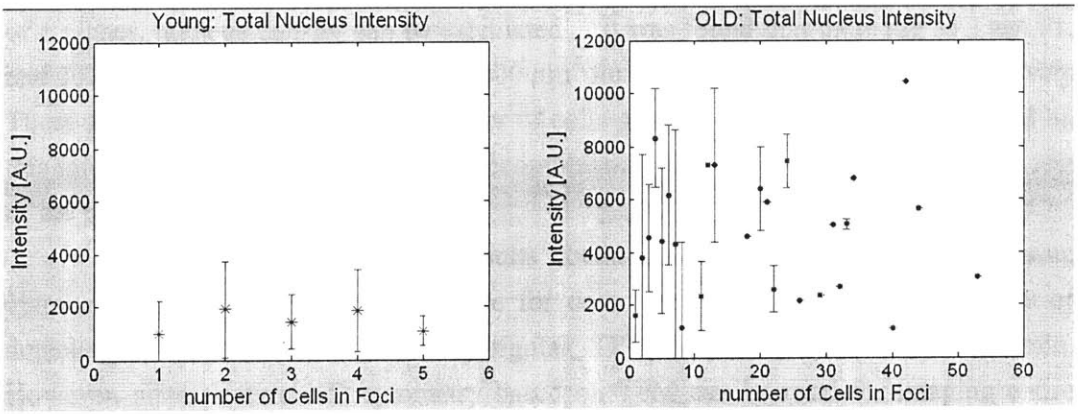

Figure 3.16. Age effect on brightness of nucleus in terms of average intensity per nucleus. Nucleus brightness vs number of cells in recombinant EYFP foci was plotted.

The lengths of principal axes were computed for each nucleus at each EYFP focus as described in algorithm development section (figure 3.17). It was expected the ellipticity from the sample preparation procedure of sandwiching the sample between

coverglass and slide. However, there was no trend found in the directions of major axes found from whole nuclei population. From the length, we can compute the ellipticity of the nucleus. Average values are found to be 0.82±0.1 and 0.84±0.1 for aged and juvenile, respectively. Data is consistent in both age types. Similar in the size and shape for nucleus in each age group indicate the possibility of the same cell type and no differentiation occurred during clonal expansion with age.

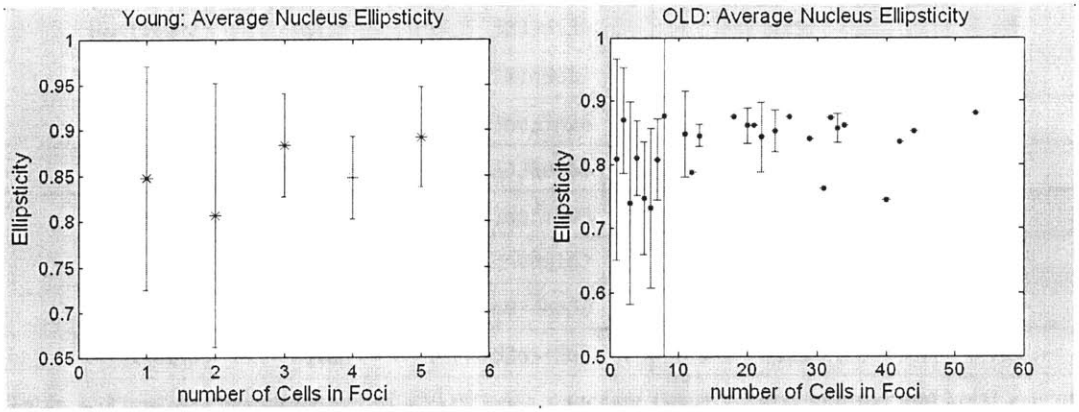

Figure 3.17. Age effect on cell shape. Ellipticity was found using the biggest and smallest values of major lengths.

We further calculate the nucleus density in the young and old mice. All of the 3-D TPM image stacks were used to find the number of cells per unit volume. It was done by counting the total number of nuclei. Using the size of both FOV and number of z planes, nucleus density can be calculated. It was found that there are 31.11±4.71, and 30.16±3.37 cells in a volume of 57600 μm^3 for juvenile and aged cases, respectively. There are no obvious changes in number of cells per unit volume with age. Based on this information, we can conclude that recombinant foci grow at the same rate as the rest of the pancreas.

We can further compare the results obtained with FC and regular TPM tissue cytometry systems in terms of the rate for detecting cells. FC has a capability of detecting over 100,000 cell/min. Regular TPM has a rate of 1800 cells/min. However, site-selective 3-D cytometry based on TPM can be used for imaging entire pancreas tissue in 6 hours assuming there are 50 recombinant foci. Total volume of the pancreas tissue was approximated by surface area found from WFM times the known spacer thickness (500 μm) (table 1). Surface area was approximated by drawing a curve along the boundary of the pancreas tissue using commercially available ImageJ commands (free hand selections + analyze/measure). Total number of cells was found for each pancreas tissue. Total number of cells were approximated by total volume

times the number of cell per unit volume. Using the information of the number of recombinant cell, and total number of cells in pancreas tissue, a frequency plot was generated (figure 3.18).

	Total volume [mm^3]	Total number of cells	Total number of Recombinant cells	Ratio ($1:10^6$ cells)
Juvenile 1	55.7	30093472	38	5
Juvenile 2	61.7	33335139	25	3
Juvenile 3	52.275	28243021	7	1
Juvenile 4	66.695	36033826	20	2
Juvenile 5	61.795	33386465	20	2
Juvenile 6	49.33	26651903	32	5
Juvenile 7	48.12	25998167	12	2
Aged 1	116	60748636	649	43
Aged 2	105	52631361	249	19

Table 1. Physical characteristics of FYDR mice pancreas tissue. Total volume and total cell of pancreas tissue of juvenile mice (n=7) and aged mice (n=2) were measured. Total number of recombinant cells were found from TPM images. Ratio of total number of recombinant cells to total number of cell was computed.

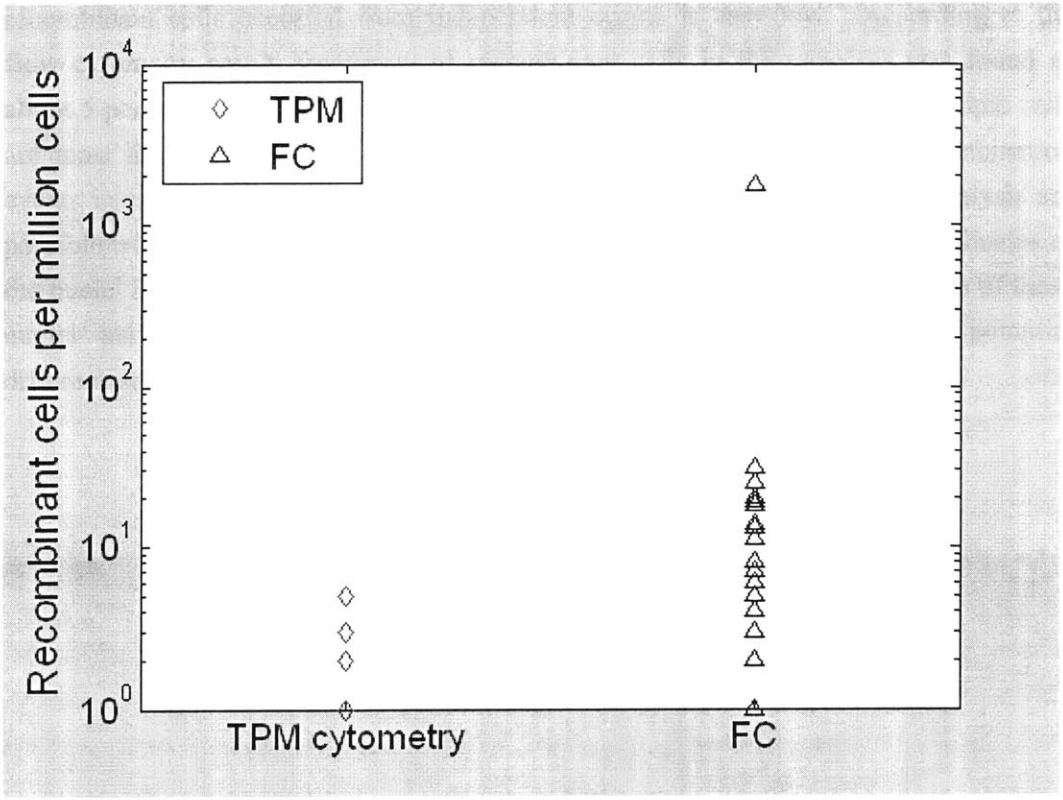

Figure 3.18. Frequency of recombinant cells in the pancreas tissue. Frequency of recombinant cells per million as determined by flow cytometry (n=49), and TPM site-selective tissue cytometry (TPM cytometry) (n=7) for juvenile.

3.1.7 Conclusion.

We have integrated one and two-photon microscopy to create a sensitive imaging system that spans four orders of magnitude. This imaging platform rapidly identifies rare fluorescent cell clusters within an entire mouse tissue at the cm scale and subsequently provides 3-D images of each fluorescent cell cluster at the micron scale. We applied these techniques to study the effect of aging on clonal expansion of fluorescent cells in the pancreas tissue of FYDR mice. This combination of mechanico-optical engineering technologies with genetically engineered FYDR mice can be applied to study the effects of genetic and environmental exposures on the risk of double strand breaks and resultant carcinogenesis. The frequency, brightness and the sizes of the both recombinant foci and nuclei inside of them were quantified with TPM images. The increase in the number of cells per recombinant focus can be explained as the result from either multiple independent recombination events occurring in neighboring cells or clonal expansion. However, the probability that two adjacent

recombinant cells occurred from independent events is very low. According to the flow cytometry result, frequency of recombinant cells in the pancreas was found as about 5 per million cells [D24]. Therefore, recombinant foci containing multiple cells are most likely the result of clonal expansion rather than independent recombination events in neighboring cells. As mentioned before, there are many other analysis are possible with the available information. For example, since the centroid coordinates of the nuclei inside of each recombinant focus are known, the spatial relationships of these nuclei may provide addition information about clonal expansion and potential differentiation processes at the recombination foci.

3.2 Multi-scale study of mouse tongue musculature

3.2.1 Introduction

The human tongue is a structurally complex muscular organ, composed of a continuum of variably aligned intrinsic and extrinsic fibers used for swallowing or speaking. From an anatomical point of view, the tongue consists of an overlapping three-dimensional network of skeletal muscle fibers and fiber bundles. A complex network of highly interwoven fibers in the tongue is responsible for producing numerous variations of shape, position, and stiffness [E1–5]. Understanding tongue structure requires a complete 3-D representation of fiber orientations present in the whole organ. The determination of principal fiber directions in structurally heterogeneous tongue tissue can aid in understanding of its mechanical function.

From the previous study, imaging the 3-D structures of the complex mammalian tongue of interwoven fiber populations were identified and characterized in bovine tongue, and mouse tongue using two types of nuclear magnetic resonance (NMR) methods, diffusion tensor imaging (DTI) [E6-8], and diffusion spectrum imaging (DSI) with tractography, [E9]. Two NMR methods use diffusion weighted MRI for signal acquisition but use different post processing methods to represent the 3-D structures. These magnetic resonance imaging techniques are based on direction specific differences in water diffusion. Water diffuses preferentially in anisotropic tissue. Muscle tissue in particular exhibits significant diffusion anisotropy in the direction of fibers, from which diffusion imaging is able to infer fiber direction. Diffusion of water in tissue depends on the location of myofibers in the myoarchitecture. The shape of myocytes are cylindrically symmetric, their elongated cellular membranes impose barriers for the diffusion of water. Thus, maximal signal attenuation occurs preferentially along the longer axis of the myofiber. By combining the signal attenuation obtained via the application of diffusion-weighting gradients in multiple directions with standard MRI image acquisition, the amount of diffusion in those directions may be measured for each voxel and then reconstructed to constitute 3-D representations of tissue myoarchitecture. Explicit measures of fiber orientation using a single second-order tensor in each voxel yield a result intermediate between the actual fiber orientations. This 3-D representation of tissue myoarchitecture was characterized in terms of its fiber orientation. However, there was a problem associated with DTI in quantifying the geometry of fiber populations where a high degree of overlap or convergence exists. In this case, the principal eigenvector of the diffusion tensor tends

to alternate among several orientations, making the determination of specific fiber orientations ambiguous.

Diffusion Spectrum Imaging (DSI) is a particular application of diffusion weighted MRI that aims to extract the complete ensemble average probability distribution function (PDF) of diffusing hydrogen atoms within any enclosed space, such as the set of myofibers within a given voxel of tissue. PDF indicates the average probability of a spin undergoing a given displacement over a given diffusion time. The PDF, which simply describes the likelihood that a particle has diffused a particular distance and direction, reflects the tissue microstructure within the voxel. Directions of greatest diffusion are expected to correspond to the orientation of the long axis of fiber-like cells. The orientational distribution function (ODF) is a transformation of the PDF from Cartesian to spherical coordinates combined with a heuristic for maximizing diffusion contrast. This produced well-defined peaks in the ODF corresponding to maximum diffusion directions. Tractography is the rule for connecting the fibers from adjacent voxels. Tractography is an intuitive visualization method that creates intervoxel connections based on angular similarity of adjacent voxels. The local maxima of each ODF are found. Both above methods result in an ODF summarizing the fiber orientation within each voxel. For generating fiber tracts, we consider that each voxel in a DSI data set has one or more local maxima, which defines one or more vectors. Constructing intervoxel connections is a function of defining similar vector directions between voxels, and is termed streamline generation. Mathematically a streamline is the solution of an ordinary differential equation. Since there can be more than one local maxima per voxel, we have employed a method termed generalized streamline tractography which adds a constraint that a certain angular threshold must be met for intervoxel association. The current study employs a 35 degree angular threshold to generate intervoxel tracts. It should be emphasized that the tracts so constructed do not represent actual anatomical entities, such as fiber bundles or fascicles, but indicate a set of macroscopically scaled diffusion maxima corresponding to a set of similarly aligned muscle fiber populations.

Using DSI in association with tractography method, 3-D structures of the complex mammalian tongue of interwoven fiber populations were identified and characterized in bovine and mouse tongue accurately. However, since the smallest voxel size that can be achieved is about 500 micron cube even with high power of MRI in the order of 10 Tesla, there is no physiological correlation of these fibers with cellular and extracellular matrix architecture of the tongue. This issue can be resolved by developing a new method combining both DSI and TPM. In this study, we have used

the combination of DSI with tractography and TPM techniques to interrogate the microstructure of the core fibers of the mammalian tongue, and have developed an analytic framework that conceives of three-dimensional microstructure on the basis of both its local diffusivity and its explicit micro-anatomical patterns.

3.2.2. Data & initial analysis

The purpose of this study is to describe the muscle architecture of the mouse tongue using two complimentary imaging modalities. TPM is an appropriate technology with good depth penetration and sub-cellular resolution. It is important to note that TPM allow multi-scale imaging based on tissue endogenous signals. The TPM imaging will be based on second harmonic signal of collagen fibers and muscle sacromere in the tongue. This endogenous signal provides the requisite structural information and allows the visualization of individual myocyte.

TPM and DSI were performed on an excised mouse tongues. The tissue specimens for three-dimensional microscopy were either viewed as fresh tissue without fixation for finding optimized imaging condition or viewed after fixation and embedding in paraffin. Figure 3.19 shows 2-D TPM image of mouse tongue and a 3-D representation of a stack of these 2-D images. Optimized imaging condition was found using regular TPM where specimen were excited by 780nm excitation light with 200mW power using a 40 X oil immersion 1.3 NA objective. The muscle fiber with its nucleus is clearly shown in this TPM image. Two-photon imaging allows us to image 140 microns deep into tissue volumes with submicron resolution.

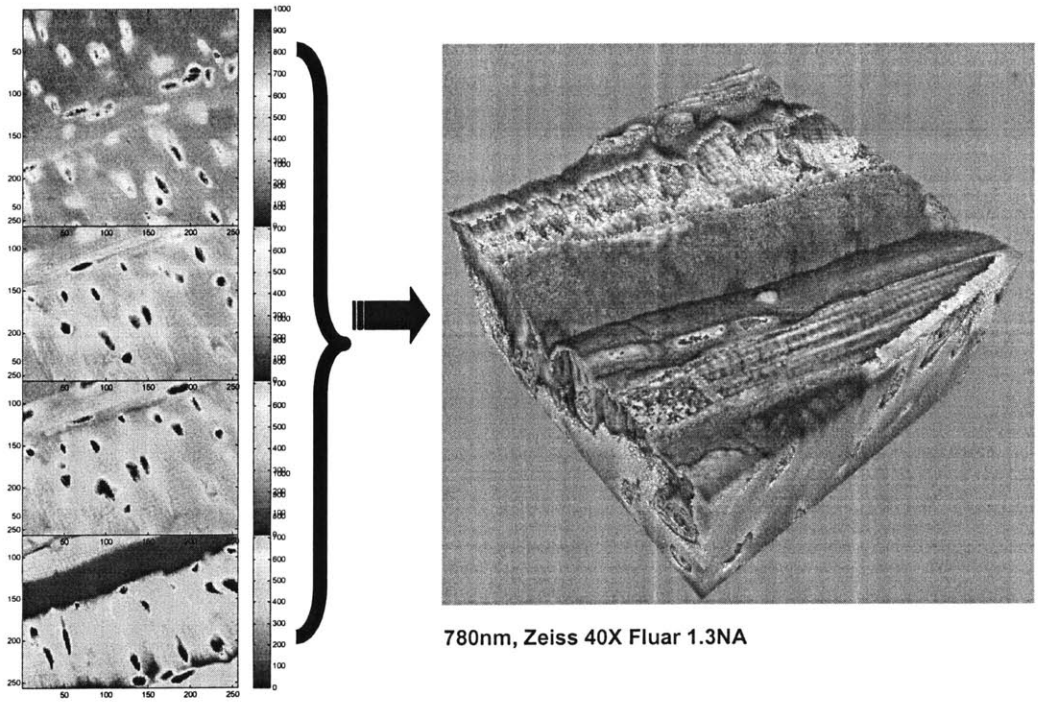

Figure 3.19: TPM of mouse tongue in 2-D and 3-D from stacking 2-D images. Images (left) were taken at 780nm with 140 micron deep with 1 micron incremental step. FOV is 120 by 120 micron. By stacking 4 volumes, 480 by 480 by 140 micron volume image (right) was generated. One of the main strengths of TPM is its ability to image thick tissues specimens. This gives us the ability to perform image cytometry in thick 3-D samples such as tissues. Above is a composite image of an *ex vivo* mouse tongue sample which has been imaged down to a depth of 140 microns. Thus it is possible to perform image cytometry on cells while they are still in their intact state, preserving many of their biochemical and mechanical inputs, and most importantly their native 3-D morphology and its relation to the 3-D architecture of the tissue. This provides a wealth of information about tissue biophysics and biology on macroscopic samples that has not been available. before.

After finding the optimized imaging condition of mouse tongue with TPM, the 3-D tissue cytometry system was calibrated as discussed in the Technology section (chapter 2.1). We further optimized imaging condition in terms of power level so that the high speed TPM will generate as good image quality as the regular TPM. Figure 3.19 shows the overlaps in TPM images along all three axes. The FOV of the 3-D tissue cytometry with combination of 40X objective and a high sensitivity PMT is 200 by 150 micron. The penetration depth for excitation is found around 80 micron.

These overlaps were done by allowing 30 microns in x and y direction and 20 microns for z direction. Figure 3.20 shows the 3-D representation of a fast scan image. The dimension is 640 by 480 by 140 micron. Through TPM imaging, we were able to determine muscle fiber structures in 3-D. As shown in figure 3.20, the fibers in the lingual core region were not, in fact, aligned as interwoven individual fibers, but rather were organized into fiber bundle sheets.

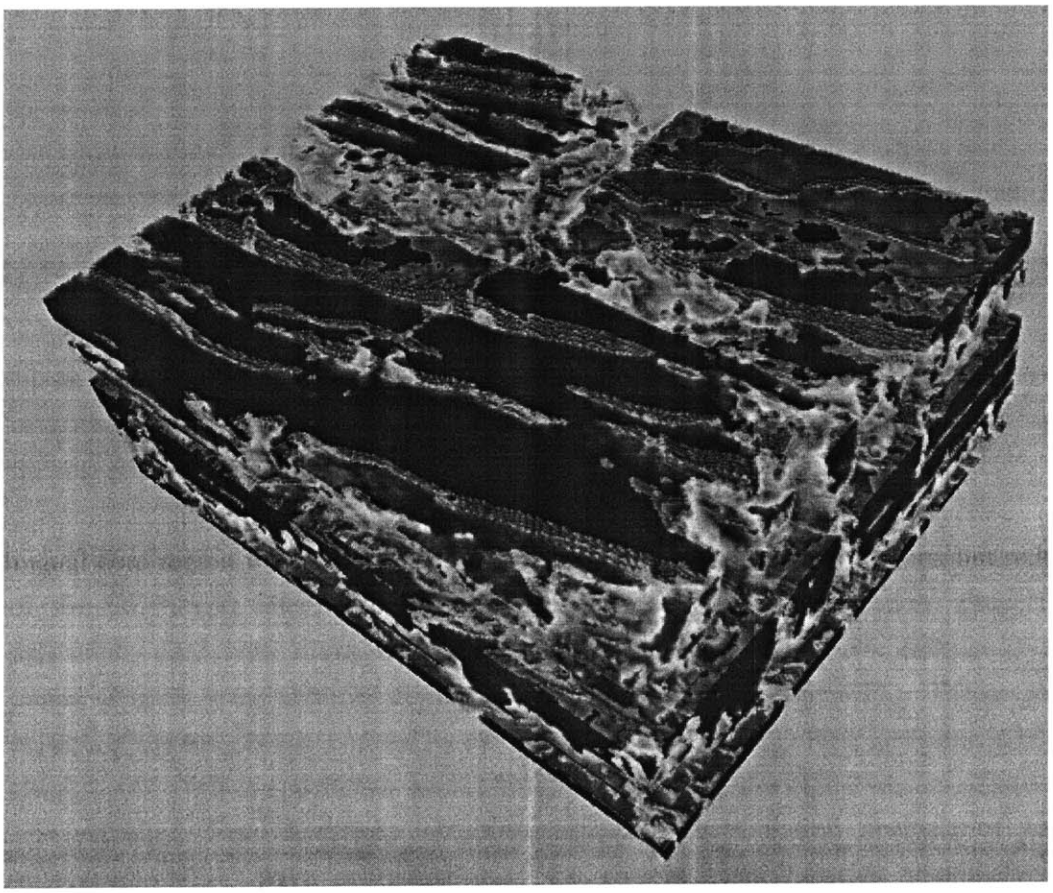

Figure 3.20: Fast scan image of mouse tongue reconstructed in 3-D. Above is a composite image of an *ex vivo* mouse tongue tissue sample. TPM images were taken at 780nm with 80 micron deep with 1 micron incremental step in z axis. FOV of each image is 200 by 150 micron. For the current application, the sectioning depth was 60 μm and the imaging depth was 80 μm allowing a 20 μm axial registration overlap. There are 30 μm radial registration overlap. By stacking 8 volumes, 640 by 480 by 140 micron 3-D volume was generated.

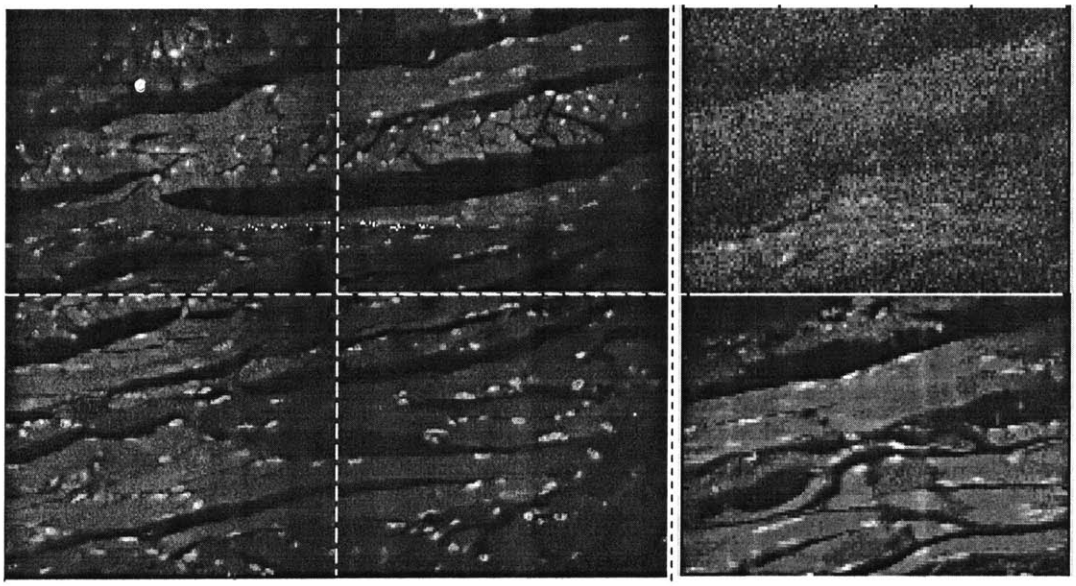

(a)Overlap in X-Y (b)Overlap in Z

Figure 3.21: Raw images of fast scan images showing overlaps in X-Y-Z directions. Series of imaging of 200 micron by 150 micron by 80 micron volumes were done. There were four adjacent 2-D images (a) in x and y direction showing about 30 micron overlap in each direction. The entire images have about 20 micron overlap in z direction, which was shown in dim and bright imaging of the same physical plane (b).

We studied excised tongues in order to relate the intravoxel (diffusion maxima of the ODF) and intervoxel (tract distribution, length, and orientation) properties defined by DSI with mean fiber orientation defined by TPM. Six female 357BL mouse tongues were obtained from the Engelward Laboratory at MIT. The anterior portion of the tongue was excised by extending the tongue and cutting just prior to basal attachment. Whole specimens were refrigerated and studied within 24 hours of harvest. The principal fiber directions obtained through autocorrelation analysis of each microscopic FOV were compared with the co-registered diffusion maxima/voxel obtained by DSI. For DSI imaging, whole mouse tongue was scanned with a Magnex Scientific 9.4T 21cm diameter horizontal bore magnet with Magnex gradient coil set capable of 20 G/cm (b-value of 7000 s/mm and net isotropic voxel dimension of 150 μm). For 3-D tissue cytometry with TPM, whole specimens (n=2) were imaged using a multi-photon high speed imaging system with a high speed robotic sample stage and an automated microtome.

Image processing was achieved via a 3-D autocorrelation algorithm. The autocorrelation of an image volume (or subvolume) is computed in order to find average

repetitive structures within the image, such as homogeneously aligned fibers. The principal patterns in the microscopy data were revealed by radially integrating from the center of the autocorrelation data, thereby creating an ODF similar to that created for each voxel using diffusion spectrum MRI. A single value was recorded for the bidirectional radial integration for each of 181 vectors equally spaced on the surface of a half-sphere over a distance of 12.5um with a step size of 0.05 um; thus compressing each 9.2 megabyte image volume file into 181 numbers. In this manner, mesoscale tractography was performed both from the exact fiber orientation obtained by microscopy and that obtained by DSI of the whole tissue, thus providing a spatial linkage at the mesoscale (figure 3.22).

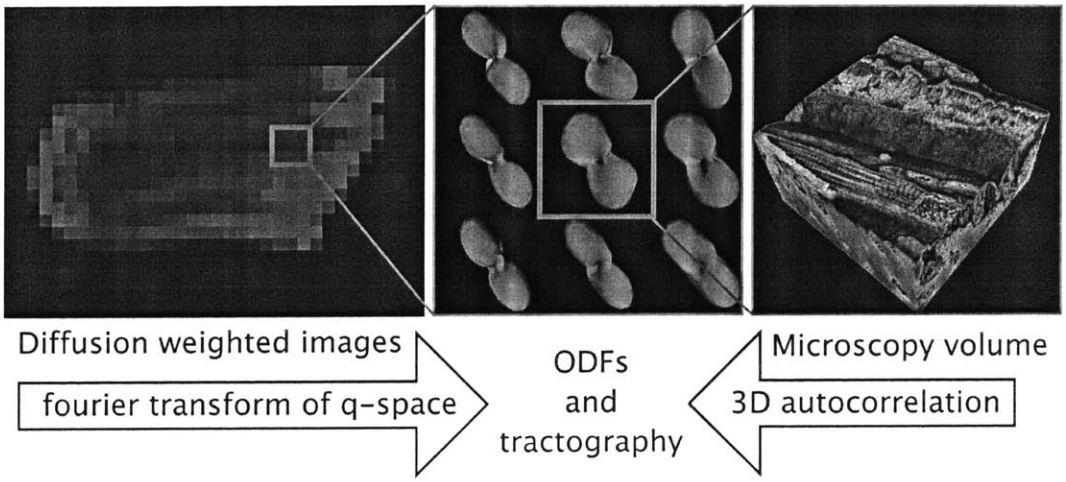

Figure 3.22: Mesoscale tractography: Template for contractility at the interface of microscopic and macroscopic scales. To quantitatively relate myofiber architecture at the resolution of the cell and the tissue, voxel specific ODFs and intervoxel tracts were generated. A set of diffusion weighted images leads to the extraction of subvoxel information about fiber alignment in the form of an ODF field, whereas an ODF field can also be generated directly via the 3-D autocorrelation function of the microscopic image.

To aid anatomical study, DSI with tractography showing the 3-D structural relationships involving intrinsic and extrinsic myofiber populations of the mouse tongue can be useful. We depict in Figure 3.23 the normal myoarchitecture of the excised anterior murine tongue, demonstrating in particular the predicted relationship among the intrinsic fiber populations and novel observations regarding the configuration of the transversus fibers and the insertion points for the extrinsic fiber groups. Of the extrinsic muscles, the genioglossus (gg) is the most clear, entering from below and

extending along the sagittal plane into the lingual core. The laterally located green fibers wrapping superiorly as they approach the anterior tip could either be the ends of an inferiorly positioned styloglossus or perhaps the mouse equivalent of the chondroglossus.

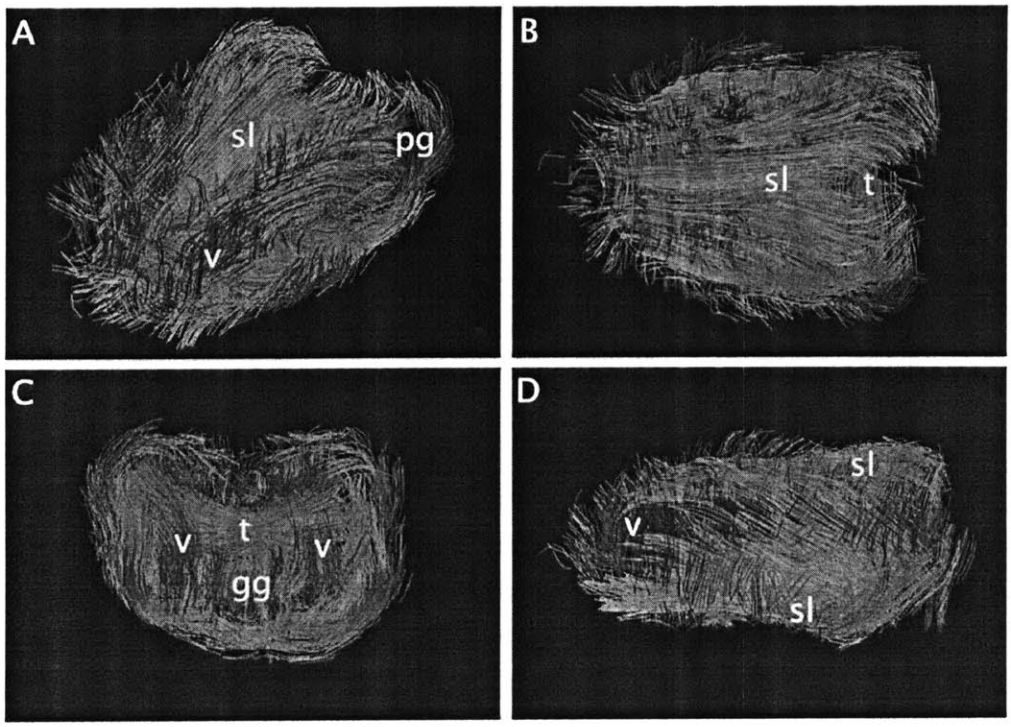

Figure 3.23. DSI of murine tongue. Demonstrated is a full diffusion spectrum imaging with tractography data set obtained at 9.4T (voxel size 150 μm) of the anterior 357BL mouse tongue from the (A) oblique, (B) coronal (superior), (C) axial (posterior),and (D) sagittal perspectives. The green superior longitudinalis (sl) and inferior longitudinalis (il) run along the dorsal and ventral exterior surfaces. The transversus (t) and verticalis (v) are not perfectly horizontal and vertical but rather form an interesting concave box like structure, becoming parallel with each other at the corners. Extrinsic fibers identified include the genioglossus (gg) and palatoglossus (pg)

We show in Figure 3.24 a direct comparison of tractography renderings from DSI (sagittal orientation) and from two photon microscopy for the mouse anterior tongue. Observe the high degree of concordance in terms of the distribution of myofiber tracts, confirming the significance of mesoscale constructs in relating fiber orientation and mechanics. The ability to identify the cells comprising a region of mesoscale architecture is significant since it provides a direct anatomical validation for DSI tractography and provides a method for relating structural data at the cellular level

with morphogenesis at the scale of the tissue.

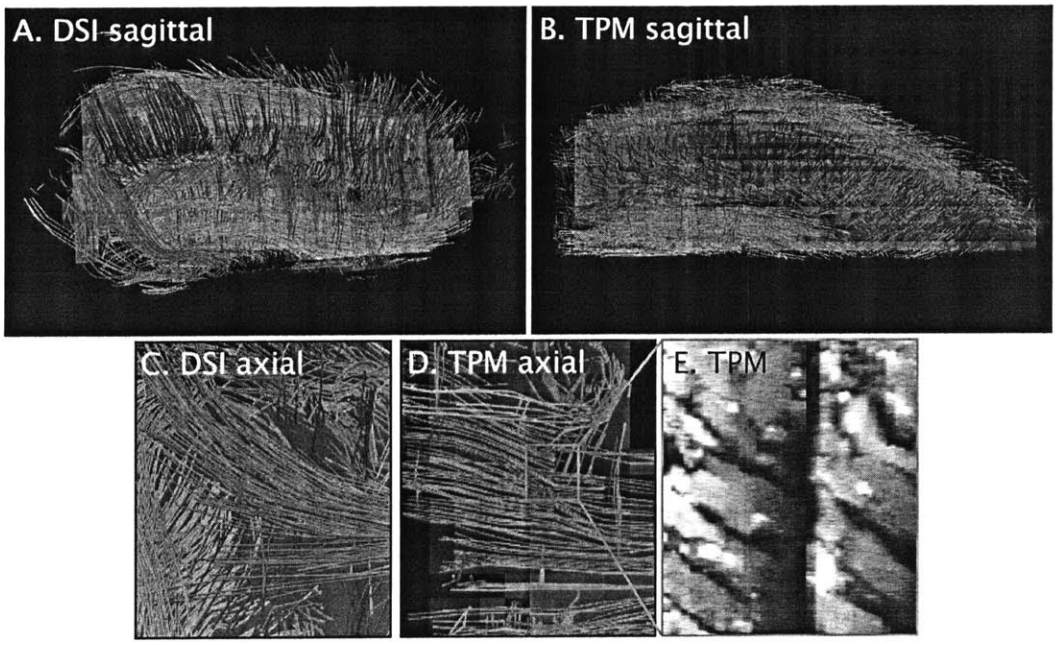

Figure 3.24: Tractography of mouse tongue myoarchitecture obtained by DSI (A) and TPM (B). The most lateral slices of the DSI tractography have been removed to match the TPM. Higher resolution DSI tractography image (C) of an axial slice emphasizing the transverse oriented fibers. Similar resolution TPM tractography image is displayed (D) accompanied an TPM image in (E) of a region of myocytes corresponding to the indicated myofiber tracts shown in (D). These results confirm the capacity of these imaging methods to derive intermediate scale myofiber tracts both from the local diffusion maxima displayed by DSI and directly from 3-D microscopy data.

3.2.3 Conclusions

It is generally believed that the structural basis of the tongue's mechanical virtuosity is its extensively interwoven myoarchitecture, whereby the constituting myofibers are simultaneously aligned along multiple spatial axes at the microscopic scale. The precise determination of the tongue's myoarchitecture and the relationship of its myoarchitecture to mechanical function are questions that have long challenged students of biological mechanics. Diffusion weighted magnetic resonance imaging (DW-MRI) reveals whole tissue architecture. Diffusion weighted imaging is sensitized to the amount of self diffusion in a particular direction by sustaining and reversing a gradient in that direction. Use of DSI with tractography distinguishes between regions consisting of crossing and noncrossing fiber populations, and explicitly allows angular

quantification of crossing fiber populations. The application of this technique *in vivo* should allow clinicians to derive measurable assays of normal and pathological myoarchitecture in anatomically complex tissues without the need for invasive tissue sampling or dissection. However, fiber tracts found from DSI with tractography is from preferential water diffusion paths in the tissue and has been shown to be correlated with physiological motion of the tongue. On the other hand, fiber tracts found from TPM with imaging analysis is from the second harmonic signals of collagen. We demonstrated the mesoscale architectural linkage between the microscopic and tissue scales validating the hypothesis that the fiber tracks observed from DSI is consistent with the distribution of myocyte fibers in the tissue.

Future work will be directed to defining the mechanical significance of these interwoven fiber populations in carrying physiological tissue deformations. Identifying complex myofiber populations can be used to relating architectural structure with mechanical function in muscular tissues [E10-12].

Chapter 4

Conclusions

The technology of 3-D tissue cytometry has been successfully developed to optimize specimen throughput by combining high speed TPM, automated x-y specimen stage, and precision specimen sectioning mechanism. In our laboratory, we have developed a novel method of 3-D tissue cytometry based on TPM allowing the characterization of cell-cell, cell-tissue interaction to be quantified in 3-D tissue. The goal of my thesis was to develop new technologies for optimizing the performance of existing 3-D tissue cytometry. There are several ways to achieve higher specimen throughput by improving the data acquisition time. An easy way to reduce this is to increase the size of the imaging FOV so that the specimen has to be repositioned less often, or to use higher speed x-y specimen stage so that the point to point specimen translation time decreases. All these simple changes to improve the data acquisition time must also maintain the image SNR. For general approach to increase the specimen throughput or decrease data acquisition time, we are interested in achieving greater penetration depth. For the special case of studying rare events in tissues, we are interested in developing new technique to decrease the data acquisition time.

We have developed and implemented two versions of tissue cytometry. 3-D tissue cytometry and 3-D site selective tissue cytometry. 3-D tissue cytometry with fast scan method based on polygonal mirror can achieve an imaging speed of 10 frames/s. This system is based on single-focus scanning and signal collection with large, non-spatial resolved detectors such as PMTs. We have integrated one- and two-photon microscopy to create a sensitive imaging system that can image a tissue specimen that spans four orders of magnitude in size scale. This 3-D site selective tissue cytometry rapidly identifies rare regions of interest within an entire specimen (at the cm scale) and subsequently provides 3-D images of these regions (at the micron scale) with high resolution. Using this WFM along with TPM, we demonstrated that this system has performance of tissue imaging almost comparable with conventional TPM in terms of imaging depth but can image at significantly higher speed. Limitation in imaging depth of 3-D site selective tissue cytometry was identified as a main hurdle for whole organ study. While optical clearing has shown promises for fresh tissue, this approach did not significantly improve imaging depth for fixed specimen. For 3-D cytometry specimen, fresh tissue is too soft for mechanical sectioning and we decided to investigate the effect of optical clearing on frozen tissues. Our study of optical

clearing effect on frozen mouse heart and brain tissues indicates that this is a promising approach and optical clearing of frozen and fresh tissue show similar imaging depth improvement. We further quantify the degree of tissue volume decrease with optical clearing agent applied on mouse pancreas tissue. Ongoing studies will be necessary to determine the effects of the sub zero temperature on the optical components.

The utility of these 3-D tissue cytometry were demonstrated by two biomedical studies. First, the high throughput 3-D site selective tissue cytometry was used in the FYDR mouse project. This study was the first quantitative measurement of clonal expansion in FYDR mouse pancreas. We demonstrated the power of using complementary imaging modalities to identify EYFP recombinant foci by WFM and to image these sites at high resolution to obtain cellular morphological information by TPM. Previous study using combination of FC and WFM had difficulty in the quantification of clonal expansion in the foci due to the lack of 3-D resolution of WFM. We have investigated the effect of aging on HR by comparing foci size, brightness and cell morphology. Second, we demonstrated the use of the two-photon 3-D tissue cytometry in the study of musculature of mouse tongue. 3-D imaging of specimen on the size scale of cubic centimeters allow the study of whole organ physiology with cellular and molecular resolution. The ability to image tissue structures over four decades in length scale allows a correlative study with magnetic resonance imaging and allows a better interpretation of DSI structures in terms of molecular and cellular tissue features. Specifically, we found that the fiber track distribution observed with DSI has good correlation with the underlying muscle fiber bundle distribution.

Bibliography

A1. Denk, W., J.H. Strickler, and W.W. Webb, Two-photon laser scanning fluorescence microscopy. Science, 1990. 248(4951): p. 73-6.

A2. Denk, W. (1994). "2-photon scanning photochemical microscopy." PNAS 91(14): 66296633.

A3. Corcuff, P., Bertrand, C. and Leveque, J. L. (1993). Morphometry of human epidermis *in vivo* by real-time confocal microscopy, Arch. Dermatol. Res. 285: 475-481.

A4. Rajadhyaksha, M., Grossman, M., Estrowitz, D. and Webb, R. H. (1995). In-vivo confocal scanning laser microscopy of human kin - melanin provides strong contrast, Journal of investigative dermatology 104(6): 946-952.

A5. Sako, Y., Sekihata, A., Yanagisawa, Y., Yamamoto, M., Shimada, Y., Ozaki, K. and Kusumi, A. (1997). "Comparison of two-photon excitation laser scanning microscopy with UV-confocal laser scanning microscopy in three-dimensional calcium imaging using the fluorescence indicator Indo-1." Journal of microscopy-oxford 185(Part 1): 9-20.

A6. Steiner, G. E., Ecker, R. C., Kramer, G., Stockenhuber, F. and Marberger, M. J. (2000). Automated data acquisition by confocal laser scanning microscopy and image analysis of triple stained immunofluorescent leukocytes in tissue, Journal of Immunological Methods 237: 39-50.

A7. Pustavalov, V. K. (1995). "Initiation of explosive boiling and optical breakdown as a result of the action of laser pulses on melanosome in pigmented biotissues." Kvantovaya elektronika 22(11): 1091-1095.

A8. Buist, A. H., Muller, M., Squier, J. and Brakenhoff, G. J. (1998). Real time two-photon absorption microscopy using multi point excitation, J. Micros.-Oxf. 192: 217-226.

A9. Beaurepaire, E. and J. Mertz (2002). "Epifluorescence collection in two-photon microscopy." App. Opt. 41(25): 5376-5382.

A10. Masters BR, S.P., Gratton E, Multiphoton excitation fluorescence microscopy and spectroscopy of *in vivo* human skin. Biophysical Journal, 1997. 72: p. 2405-2412.

A11. So, P.TC., *et al.*, Two-Photon Excitation Fluorescence Microscopy. Annu Rev Biomed Eng, 2000. 2: p. 399-429.

A12. Givan, A.L., Principles of flow cytometry: An overview, in Methods in Cell Biology, Vol 63. 2001, ACADEMIC PRESS INC: San Diego. p. 19-50.

A13. Melamed, M.R., A brief history of flow cytometry and sorting, in Methods in Cell

Biology, Vol 63. 2001, ACADEMIC PRESS INC: San Diego. p. 3-17.
A14. Kamentsky, L.A. and M.R. Melamed, Spectrophotometric cell sorter. Science, 1967. 156(780): p. 1364-5.
A15. Van Dilla, M.A., *et al.*, Cell microfluorometry: a method for rapid fluorescence measurement. Science, 1969. 163(872): p. 1213-4.
A16. Rieseberg, M., Kasper, C., Reardon, K. F. and Scheper, T. (2001). Flow cytometry in biotechnology, Appl. Microbiol. Biotechnol. 56: 350-360.
A17. Rieseberg, M., *et al.*, Flow cytometry in biotechnology. Applied Microbiology and Biotechnology, 2001. 56(3-4): p. 350-360.
A18. Darzynkiewicz, Z., *et al.*, Laser-scanning cytometry: A new instrumentation with many applications. Experimental Cell Research, 1999. 249(1): p. 1-12.
A19. Kamentsky, L.A., *et al.*, Slide-based laser scanning cytometry. Acta Cytol, 1997. 41(1): p. 123-43.
A20. Kamentsky, L.A. and L.D. Kamentsky, Microscope-based multiparameter laser scanning cytometry yielding data comparable to flow cytometry data. Cytometry, 1991. 12(5): p. 381-7.
A21. Ecker, R. C. and Steiner, G. E. (2004). Microscopy-based multicolor tissue cytometry at the single-cell level, Cytometry Part A 59A: 182-190.
A22. Kamentsky, L.A., Laser scanning cytometry, in Methods in Cell Biology, Vol 63. 2001, ACADEMIC PRESS INC: San Diego. p. 51-87.
A23. Gorczyca, W., Z. Darzynkiewicz, and M.R. Melamed, Laser scanning cytometry in pathology of solid tumors - A review. Acta Cytologica, 1997. 41(1): p. 98-108.
A24. Hendricks, J.B., Quantitative histology by laser scanning cytometry. Journal of Histotechnology, 2001. 24(1): p. 59-62.
A25. Tarnok, A. and Gerstner, A. O. H. (2002). Clinical applications of laser scanning cytometry, Cytometry 50: 133-143.
A26. Gerstner, A. O. H., Trumpfheller, C., Racz, P., Osmancik, P., Tenner-Racz, K. and Tarnok, A. (2004). Quantitative histology by multicolor slide-based cytometry, Cytometry Part A 59A: 210-219.
A27. Powers, M.J., *et al.*, Functional behavior of primary rat liver cells in a three-dimensional perfused microarray bioreactor. Tissue Engineering, 2002. 8(3): p. 499-513.
A28. Liotta, L.A. and E.C. Kohn, The microenvironment of the tumour-host interface. Nature, 2001. 411(6835): p. 375-379.
A29. Knezevic, V., *et al.*, Proteomic profiling of the cancer microenvironment by antibody arrays. Proteomics, 2001. 1(10): p. 1271-1278.
A30. Gohongi, T., *et al.*, Tumor-host interactions in the gallbladder suppress distal

angiogenesis and tumor growth: involvement of transforming growth factor beta1. Nat Med, 1999. 5(10): p. 1203-8.

A31. EmmertBuck, M.R., *et al.*, Laser capture microdissection. Science, 1996. 274(5289): p. 998-1001.

A32. Bonner, R.F., *et al.*, Cell sampling - Laser capture microdissection: Molecular analysis of tissue. Science, 1997. 278(5342): p. 1481-

A33. Guild, J.B. and W.W. Webb, Line scanning microscopy with two-photon fluorescence excitation. Biophys J, 1995. 68: p. 290a.

A34. Fan, G.Y., *et al.*, Video-rate scanning two-photon excitation fluorescence microscopy and ratio imaging with cameleons. Biophys. J., 1999. 76(5): p. 2412-20.

A35. Kim, K.H., C. Buehler, and P.T.C. So, High-speed, two-photon scanning microscope. Appl. Opt., 1999. 38(28): p. 6004-9.

A36. Bewersdorf, J., R. Pick, and S.W. Hell, Mulitfocal multiphoton microscopy. Opt. Lett., 1998. 23: p. 655-657.

A37 Buist, A. H., Muller, M., Squier, J. and Brakenhoff, G. J. (1998). "Real time two-photon absorption microscopy using multi point excitation." J. Micros.-Oxf. 192: 217-226.

A38. Nielsen, T., Frick, M., Hellweg, D. and Andresen, P. (2001). High efficiency beam splitter for multifocal multiphoton microscopy, Journal of microscopy-oxford 201: 368-376.

A39. Buehler, C., Kim, K. H., Greuter, U., Schlumpf, N. and So, P. T. C. (2005). Single-photon counting multicolor multiphoton fluorescence microscope, Journal of fluorescence 15(1): 41

A40. Davies, J. A. (2001). Extracellular matrix, Encyclopedia of life sciences.

A41. Konig, K., Becker, T. W., Fischer, P., Riemann, I. and Halbhuber, K. J. (1999). "Pulse-length dependence of cellular response to intense near-infrared laser pulses in multiphoton microscopes." Optics letters 24(2): 113-115.

A42. Jain, R. K. (1999). Understanding barriers to drug delivery: High resolution *in vivo* imaging is key, Clin. Cancer. Res. 5: 1605-1606.

A43. Denk, W., Delaney, K. R., Gelperin, A., Kleinfeld, D., Strowbridge, B. W., Tank, D. W. and Yuste, R. (1994). "Anatomical and functional imaging of neurons using 2-photon laser-scanning microscopy." Journal of neuroscience methods 54(2): 151-162.

A44. Fan, G. Y., Fujisaki, H., Miyawaki, A., Tsay, R.-K., Tsien, R. Y. and Ellisman, M. H. (1999). "Video-Rate Scanning Two-Photon Excitation Fluorescence Microscopy and Ratio Imaging with Cameleons." Biophy. J. 78: 2412-2420.

A45. Koester, H. J., Baur, D., Uhl, R. and Hell, S. W. (1999). "Ca2+ fluorescence

imaging with pico- and femtosecond two-photon excitation: Signal and photodamage." Biophysical journal 77(4): 2226-2236.

A46. Konig, K., So, P. T. C., Mantulin, W. W., Tromberg, B. J. and Gratton, E. (1996). "Twophoton excited lifetime imaging of autofluorescence in cells during UVA and NIR photostress." Journal of microscopy-oxford 183: 197-204.

A47. Masters, B. R., So, P. T. C., Buehler, C., Barry, N., Sutin, J. D., Mantulin, W. W. and Gratton, E. (2004). "Mitigating thermal mechanical damage potential during two-photon dermal imaging." Journal of biomedical optics 9(6): 1265-1270.

A48. Masters, B. R., So, P. T. C. and Gratton, E. (1997). "Multiphoton excitation fluorescence microscopy and spectroscopy of *in vivo* human skin." Biophys. J. 72(6): 2405-2412.

A49. Piston, D. W., Masters, B. R. and Webb, W. W. (1995). "3-Dimensionally resolved NAD(P)H cellular metabolic redox imaging of the in-situ cornea with 2-photon excitation laser-scanning microscopy." Journal of microscopy-oxford 178: 20-27 Part 1.

A50. Squirrell, J. M., Wokosin, D. L., White, J. G. and Bavister, B. D. (1999). "Long-term two-photon fluorescence imaging of mammalian embryos without compromising viability." Nature Biotech. 17(8): 763-767.

A51. Masters, B. R., So, P. T. C. and Gratton, E. (1997). Multiphoton excitation fluorescence microscopy and spectroscopy of *in vivo* human skin, Biophys. J. 72(6): 2405-2412.

A52. Masters, B. R., So, P. T. C. and Gratton, E. (1998). Optical biopsy of *in vivo* human skin: Multi-photon excitation microscopy, LASERS IN MEDICAL SCIENCE 13(3): 196-203.

A53. Padera, T. P., Stoll, B. R., So, P. T. C. and Jain, R. K. (2002). Conventional and High-Speed Intravital Multiphoton Laser Scanning Microscopy of Microvasculature, Lymphatics, and Leukocyte.Endothelial Interactions, Molecular Imaging 1: 9-15.

A54. Squirrell, J. M., Wokosin, D. L., White, J. G. and Bavister, B. D. (1999). Long-term two-photon fluorescence imaging of mammalian embryos without compromising viability, Nature Biotech. 17(8): 763-767.

A55. Yu, B., Dong, C.-Y., So, P. T. C., Blankschtein, D. and Langer, R. (2001). In Vitro Visualization and Quantification of Oleic Acid Induced Changes in Transdermal Transport Using Two-Photon Fluorescence Microscopy, J. Invest. Dermatol. 117: 16-25.

A56. Yu, B., Kim, K. H., So, P. T. C., Blankschtein, D. and Langer, R. (2002). Topographic Heterogeneity in Transdermal Transport Revealed by High-Speed Two-Photon Microscopy: Determination of Representative Skin Sample Sizes, J. Invest. Dermatol. 118:1085-1088.

A57. Yu, B., Kim, K. H., So, P. T. C., Blankschtein, D. and Langer, R. (2003). Evaluation of Fluorescent Probe Surface Intensities as an Indicator of Transdermal Permeant Distributions Using Wide-Area Two-Photon Fluorescence Microscopy, Journal of pharmaceutical sciences 92(12): 2354-2365.

A58. Yu, B., Kim, K. H., So, P. T. C., Blankschtein, D. and Langer, R. (2003). Visualization of Oleic Acid-induced Transdermal Diffusion Pathways Using Two-photon Fluorescence Microscopy, J. Invest. Dermatol. 120: 448-455.

A59. Fan, G. Y., H. Fujisaki, *et al.* (1999). "Video-Rate Scanning Two-Photon Excitation Fluorescence Microscopy and Ratio Imaging with Cameleons." Biophy. J. 78: 2412-2420.

B1. Dhenain, M., S.W. Ruffins, and R.E. Jacobs, Three-Dimensional Digital Mouse Atlas Using High-Resolution MRI. Developmental Biology, 2001. 232(2): p. 458-470.

B2. Huang, D., *et al.*, Optical coherence tomography. Science, 1991. 254(5035): p. 1178-81.

B3. Sharpe, J., *et al.*, Optical projection tomography as a tool for 3-D microscopy and gene expression studies. Science, 2002. 296(5567): p. 541-545.

B4. Ewald, A.J., *et al.*, Surface imaging microscopy, an automated method for visualizing whole embryo samples in three dimensions at high resolution. Developmental Dynamics, 2002. 225(3): p. 369-375.

B5. Hoffman, R.M., Green fluorescent protein imaging of tumour growth, metastasis, and angiogenesis in mouse models. Lancet Oncology, 2002. 3(9): p. 546-556.

B6. Streicher, J. and G.B. Muller, 3-D modelling of gene expression patterns. Trends in Biotechnology, 2001. 19(4): p. 145-148.

B7. Timothy Ragan, Jeremy D. Sylvan, Ki Hean Kim, Hayden Huang, Karsten Bahlmann, Richard T. Lee, and Peter T. C. So, High-resolution whole organ imaging using two-photon tissue cytometry J. Biomed. Opt. 12, 014015 (2007)

C31. Ramanujan VK, Zhang JH, Biener E, Herman B., Multiphoton fluorescence lifetime contrast in deep tissue imaging: prospects in redox imaging and disease diagnosis J Biomed Opt. 2005 Sep-Oct;10(5):051407.

C32. He, G.S., Markowicz, P.P., Lin, T-C. and Prasad, P.N. (2002) Observation of stimulated emission by direct three-photon excitation. Nature 415, 767-770

C33. L. Sherman, J.Y. Ye, O. Albert, T. B. Norris, Adaptive correction of depth-induced abberations in multiphoton scanning microscopy using a deformable mirror, J. Microsc. 206(1), pp65-71, 2002.

C34. P. N. Marsh, D. Burns, and J.M. Girkin, Practical implementation of adaptive optics in multiphoton microscopy, Optics Express 11, pp. 1123-1130, 2003

C35. M. J. Booth, M. A. A. Neil, T. Wilson, Adaptive abberation correction in confocal microscope, Proc. Nat. Acad. Sci. 99(9), pp. 5788-5792, 2002
C36. Williams C, Ponten F, Moberg C, Soderkvist P, Uhlen M, Ponten J, Sitbon G, Lundeberg J, A high frequency of sequence alterations is due to formalin fixation of archival specimens, Am J Pathol. 2000 Apr;156(4):1478.
C41. Valery V Tuchin, Optical clearing of tissues and blood using the immersion method, J. Phys. D: Appl. Phys. vol 38 P. 2497-2518, 2005
C42. Plotnikov S, Juneja V, Isaacson AB, Mohler WA, Campagnola PJ. Optical clearing for improved ontrast in second harmonic generation imaging of skeletal muscle. Biophys J. 2006 Jan 1;90(1):328-39.
C43. Barry Fuller (Editor), Nick Lane (Editor), Erica E. Benson, Life in the frozen state, CRC, 2004.
C44. http://en.wikipedia.org/wiki/Vitrification
C45.PolgeC, Smith AU, Parkes AS. Revival of spermatozoa after vitrification and dehydration at low temperatures. Nature.1949; 164:666.
C50. Ken, Janet Storey, Frozen and Alive, SCIENTIFIC AMERICAN December 1990
C51. Karl Erik Zachariassen and Erlend Kristiansen, Ice Nucleation and Antinucleation in Nature, Cryobiology, Volume 41, Issue 4, December 2000, Pages 257-279
C52. I. SUDA, K. KITO & C. ADACHI, Viability of Long Term Frozen Cat Brain In Vitro, NATURE 212:268-270 (1966)
C53. Suda, I., K. Kite, and C. Adachi, Bioelectric discharges of isolated cat brain after revival from years of frozen storage, Brain Res, 70, 527-531 (1974).
C54. Karow AM, Webb WR. Tissue freezing. A theory for injury and survival. Cryobiology. 1965 Nov-Dec;2(3):99-108.
C55. A.U.Smith, Biological effects of freezing and supercooling, Ed, p.304-368
C56. M. Darwin, S. Russell, P. Wakfer, L. Wood, C. Wood, Effect of human cryopreseervation protocol of the ultrastructure of the canine brain, BPI Tech Brief 16 on CryoNet and sci.cryonics May 31, 1995
D1. Nowell, P. C. (1976) Science 194, 23-8.
D2. Prehn, R. T. (1964) J Natl Cancer Inst 32, 1-17.
D3. Hanahan, D. & Weinberg, R. A. (2000) Cell 100, 57-70.
D4. Kim, U. & Depowski, M. J. (1975) Cancer Res 35, 2068-77.
D5. Gregory, S. G. *et al.* The DNA sequence and biological annotation of human chromosome 1, Nature 441, 315-21 (2006)
D6. Bishop, A. J. & Schiestl, R. H. (2003) Exp Mol Pathol 74, 94-105.
D7. Helleday, T., Lo, J., van Gent, D. C. & Engelward, B. P. (2007) DNA Repair (Amst).

D8. Cox, M. M., Goodman, M. F., Kreuzer, K. N., Sherratt, D. J., Sandler, S. J. & Marians, K. J. (2000) Nature 404, 37-41.

D9. Seigneur, M., Bidnenko, V., Ehrlich, S. D. & Michel, B. (1998) Cell 95, 419-30.

D10. Strumberg, D., Pilon, A. A., Smith, M., Hickey, R., Malkas, L. & Pommier, Y. (2000) Mol Cell Biol 20, 3977-87.

D11. Saleh-Gohari, N., Bryant, H. E., Schultz, N., Parker, K. M., Cassel, T. N. & Helleday, T. (2005) Mol Cell Biol 25, 7158-69.

D12. Saintigny, Y., Delacote, F., Vares, G., Petitot, F., Lambert, S., Averbeck, D. & Lopez, B. S. (2001) Embo J 20, 3861-70.

D13. Chaganti, R. S., Schonberg, S. & German, J. (1974) Proc Natl Acad Sci U S A 71, 4508-12.

D14. Prince, P. R., Emond, M. J. & Monnat, R. J., Jr. (2001) Genes Dev 15, 933-8.

D15. Moynahan, M. E., Chiu, J. W., Koller, B. H. & Jasin, M. (1999) Mol Cell 4, 511-8.

D16. Moynahan, M. E., Pierce, A. J. & Jasin, M. (2001) Mol Cell 7, 263-72.

D17. Bishop, A. J., Kosaras, B., Sidman, R. L. & Schiestl, R. H. (2000) Mutat Res 457, 31-40.

D18. Bill, C. A. & Nickoloff, J. A. (2001) Mutat Res 487, 41-50.

D19. Thompson, L. H. & Schild, D. (2002) Mutat Res 509, 49-78.

D20. Venkitaraman, A. R. (2002) Cell 108, 171-82.

D21. Hendricks, C. A., Almeida, K. H., Stitt, M. S., Jonnalagadda, V. S., Rugo, R. E., Kerrison, G. F. & Engelward, B. P. (2003) Proc Natl Acad Sci U S A 100, 6325-30.

D22. Edlund, H. (2002) Nat Rev Genet 3, 524-32.

D23. Li, D., Xie, K., Wolff, R. & Abbruzzese, J. L. (2004) Lancet 363, 1049-57.

D24. Wiktor-Brown, D. M., Hendricks, C. A., Olipitz, W. & Engelward, B. P. (2006) Proc Natl Acad Sci U S A 103, 11862-7.

E1. Gilbert, R. J., S. Daftary, T. A. Campbell, and R. M. Weisskoff. 1998. Patterns of lingual tissue deformation associated with bolus containment and propulsion during deglutition as determined by echo-planar MRI. J. Magn. Reson. Imaging. 8:554–560.

E2. Miller, A. J. 1982. Deglutition. Physiol. Rev. 62:129–184.

E3. Groher, M. 1997. Dysphagia: Diagnosis and Management, 3rd ed. Butterworth-Heinemann Press, Boston.

E4. Palmer, J. B., N. J. Rudin, G. Lara, and A. W. Crompton. 1992. Coordination of mastication and swallowing. Dysphagia. 7:187–200.

E5. Thexton, A. J. 1992. Mastication and swallowing. Br. Dent. J. 173: 197–206.

E6. Gilbert, R. J., S. Daftary, T. G. Reese, R. M. Weisskoff, and V. J. Wedeen. 1998. Determination of lingual myoarchitecture in whole tissue by NMR imaging of

anisotropic water diffusion. Am. J. Physiol. 175:G363–G369.

E7. Wedeen, V. J., T. G. Reese, V. J. Napadow, and R. J. Gilbert. 2001. Demonstration of primary and secondary fiber architecture of the bovine tongue by diffusion tensor magnetic resonance imaging. Biophys. J. 80:1024–1028.

E8. Napadow, V. J., Q. Chen, V. Mai, P. T. C. So, and R. J. Gilbert. 2001. Quantitative analysis of three-dimensionally resolved fiber architecture

E9. Richard J. Gilbert, Lee H. Magnusson, Vitaly J. Napadow, Thomas Benner, Ruopeng Wang and Van J. Wedeen. Mapping Complex Myoarchitecture in the Bovine Tongue with Diffusion-Spectrum Magnetic Resonance Imaging, Biophysical Journal 91:1014-1022 (2006)

E10. Napadow, V. J., Q. Chen, V. J. Wedeen, and R. J. Gilbert. 1999. Intramural mechanics of the human tongue in association with physiological deformations. J. Biomech. 32:1–12.

E11. Napadow, V. J., Q. Chen, V. J. Wedeen, and R. J. Gilbert. 1999. Biomechanical basis for lingual tissue deformation during swallowing. Am. J. Physiol. 40:G695–G701.

E12. Napadow, V. J., R. D. Kamm, and R. J. Gilbert. 2002. Biomechanical model of sagittal bending for the human tongue. J. Biomech. Eng. 124:547–556.